OPTIMIZATION OF SUPERCONDUCTING CROSSBAR H-MODE CAVITY PREPARATION

Dissertation zur Erlangung des Doktorgrades der
Naturwissenschaften

Vorgelegt am Fachbereich Physik der Johann Wolfgang
Goethe-Universität in Frankfurt am Main

von
Patrick Müller
aus
Wiesbaden

Frankfurt am Main, 2024
(D30)

GOETHE
UNIVERSITÄT
FRANKFURT AM MAIN

Vom Fachbereich Physik der
Goethe Universität als Dissertation angenommen.

Dekan: Prof. Dr. R. Erb
1. Gutachter: Prof. Dr. H. J. Podlech
2. Gutachter: Prof. Dr. U. Ratzinger

Datum der Disputation:

Acronyms

CH	Cross-Bar H-Mode
SHE	Super Heavy Elements
CN	Compound Nuclei
IAP	Institute for Applied Physics
RF	Radio Frequency
CH	Cross-Bar H-Mode
NC	Normal Conducting
SC	Superconducting
CN	Compound Nuclei
HELIAC	Helmholtz Linear Accelerator
CN	Compound Nuclei
IH	Interdigital H-Mode
DTL	Drift Tube Linac
HIM	Helmholtz Institute Mainz
GSI	Gesellschaft für Schwerionenforschung
HPR	High-Pressure Rinsing
RFQ	Radio Frequency Quadrupole
UHV	Ultra-High Vacuum
TE	Transverse Electric
TM	Transverse Magnetic
CW	Continuous Wave
RT	Room Temperature
DUT	Device Under Test
SEC	Secondary Electron Coefficient
AC	Alternating Current
DC	Direct Current
RR	Residual Resistance Ratio
GTI	Global Thermal Instability
SRF	Superconducting Radio-Frequency
BCP	Buffered Chemical Polishing
EP	Electro Polishing
HWR	Halve-Wave Resonator
QWR	Quarter-Wave Resonator
FM	Frequency Modulation

Zusammenfassung

In dieser Dissertation werden die Erfahrungen mit verschiedenen Präparationsmethoden für CH-Kavitäten beschrieben, um die Leistung der Kavitäten nach der Herstellung weiter zu steigern. Die Leistung wird anhand von zwei wichtigen HF-Parametern bewertet: dem elektrischen Feld E_a und der intrinsischen Güte Q_0. Im Gegensatz zu normalleitenden (NC) Kavitäten kann die intrinsische Güte von supraleitenden (SC) Kavitäten mit zunehmendem elektrischem Feld erheblich variieren. Das optimale Ergebnis für die Kavitätenpräparation ist die Erhöhung des maximalen elektrischen Feldes unter Beibehaltung eines höheren Q_0 über die gesamte Feldspanne. Da Q_0 umgekehrt proportional zu den Kavitätsverlusten ist, reduziert eine Erhöhung des Qualitätsfaktors die Kryoverluste für den Betrieb bei gegebenem Feldniveau. Die Entwicklung der Kavitätenperformanz im Verlauf dieser Arbeit ist in Abbildung 1 dargestellt.

Die meisten SC-Kavitäten sind elliptische Strukturen, welche bei hoher Geschwindigkeit und Tastrate angewendet werden. Die Präparationsmethoden wurden daher überwiegend auf diese Strukturen angewandt und optimiert. Diese Arbeit konzentriert sich auf die Umsetzung der zuverlässigsten und vielversprechendsten Oberflächenbehandlungen mittels des ersten vom IAP entwickelten SC 360 MHz CH-Prototyps. Diese Kavität wies nach 11 Jahren Lagerung eine verminderte Leistung auf, welche mit Röntgenstrahlung bei bereits niedrigen elektrischen Feldern einherging. Dies deutet auf eine unbeabsichtigte Belüftung mit normaler Luft hin, durch die Partikel eingeführt wurden, die als verstärkende Quellen von Elektronen fungierten. Außerdem musste der Leistungskoppler aufgrund einer starken Überkopplung neu ausgelegt werden.

Die Kavität wurde für 48 Stunden bei 120° C mittels Heizbändern in der Experimentierhalle des IAP's ausgeheizt, was zu einer Verbesserung des Qualitätsfaktors bei niedrigen Werten und zu einer Verkürzung der für die Konditionierung von Multipacting-Barrieren erforderlichen Zeit führte. Allerdings wurde durch diese Behandlung das maximale erreichbare elektrische Feld weiter verringert. Die Verbesserung der Güte ist auf das Ausgasen der Kohlenwasserstoffe während des Backvorgangs zurückzuführen. Die negative Auswirkung auf das maximale elektrische Feld ist weniger auf das Backen selbst zurückzuführen als auf den Transport der Kavität und die verwendeten Vakuumkomponenten, die in der Versuchshalle gelagert sind.

Die beobachtete Leistungseinschränkung lässt sich hauptsächlich durch Partikel im Inneren des Resonators erklären, da Feldemission bei niedrigen Feldstärken auftrat. Eine Hochdruckspülung mit ultrareinem Wasser (HPR) ist das Standardverfahren, um nach Behandlungen, bei denen das Risiko einer Oberflächenkontamination besteht, eine hohe Reinheit der inneren Oberflächen zu erreichen. Die HPR wurde in Zusammenarbeit mit dem Helmholtz-Institut-Mainz und der Gesellschaft für Schwerionenforschung geplant und durchgeführt. Der Resonator zeigte bereits während der Messung der Q-E-Kurve eine Zunahme der transmittierten Leistung bei konstanter Vorwärtsleistung, was vor der HPR nicht der Fall war. Bei der CW-HF-Konditionierung zeigte die Kavität den höchsten Gradienten bei einem deutlich schwächeren Q-Abfall bei hohen Feldstärken.

Sowohl bei der Messung von 2008 als auch bei der beschriebenen Messung wurde die Kavität mit einer HPR-Behandlung fertiggestellt, aber für die HPR-Behandlung bei HIM in Mainz wurden einige Anpassungen vorbereitet. Der CH Prototyp verfügt über keine zusätzlichen Spülports und wurde daher mit zwei verschiedenen Düsen mit unterschiedlichen Sprühwinkeln gespült, um die erreichbaren inneren Resonatorflächen zu maximieren. Die Verwendung mehrerer Sprühwinkel könnte auch für CH-Kavitäten mit Spülöffnungen von Vorteil sein und sollte für zukünftige HPR-Anwendungen in Betracht gezogen werden.

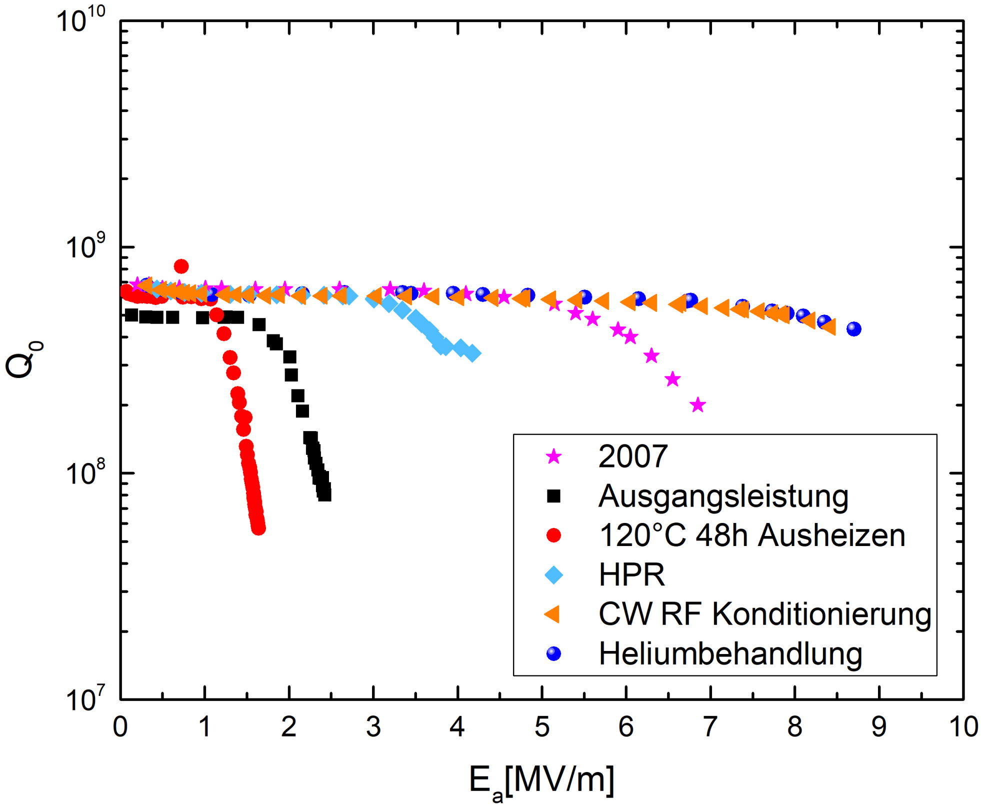

Abb. 1: Entwicklung des Kavitätenverhaltens in Abhängigkeit der durchgeführten Preparationsmethoden im Vergleich zum bisher besten Ergebnis aus 2007.

Die Heliumbehandlung wurde am CH-Prototyp 2,5 Stunden lang durchgeführt und lieferte vielversprechende Ergebnisse in Bezug auf die Güte und die Gradientenoptimierung. Während dieses Prozesses wurde die emittierte Röntgenstrahlung in Richtung am Arbeitsplatzs gemessen und zeigte starke zeitabhängige Fluktuationen. Dies deutete auf die Beseitigung von Partikeln hin und wurde anschließend durch einen Anstieg des elektrischen Feldes von 8,4 auf 8,7 MV/m bestätigt. Eine unerwartete Auswirkung wurde bei der Q-Steigung im mittleren bis hohen Feld festgestellt, bei der der Qualitätsfaktor im Vergleich zum HF-konditionierten Fall eine Erhöhung von 5 % oberhalb von 2 MV/m aufwies. Dieser systematische Anstieg wurde für diesen Beschleuniger vor der Behandlung bisher nicht beobachtet. Stickstoffgedopte Kavitäten zeigen ein ähnliches Verhalten, bei dem Wechselwirkungen innerhalb der Oxidschicht mit Änderungen der Qualitätsfaktoren korreliert sind. Da Helium ein nicht reaktives Element ist, sind mögliche Erklärungen für diesen Effekt der Sputterprozess und die Einlagerung von Helium innerhalb der Oberfläche. Eine Serie von Heliumbehandlungen ist geplant, um ein optimiertes und sicheres Rezept für CH-Kavitäten zu finden. Die Q-E-Messung nach der Abkühlung und vor der Behandlung wird auch zeigen, ob der Leistungsgewinn durch ein Aufwärmen auf Raumtemperatur beeinträchtigt wird.

Die in dieser Arbeit skizzierte Behandlungssequenz wird für CH-Kavitäten dringend empfohlen. Das Ausheizen hat sich bei der Verringerung des Multipactings and der Güteabnahme bei hohen Feldern als wirksam erwiesen und bleibt von der anschließenden HPR unbeeinflusst. In dieser Arbeit wurden keine negativen Auswirkungen der HPR auf das Multipactingverhalten festgestellt. Anschließend wird eine CW-HF-Konditionierung durchgeführt, bis keine weitere Leistungszunahme der Kavität mehr zu verzeichnen ist. Wenn die Kavität immer noch durch Feldemission begrenzt ist, sollte eine Wiederholung der HPR-Behandlung in Betracht gezogen werden, da bei sorgfältiger Durchführung der HPR keine der bisherig gefertigten CH-Kavitäten hierdurch begrenzt war. Es ist auch anzumerken, dass die Heliumbehandlung nur an der 360 MHz CH-Kavität durchgeführt wurde, als diese eine geringe Strahlung durch Feldemission aufwies. Das Risiko des Heliumprocessing an CH-Kavitäten unter starker Feldemission ist unbekannt. Es ist zu erwarten, dass die Elektronenströme und damit die Ionenbeschusslawinen zunehmen und ein größeres Risiko für die Beschädigung von der Komponenten darstellen. Nach dem derzeitigen Kenntnisstand sollte die Heliumbehandlung nur für gut vorbereitete Kavitäten mit minimaler Feldemission in Betracht gezogen werden.

In dieser Arbeit wird ein optimierter Plan für die Präparation von CH-Strukturen vorgestellt, siehe Abbildung 2, der die Leistung nach der Standard-BCP-Behandlung maximiert. Neue Erkenntnisse über die Optimierung der einzelnen Behandlungen bilden die Grundlage für die weitere Untersuchung der CH-Kavitätenpräparation.

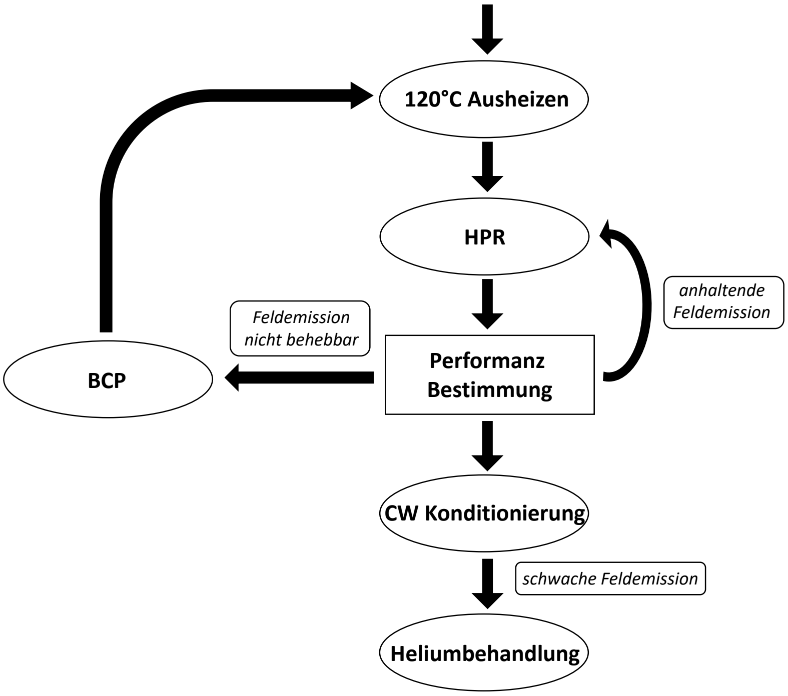

Abb. 2: Schematische Darstellung des empfohlenen Preparationsablaufes für CH Kavitäten.

Contents

1 Introduction

1.1 Super Heavy Ion Synthesis

The research on the synthesis of elements beyond uranium started in the 1930s. Neutron capture and subsequent β^- decay were initially expected to produce transuranic elements. In 1938, Hahn and Strassmann observed a different effect, which led to the development of the important liquid drop model, used in 1939[1] to explain fission of nuclei [1]. After neutron capture, the heated uranium nucleus broke into two parts of approximately equal mass [2]. The phenomenon is called nuclear fission, which is an induced fission, in contrast to the spontaneous fission during natural uranium decay, first detected by Flerov and Petrjak in 1940 [3]. The liquid drop model predicts an upper limit for nuclei, which corresponds with elements in the range of 100–110. The model did not explain isotopes with increased observed binding energy, featuring 2, 8, 20, 28, 50, and 82 protons or neutrons. These so-called magic numbers were explained by the nuclear shell model, which was extrapolated to search for further stable elements. Proton numbers 114 or 120, and neutron number 184, were predicted to be the next shell closures. Nuclei with these parameters are referred to as the island of stability, where the binding energy is expected to be increased compared to adjacent isotopes. The synthesis of new superheavy elements (SHE) required more powerful accelerators for heavy ion fusion reactions. The ion beam is used in a collision reaction with a heavy element target, which can form new compound nuclei (CN). When the coulomb barrier is successfully overcome, nuclei are bound by the attractive strong force and result in a new compound nucleus. The CN is generally excited, which can lead to fission into the initial compounds. Alternatively, the fission process can occur during mass equilibration and is prevalent when a fragment in the double magic region of ^{208}Pb is produced [4]. If the CN does not undergo fission, it emits neutrons and x-rays and forms an evaporation residue in the ground state. The fusion process can be distinguished into cold and hot fusion. Cold fusion was successfully achieved with a strongly bound ^{208}Pb or ^{209}Bi target. Strongly bound elements from calcium (Ca) to zinc (Zn) were used as projectiles to produce compound nuclei with only 12 to 20 MeV excitation energy. The ground state of the nuclei is reached via evaporation of 1 to 2 neutrons and gamma rays. Hot fusion reactions are based on actinide targets and lighter projectiles. The compound nuclei evaporate an excitation energy of 35 to 50 MeV via 3 to 5 neutrons. The elements from $Z = 107$ to 112 were discovered by "Gesellschaft für Schwerionenforschung" (GSI). An example of those elements is Darmstadtium (Ds), which was synthesized by the cold fusion reaction [5]:

$$^{208}_{82}\mathrm{Pb} +^{62}_{28}\mathrm{Ni} \rightarrow^{269}_{110}\mathrm{Ds} +^{1}_{0}\mathrm{n} \tag{1.1}$$

---

[1] The liquid drop model was developed by George Gamow, Hans Bethe, and Carl Friedrich von Weizäcker

The elements from $Z = 114$ up to $Z = 118$ have been discovered by JINR in Dubna. The heaviest synthesized element, Oganesson, has been discovered by the hot fusion reaction [6]:

$$^{249}_{98}\mathrm{Cf} +^{48}_{20}\mathrm{Ca} \rightarrow^{294}_{118}\mathrm{Og} + 3^{1}_{0}\mathrm{n} \tag{1.2}$$

The measured cross sections of cold and hot fusion are shown in Figure 1.1.

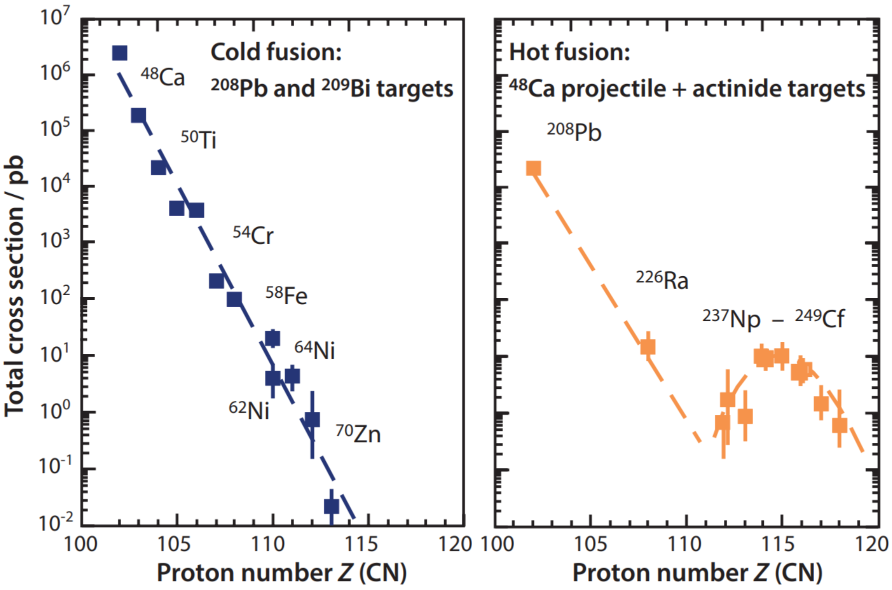

Figure 1.1: Cross sections of cold fusion (left) and hot fusion (right) [7].

The further synthesis of SHE requires improved detection sensitivity and higher beam intensities. Spectroscopic data on neutron-deficient, lower Z-isotopes may lead to insights into the shell structures of nuclei up to $Z = 126$. The production of neutron-rich isotopes near the island of stability for $N = 184$ and the production of neutron-rich isotopes with expected increased half-lives of $Z = 107$ to 114 are important open questions [7].

1.2 HELIAC

The Institute for Applied Physics (IAP) in Frankfurt, Germany, has developed a low-β radio frequency (RF) cavity structure. This H-mode accelerator is named Cross-Bar H-Mode (CH) structure and it is applicable for normal conducting (NC) and superconducting (SC) cavity design. The 'Gesellschaft für Schwerionenforschung' (GSI) is a research facility in the fields of nuclear physics, atomic physics, plasma physics, biophysics, material research, and tumor therapy located in Darmstadt, Germany. The main accelerator consists of the High Charge State Injector (HLI), High Current Injector (HSI), the Universal Linear Accelerator (UNILAC), the SIS18 synchrotron, and the Experimental Storage Ring (ESR). GSI is currently realizing the FAIR project, see Figure 1.2.

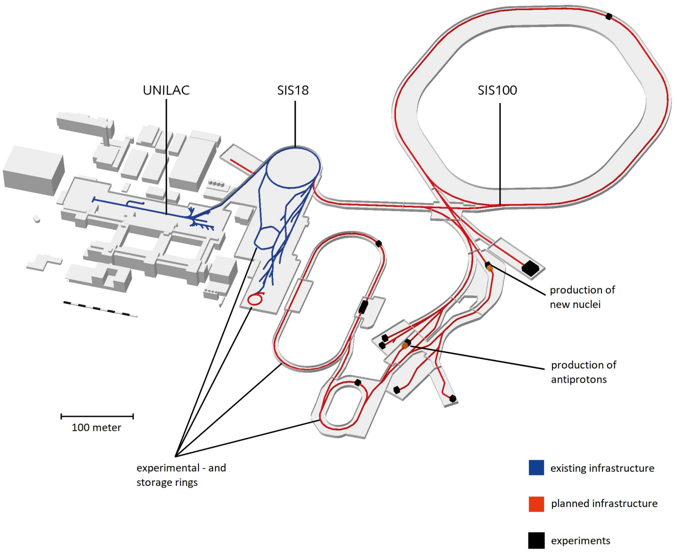

Figure 1.2: Layout of the FAIR project, modified [8].

The UNILAC is planned to exclusively function as injector into the SIS100 synchrotron. The research on SHE will continue with a new dedicated SC continuous-wave (CW) 'Helmholtz Linear Accelerator' (HELIAC)[2], shown in Figure 1.3, which is currently under construction. The heavy ions are provided by the High Charge State Injector (HLI). The HLI consists of an 18 GHz electron cyclotron resonance ion source (ECR), a 108 MHz four-rod Radio Frequency Quadropol (RFQ), and a 108 MHz interdigital H-mode drift tube linac (IH-DTL). The injection energy into HELIAC is $W_{\mathrm{in}} = 1.39\,\mathrm{MeV/u}$ for a mass-to-charge ratio $A/z \leq 6$ and beam currents of $I_{\mathrm{b}} \leq 1\,\mathrm{mA}$.

---

[2] previously CW-linac

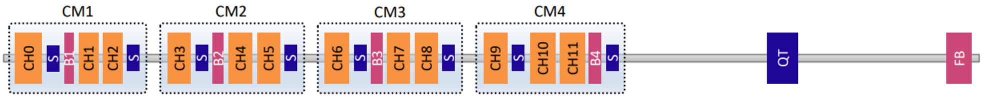

Figure 1.3: Schematic layout of the preliminary full HELIAC accelerator cryo module configuration [9].

A total of 12 SC CH cavities, distributed over 4 cryo modules, will deliver beam energies ranging from 3.5 MeV/u to 7.3 MeV/u. The design gradient of the CH cavities is 7.1 MV/m. Additional performance of these cavities enables higher energy gain or acceleration of particles with a mass-to-charge ratio $A/z > 6$. The beam dynamic layout of HELIAC supports ratios up to $A/z = 8.5$, given by gold ion with a required gradient of 10 MV/m.

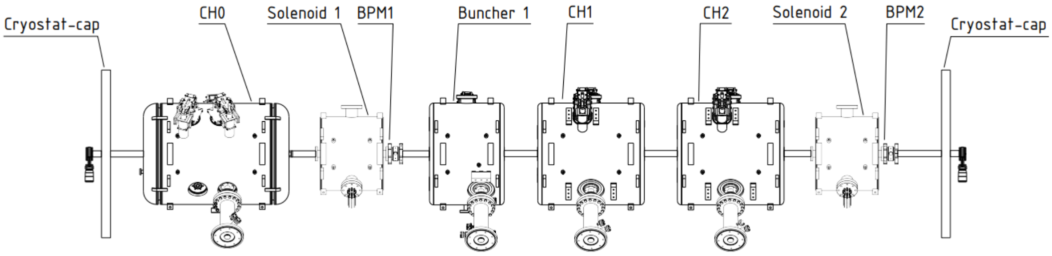

Figure 1.4: Layout of the first cryo module for the HELIAC accelerator [9].

Cavities, solenoids, and beam positioning monitors have been assembled in the clean room at HIM and successfully integrated into cryo module 1 in 2023, Figure 1.4 shows the schematic layout of the module. It has been transported to GSI and successfully accelerated He nuclei, provided by HLI, in 2023.

1.3 Cavity Preparation

The assessment of RF performance for SC linac cavities is mainly based on two factors: Q_0 and the maximum electric field gradient $E_{\mathrm{a}}^{\mathrm{max}}$. The intrinsic quality factor is linked to the total cavity losses, which are strongly dependent on the electric and magnetic field strength in the case of SC cavities. Multiple mechanisms lead to additional and increased losses with increasing field levels. When the cavity is pushed to its maximum field level, the superconducting phase fails and the cavity transitions into the normal conducting phase. This event is called a 'quench' and is caused by exceeding the critical supercurrent limit of the superconductor. This limit is dependent on a multitude of mechanisms that are dependent on the material properties, as well on the geometry and high-level field effects inside the cavity. Post-manufacturing cavity preparation of SC RF cavities is an ongoing research field that pushes the performance limits of SC cavities. The majority of SC sections of accelerators are elliptical cavities, as discussed in Chapter 2.3. Preparation methods therefore have been optimized towards these structures. Elliptical structures are not suited for particle acceleration below β of 0.6. Common low β structures for SC operation are Quarter-Wave Resonators (QWR) and Half-Wave Resonators (HWR).

Project	Cavity Type	Maximum Gradient
HELIAC	CH	9.6 MV/m
ATLAS	QWR	13.5 MV/m
PIAVE	QWR	5.5 MV/m
RAON	QWR	10.5 MV/m
ISAC-II	QWR	9 MV/m
HIE-ISOLDE	QWR	7 MV/m
SPIRAL2	QWR	12 MV/m
SRILAC	QWR	12 MV/m

Table 1.1: Comparison of low beta structure gradients.[10, 11, 12, 13, 13, 14, 15, 16, 17, 18]

While the gradient of CH structures is competitive with QWRs displayed in Table 1.1, the multicell design delivers high voltage cavities, which results in fewer total cavities required and higher average voltage gain per meter along the linac.

2 RF Accelerator Physics Fundamentals

The development of particle accelerators started with Rutherford in 1911, who demonstrated the existence of a positively charged nucleus via the scattering of α particles on a thin gold foil. The first nuclear transmutation, p + Li → 2He, was performed in 1932 with the Cockcroft-Walton electrostatic accelerator [19]. This accelerator type was widely used as the first acceleration unit after an ion source and nowadays is replaced by the more efficient, economical, and reliable Radio Frequency Quadrupole (RFQ). Another important electrostatic accelerator is the Van de Graaff (tandem) accelerator, invented in 1931, which allowed for research on heavy-ion nuclear reactions. The electrostatic accelerators are limited by sparking. RF-based structures can be distinguished into cyclic and linear accelerators. For the interested reader, a small selection of books that include cyclic structures are referenced [20, 21, 22].

Different designs of linear RF cavities have been developed over the years, that work for different beam velocities β and frequency ranges f. This chapter summarizes the physics behind the pillbox-based accelerator structures and describes key performance characteristics of general RF cavities.

2.1 Maxwell's Equation and Pillbox Solution

Classical electrodynamics encompasses the origin and propagation of electromagnetic fields and the interaction of charged particles with those fields. Electromagnetic fields are derived and calculated using Maxwell's equations. The interaction of charged particles with electromagnetic fields is given by Couloumb's and Lorentz's law. First, the field equations are explained and then applied to the underlying resonator geometry of a CH structure.

$$\nabla \cdot \mathbf{E} = \frac{\rho}{\epsilon_0} \tag{2.1}$$

$$\nabla \cdot \mathbf{B} = 0 \tag{2.2}$$

$$\nabla \times \mathbf{E} = -\frac{\partial \mathbf{B}}{\partial t} \tag{2.3}$$

$$\nabla \times \mathbf{B} = \mu_0 \mathbf{j} + \mu_0 \epsilon_0 \frac{\partial \mathbf{E}}{\partial t} \tag{2.4}$$

Equation 2.1, known as the law of Gauss, states that electric charges are the sources and sinks of electric fields. Equation 2.2 describes the absence of magnetic charges as sources of magnetic fields. Equation 2.3, known as Faraday's law of induction, states that time-varying magnetic fields lead to the induction of vortex electric fields and, consequently, voltage. Equation 2.4 is Ampere's law, stating that magnetic fields are generated by electric currents and electric fields that change with time.

Accelerator cavities present boundary conditions for Maxwell's equations, determined by the geometry of the inner surfaces. Furthermore, negligible amounts of charged particles

($\rho = 0$) and ($\mathbf{j} = 0$) are located inside the cavity at UHV[3]. With these simplifications, wave equations for electric and magnetic fields can be derived from Maxwell's equations.

$$\left(\Delta - \frac{1}{c^2}\frac{\partial^2}{\partial t^2}\right)\mathbf{E} = 0 \tag{2.5}$$

$$\left(\Delta - \frac{1}{c^2}\frac{\partial^2}{\partial t^2}\right)\mathbf{B} = 0 \tag{2.6}$$

The closed metallic surfaces of a cavity form the geometrical boundary conditions for the wave equations 2.5 and 2.6, leading to the mode formation of electromagnetic field solutions. The underlying geometry for the CH structure is that of a cylinder, referred to as a pillbox. The modifications to a pillbox to achieve a CH structure are explained in Chapter 3.1.1. For the inner surfaces of the cavity, the following conditions apply to the electric and magnetic fields:

$$\mathbf{n} \times \mathbf{E} = 0 \tag{2.7}$$

$$\mathbf{n} \cdot \mathbf{H} = 0 \tag{2.8}$$

Equation 2.7 states that the electric field is perpendicular to the surface, and parallel field components on the surface must disappear. Equation 2.8 states that for the magnetic field, the field has only a parallel component on the surface, and the perpendicular component must disappear on the surface.

We will derive the solution for the pillbox by solving a waveguide of constant cross-section and infinite length in the z-direction. Then, we will apply the boundaries of the pillbox. Inside the waveguide, the electromagnetic field propagates along the z-axis with a frequency of ω and the wave number k:

$$\mathbf{E}(\mathbf{x}, t) = \mathbf{E}(\rho, \phi)\mathrm{e}^{ikz-i\omega t} \tag{2.9}$$

$$\mathbf{H}(\mathbf{x}, t) = \mathbf{H}(\rho, \phi)\mathrm{e}^{ikz-i\omega t} \tag{2.10}$$

Equation 2.9 and 2.10 provide the electromagnetic field components inside the waveguide. We can apply Equation 2.5 and 2.6 to Equation 2.9 and 2.10.

$$\left(\Delta - \frac{1}{c^2}\frac{\partial^2}{\partial t^2}\right)\begin{pmatrix} \mathbf{E} \\ \mathbf{H} \end{pmatrix} = 0 \tag{2.11}$$

The Nabla operator can be separated into a perpendicular and a parallel part to the z-axis:

$$\nabla = \begin{pmatrix} \nabla_\perp \\ \frac{\partial}{\partial z} \end{pmatrix} \tag{2.12}$$

---

[3] Acronym for ultra-high vacuum

This wave equation now becomes:

$$\left(\Delta_\perp + \frac{\omega^2}{c^2} - k_z^2\right)\begin{pmatrix}\mathbf{E}\\ \mathbf{H}\end{pmatrix} = 0 \tag{2.13}$$

Equation 2.13 represents an orthogonal set of eigenvalue solutions with eigenvalues $k_\perp^2 = \frac{\omega^2}{c^2} - k_z^2$. The longitudinal solutions E_z and H_z must still satisfy the boundary conditions of the waveguide surface.

$$E_z\Big|_S = 0 \tag{2.14}$$

$$\frac{\partial H_z}{\partial n}\Big|_S = 0 \tag{2.15}$$

Since E_z and H_z are independent, the solutions of the differential equations form two sets of modes with unique eigenvalues. These solutions can be categorized into transverse electric modes (TE) and transverse magnetic modes (TM). The transverse field components are related through the wave impedance:

$$\mathbf{H}_\perp = \pm\frac{\mathbf{e}_z \times \mathbf{E}_\perp}{Z} \tag{2.16}$$

with $Z = \frac{k}{\epsilon_0\omega}$ for TM and $Z = \frac{\mu_0\omega}{k}$ for TE modes. TE modes exclusively have transverse electric field components and we can see from Equation 2.3 that magnetic longitudinal field solutions exist. In contrast, TM modes only have transverse magnetic field components. Equation 2.4 combined with the vacuum condition $\mathbf{j} = 0$ yields the existence of a longitudinal electric field solution. TM modes are used for particle acceleration, whereas TE modes have no longitudinal electric field component and can not be used for particle acceleration in a pillbox setting. Later we will see, that modifications to the pillbox will generate longitudinal electric field components from TE-based modes.

Longitudinal and transverse fields of each type are related by:

$$\begin{pmatrix}\mathbf{E}_\perp\\ \mathbf{H}_\perp\end{pmatrix} = \pm\frac{ik_z}{k_\perp^2}\nabla_\perp\begin{pmatrix}\mathbf{E}_z\\ \mathbf{H}_z\end{pmatrix} \tag{2.17}$$

These findings from an infinite waveguide can now be translated into solutions for a cavity of length L, by adding conducting faces at $z = 0$ and $z = L$. Boundary conditions 2.7 and 2.8 now also apply to the longitudinal solutions, resulting in standing waves.

$$E_z(\mathbf{x}, t) = \Phi_\mathrm{E}(r,\phi)\cos\left(\frac{p\pi z}{L}\right)\mathrm{e}^{i\omega t}, \qquad p = 0, 1, 2... \tag{2.18}$$

$$H_z(\mathbf{x}, t) = \Phi_\mathrm{H}(r,\phi)\sin\left(\frac{p\pi z}{L}\right)\mathrm{e}^{i\omega t}, \qquad p = 1, 2, 3... \tag{2.19}$$

We can now apply equation 2.13 to the standing wave solutions and find the eigenvalue equation

$$\left(\Delta_\perp + k_{\perp,j}^2\right)\Phi(r,\phi) = 0 \tag{2.20}$$

with $k_{\perp,j}^2 = \left(\frac{\omega_j}{c}\right)^2 - \left(\frac{p\pi}{L}\right)^2$ and ω_j beeing the jth eigenvalue.

Longitudinal solutions 2.18 and 2.19 combined with equation 2.17 result in differential equations for transverse TE and TM fields.

TE solutions:

$$\mathbf{E}_\perp = -\frac{i\eta\omega_j}{ck_{\perp,j}^2}\mathbf{e}_z \times \nabla_\perp\Phi(r,\phi)\sin\left(\frac{p\pi z}{L}\right) \tag{2.21}$$

$$\mathbf{H}_\perp = \frac{p\pi}{k_{\perp,j}^2}\nabla_\perp\Phi(r,\phi)\cos\left(\frac{p\pi z}{L}\right) \tag{2.22}$$

TM solutions:

$$\mathbf{E}_\perp = -\frac{p\pi}{k_{\perp,j}^2}\nabla_\perp\Phi(r,\phi)\sin\left(\frac{p\pi z}{L}\right) \tag{2.23}$$

$$\mathbf{H}_\perp = \frac{i\eta\omega_j}{ck_{\perp,j}^2}\mathbf{e}_z \times \nabla_\perp\Phi(r,\phi)\cos\left(\frac{p\pi z}{L}\right) \tag{2.24}$$

Now consider a cylindrical pillbox cavity with length L and radius R. The solution to cylindrical transverse eigenvalue equation 2.20 are Bessel functions J_m. The entire set of TM modes becomes:

$$E_z = E_0 J_m\left(x_{mn}\rho\right)\cos(m\phi)\cos\left(\frac{p\pi z}{L}\right) \tag{2.25}$$

$$E_r = -E_0\frac{p\pi R}{Lx_{mn}}J_m'\left(x_{mn}\rho\right)\cos(m\phi)\sin\left(\frac{p\pi z}{L}\right) \tag{2.26}$$

$$E_\phi = \frac{mp\pi R^2}{rLx_{mn}^2}J_m\left(x_{mn}\rho\right)\sin(m\phi)\sin\left(\frac{p\pi z}{L}\right) \tag{2.27}$$

$$H_z = 0 \tag{2.28}$$

$$H_r = -i\omega_{mnp}E_0\frac{mR^2}{\rho c^2 x_{mn}^2}J_m\left(x_{mn}\rho\right)\sin(m\phi)\cos\left(\frac{p\pi z}{L}\right) \tag{2.29}$$

$$H_\phi = -i\omega_{mnp}E_0\frac{R}{c^2 x_{mn}}J_m'\left(x_{mn}\rho\right)\cos(m\phi)\cos\left(\frac{p\pi z}{L}\right) \tag{2.30}$$

Respectively the TE-Modes become:

$$E_z = 0 \tag{2.31}$$

$$E_r = i\omega_{mnp} B_0^* \frac{mR^2}{x_{mn}^{'2} r} J_m \left(x_{mn}^{'}\rho\right) \cos(m\phi)\sin\left(\frac{p\pi z}{L}\right) \tag{2.32}$$

$$E_\phi = i\omega_{mnp} \frac{R}{x_{mn}^{'}} J_m^{'} \left(x_{mn}^{'}\rho\right) \sin(m\phi)\sin\left(\frac{p\pi z}{L}\right) \tag{2.33}$$

$$H_z = H_0^* J_m(x_{mn}^{'}\rho)\cos(m\phi)\sin\left(\frac{p\pi z}{L}\right) \tag{2.34}$$

$$H_r = -iH_0^* \frac{p\pi R}{Lx_{mn}^{'}} J_m^{'} \left(x_{mn}^{'}\rho\right) \sin(m\phi)\cos\left(\frac{p\pi z}{L}\right) \tag{2.35}$$

$$H_\phi = -H_0^* \frac{p\pi m R^2}{Lx_{mn}^{'2} r} J_m \left(x_{mn}^{'}\rho\right) \cos(m\phi)\cos\left(\frac{p\pi z}{L}\right) \tag{2.36}$$

with $\rho = \frac{r}{R}$. TM and TE modes are characterized by their parameters m, n and ρ. These parameters can be categorized into two distinct groups: transverse and longitudinal parameters. Specifically, m and n divide the transverse plane by m angular separation lines and n radial separation lines. The parameter p defines the number of longitudinal half-waves of the mode. Figure 2.1 shows two pillbox modes, which are the underlying operation modes of the Alvarez (E_{010}) and CH (T_{211}) cavities.

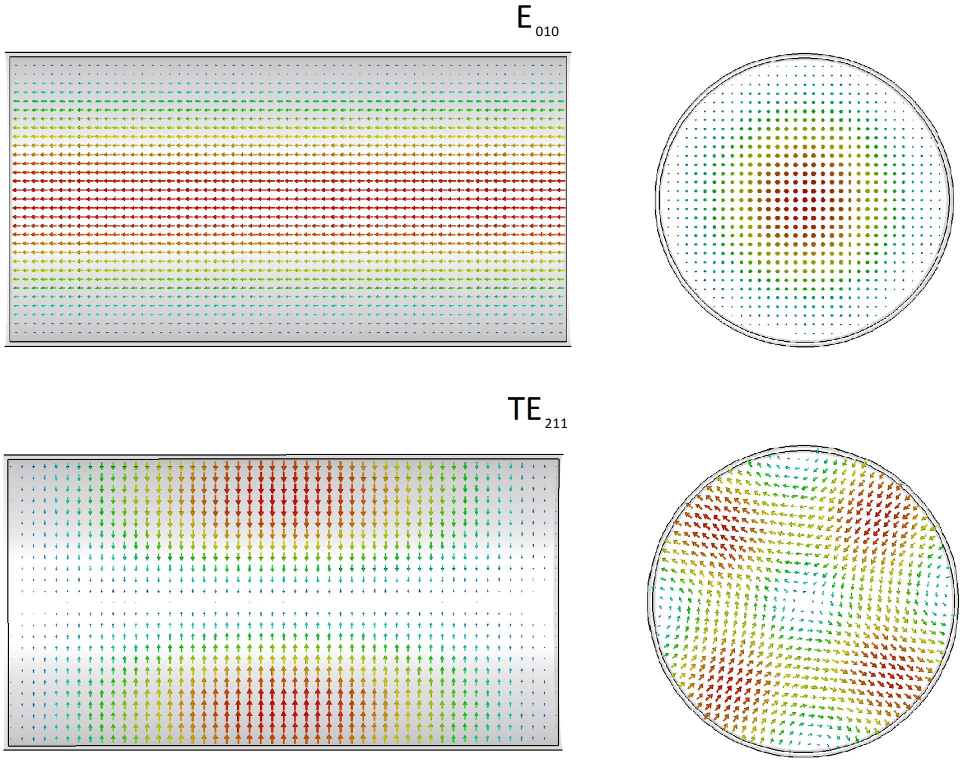

Figure 2.1: Electric field components of the pillbox ground mode E_{010} and the quadrupol operation mode TE_{211} of CH structures, simulated with CST [23].

All non-trivial solutions include Bessel's functions to solve the underlying eigen-differential equations. The eigenvalues are calculated based on the wave numbers and geometry in each spatial direction. This relation can be illustrated by examining the properties of the wave numbers, which satisfy:

$$k^2 = k_x^2 + k_y^2 + k_z^2 = k_\perp^2 + k_z^2 \tag{2.37}$$

For a standing wave solution in a resonator of length L, it must adhere to the relation:

$$k_z L = p\pi \tag{2.38}$$

The boundary condition of an ideal conductor restricts the solutions E_ϕ and B_r of the TE and TM modes:

$$E_\phi(R) = 0 \tag{2.39}$$

$$B_r(R) = 0 \tag{2.40}$$

For TM (E) modes, this leads to the relations:

$$J_m(x_{mn}) = J_m(k_\perp^E R) = 0 \tag{2.41}$$

$$k_\perp^E = \frac{x_{mn}}{R} \tag{2.42}$$

and for TE (H) modes, this results in:

$$J_m^{'}(x_{mn}^{'}) = J_m^{'}(k_\perp^H R) = 0 \tag{2.43}$$

$$k_\perp^H = \frac{x_{mn}^{'}}{R} \tag{2.44}$$

Insertion of the longitudinal and transverse wave number relations 2.38, 2.42 and 2.44 into equation 2.37 yields the cavity resonance wave numbers for E and H modes:

$$k^E = \sqrt{\left(\frac{x_{mn}}{R}\right)^2 + \left(\frac{\pi p}{L}\right)^2} \tag{2.45}$$

$$k^H = \sqrt{\left(\frac{x_{mn}^{'}}{R}\right)^2 + \left(\frac{\pi p}{L}\right)^2} \tag{2.46}$$

The dispersion relation $f = \frac{kc}{2\pi}$ allows the calculation of the resonance frequency of each E and H mode:

$$f^E = c\sqrt{\left(\frac{x_{mn}}{2\pi R}\right)^2 + \left(\frac{p}{2L}\right)^2} \tag{2.47}$$

$$f^H = c\sqrt{\left(\frac{x_{mn}^{'}}{2\pi R}\right)^2 + \left(\frac{p}{2L}\right)^2} \tag{2.48}$$

m	x_{m1}	x_{m2}	x_{m3}	x'_{m1}	x'_{m2}	x'_{m3}
0	2.405	5.520	8.654	3.832	7.016	10.174
1	3.832	7.016	10.173	1.841	5.331	8.536
2	5.136	8.417	11.620	3.054	6.706	9.970

Table 2.1: First zeros of the Bessel's functions J_m and J'_m.

The zeros of the Bessel's functions shown in Table 2.1 can be used to determine the frequency of the resonator modes displayed in Figure 2.2.

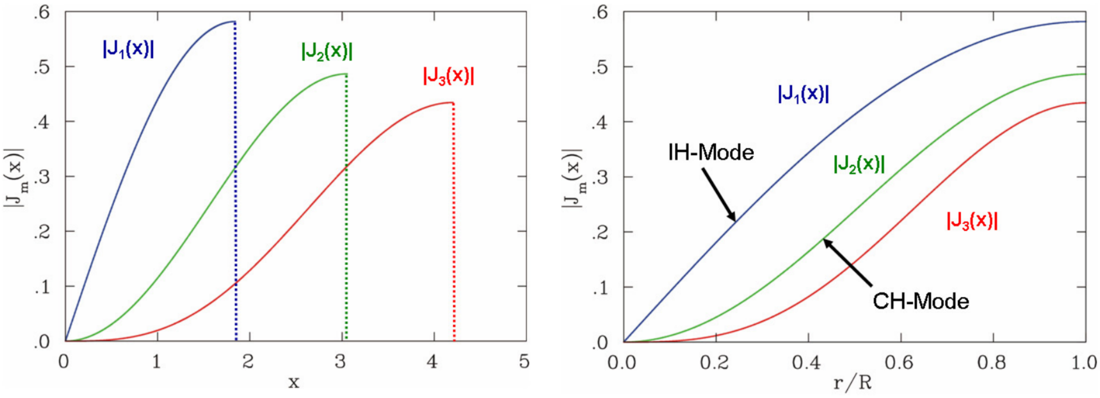

Figure 2.2: Bessel's function $|J_m(x)|$ shown for the the cases $m = 1, 2, 3$, where $m = 1$ is present in the operation mode of an IH-cavity and $m = 2$ is in a CH cavity [24].

In Chapter 2.2.1, we observed that particle acceleration is attained through an electric field component along the beam axis. The pillbox achieves this using the E_{010} mode, which possesses the lowest frequency and is thus referred to as the 'ground mode' of the resonator. The TE_{211} mode serves as the fundamental mode of two modern accelerator types: the CH structure and the 4-vane RFQ. A detailed discussion of the CH structure will be provided in Chapter 3.1.1.

2.2 Cavity RF Parameters

A multitude of resonator types have been developed and established in the field of particle accelerators. These structures cater to distinct boundary conditions defined by the RF and beam requirements of the project. Some structures vary vastly from each other in geometry and the utilization of the underlying RF resonator mode. The following RF parameters express important RF and geometric properties that allow for the comparison of the performance across different cavity types.

2.2.1 Electric Field and Voltage

Electric fields propel charged particles. The electric field component along the beam axis of the accelerator's beam axis is conventionally defined as the z-axis. The amplitude of the electric field adheres to a distribution $E_{z,0} = E_{z,0}(r)$ contingent on the position along the beam axis and oscillates at the resonant frequency ω_{r}. This gives rise to the equation:

$$E_z(r,t) = E_{z,0}(r) \cdot \cos(\omega t) \tag{2.49}$$

Here, $E_z(r,t)$ represents the time-dependent field distribution function of the z-component. Time can be selected so that the field amplitude is maximal when the target particle is positioned at the center of the accelerating gap. The accumulated field along the beam axis gives the voltage $U = \int E \mathrm{d}s$. In the case of RF particle accelerators, the time dependence of the voltage becomes:

$$U(t) = \int_0^{L_C} E_{z,0}(z) \cos(\omega t) \mathrm{d}z = U_0 \cos(\omega t) \tag{2.50}$$

The decoupled space and time dependence of Equation 2.49 is a property of the electric field distribution, where the voltage depends on the parameters of the particle. Equation 2.50 holds under the special circumstance where a particle traverses the accelerator instantaneously. When such a particle crosses the accelerator precisely at the moment of maximum field strength, it experiences a voltage of U_0. Accelerators are designed for specific particle velocities denoted as β and fixed charge-to-mass ratios $\frac{Q}{M}$. The acceleration can be visualized via a reference particle, named target particle, which crosses each gap center at a the design phase and corresponds to the phase position of the center of mass of the bunch. For this particle with velocity β, the equation can be expressed as:

$$U_a = \int_0^{L_C} E_{z,0}(z) \cos\left(\frac{\omega z}{\beta c}\right) \mathrm{d}z = T U_0 \tag{2.51}$$

Here, U_{a} represents the effective voltage, and T is referred to as the transit time factor, denoting the ratio of effective to maximum voltage. The design velocity, denoted as $\beta_{\mathrm{geometry}}$, is a critical parameter that influences the selection of existing accelerator designs for a project. The delay factor of single-cell structures increases with particle velocity and reaches its maximum for $\beta = 1$. In contrast, multi-cell structures reach their maximum at the design velocity β_{design}. These multi-cell cavities are designed for a specified operation case. Negative constant target phase structures keep the target particle on the target phase at each gap center. Therefore, the acceleration cell length increases with each cell. Constant *beta*-structures have a fixed design velocity and therefore constant acceleration cell length. This design choice is used for rebuncher cavities, which are operated at a constant target phase of 90° and therefore do not lead to energy gain. For HELIAC a constant β-design with a sliding movement in the longitudinal phase space, named EQUUS, was chosen [9]. Deviations from the design velocity lead to a decrease in the voltage that is used for energy gain and, consequently, a reduction in the transit time factor. This effect becomes more pronounced with an increasing number of accelerating cells, as each additional accelerating cell introduces additional constraints for the beam transport, thereby decreasing the velocity acceptance range, as shown in Figure 2.3.

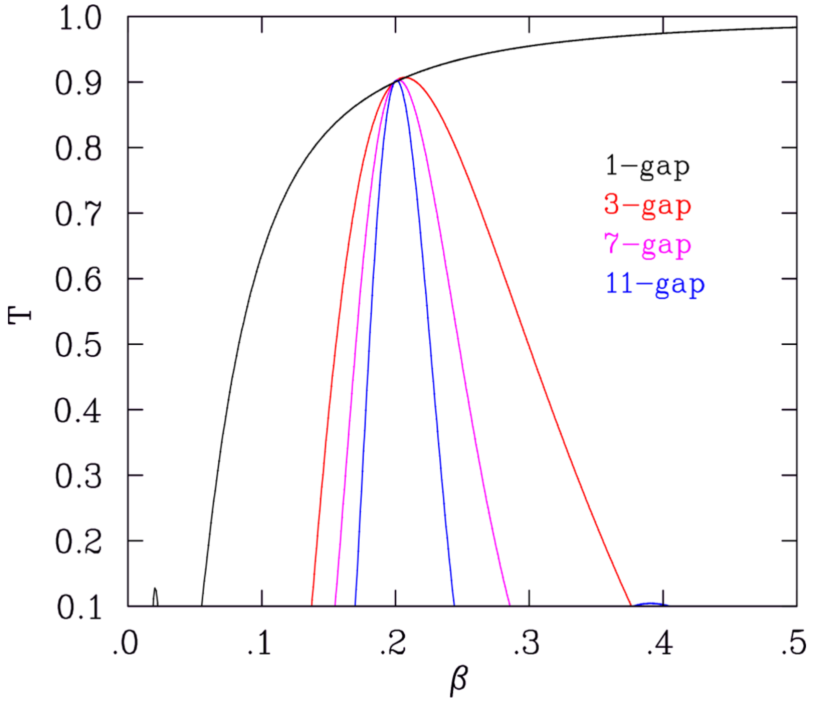

Figure 2.3: Tightening of the particle energy acceptance range intensifies with the number of acceleration gaps for a constant β structure.

In the case of the heavy ion accelerator HELIAC, the constant β EQUUS design allows for longitudinal focusing during acceleration. This is required due to the low particle velocities and the required compensation of space charge.

2.2.2 Shunt Impedance

The required electromagnetic fields in accelerators are excited by coupling to a high-frequency signal. The electric power is generally defined by:

$$P = U \cdot I \tag{2.52}$$

Here, an electric component has an impedance Z defined as:

$$Z = \frac{U}{I} \tag{2.53}$$

A cavity can be regarded as a parallel connected oscillating circuit with an ohmic resistance R, inductivity L, and capacity C. The impedance in this case is given by:

$$Z = \frac{1}{\frac{1}{R} + i\omega C - \frac{i}{\omega L}} \tag{2.54}$$

Since the cavity is operated at its resonance frequency ω_r, the imaginary parts cancel each other $\omega_\mathrm{r} C = \frac{1}{\omega_\mathrm{r} L}$, and the impedance is given by the ohmic part $Z = R$. The physical resistance of the accelerator tank is not a useful parameter for quantifying the efficiency of a particle accelerator. Instead, the acceleration voltage U_a depends on the required RF power P_c. In analogy to the impedance, Equation 2.52 and Equation 2.53 can be used to define the shunt impedance as:

$$R_\mathrm{a} = \frac{U_\mathrm{a}^2}{P_\mathrm{c}} \tag{2.55}$$

The shunt impedance is used to compare the RF efficiency of resonators at their respective operation mode. Linacs are commonly compared by a length-normalized shunt impedance:

$$R'_\mathrm{a} = \frac{Z_\mathrm{a}}{l} \tag{2.56}$$

The length l for normalization is not generally specified. The beta lambda definition $l = n\beta\lambda/2$ is used for $\beta\lambda/2$ structures with n gaps. This provides the physical gradient of the acceleration zone and is predominantly used to quantify the cavity's performance.

2.2.3 Quality Factor Q and Coupling Strength β

RF accelerators are damped harmonic oscillators that operate at the eigenfrequency ω_r of the resonator mode. The surface currents dissipate the power P_c and excite the electromagnetic field with energy W inside the resonator. When the RF power is turned off, the resonator's energy drops exponentially, following:

$$W(t) = W_0 \mathrm{e}^{-\frac{t}{\tau}} \tag{2.57}$$

The intrinsic quality factor Q_0 is defined as:

$$Q_0 = \frac{\omega_\mathrm{r} W}{P_\mathrm{c}} \tag{2.58}$$

The RF fields oscillate at the frequency $f_\mathrm{r} = \frac{\omega_\mathrm{r}}{2\pi}$, where $T = \frac{1}{f_\mathrm{r}}$ represents the time period of one full oscillation cycle. Q_0 is proportional to the ratio N of resonator energy W and energy loss TP per RF period duration.

$$Q_0 = \frac{\omega_\mathrm{r} W}{P} = \frac{2\pi W}{TP} = 2\pi N \tag{2.59}$$

The stored resonator energy W decreases to $\frac{1}{e}$ of its value after N RF periods:

$$W(NT) = W_0 \mathrm{e}^{-\frac{NT}{\tau}} = \frac{W_0}{e} \tag{2.60}$$

Measuring methods come to a limit when determining the quality factor of SC cavities. To understand this, the frequency-dependent spectrum can be approximated by the Lorentz function U(ω):

$$|U(\omega)| = \frac{|U_\mathrm{max}|}{\sqrt{1 + 4Q_0^2 \left(\frac{\omega - \omega_\mathrm{r}}{\omega_\mathrm{r}}\right)^2}} \tag{2.61}$$

The Lorentz function width depends on Q_0, reaches its maximum value U_max for $\omega = \omega_\mathrm{r}$, and decreases monotonically around ω_r. When $|U(\omega_\mathrm{3dB})| = \frac{|U_\mathrm{max}|}{\sqrt{2}}$, the important relation between Q_0 and ω_3dB is found:

$$2 = 1 + 4Q_0^2 \left(\frac{\omega_\mathrm{3dB} - \omega_\mathrm{r}}{\omega_\mathrm{r}}\right)^2 \Rightarrow Q_0 = \frac{1}{2} \frac{\omega_\mathrm{r}}{|\omega_\mathrm{3dB} - \omega_\mathrm{r}|} = \frac{\omega_\mathrm{r}}{\Delta\omega_\mathrm{3dB}} \tag{2.62}$$

The term '3dB' refers to the amplitude attenuation of the voltage amplitude by $\frac{1}{\sqrt{2}}$ with $\Delta\omega_\mathrm{3dB} = 2|\omega_\mathrm{3dB} - \omega_\mathrm{r}|$. The 3dB measurement method is used to determine the quality factor of a resonator. Figure 2.4 illustrates the tightening of the Lorentz curve with increasing Q_0.

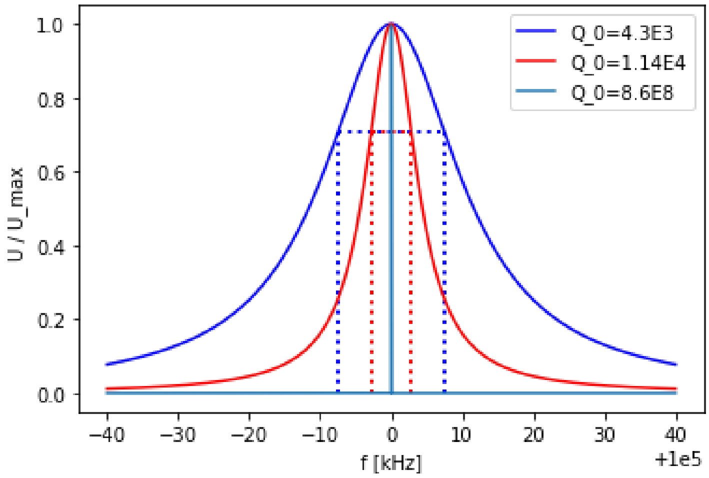

Figure 2.4: Lorentz function of the 360 MHz CH structure in case of normal conducting niobium, normal conducting copper, and SC niobium at 4 K. The theoretical value for the case of copper was calculated with $Q_{0,\text{copper}} = Q_{0,\text{niobium}} \cdot \sqrt{\frac{\rho_\text{copper}}{\rho_\text{niobium}}} = Q_{0,\text{niobium}} \cdot \sqrt{\frac{12.5 \times 10^{-8}\,\Omega\text{m}}{1.78 \times 10^{-8}\,\Omega\text{m}}}$

For SC cavities with typical quality factors above 10^8, the 3 dB frequency width becomes only a couple of Hz. Network analyzers are not capable of precisely resolving such narrow frequency intervals for the 3 dB method. For this purpose, using the field energy decay proves to be a precise tool to determine the quality factor, which will be discussed in Section 2.6.

The RF fields are excited by a coupler inside the cavity. The total power of the RF system that reaches the cavity is P_f, referred to as forward power. The RF fields inside the cavity interact with the coupler, resulting in RF power P_e being decoupled from the cavity and sent back to the RF system. A second coupler, called pickup, is used to evaluate the cavity field energy through the transmitted power P_t. The total power P_G that leaves and is dissipated by the cavity is given by:

$$P_\text{G} = P_\text{c} + P_\text{e} + P_\text{t} \tag{2.63}$$

The total power can now be associated with a quality factor Q_L similar to Q_0:

$$Q_\text{L} = \frac{\omega_\text{r} W}{P_{tot}} = \frac{\omega_\text{r} W}{P_\text{c} + P_\text{e} + P_\text{t}} \tag{2.64}$$

With Equation (2.64), the expression for the change of the quality factor because of the couplers is given by:

$$\frac{1}{Q_\text{L}} = \frac{P_\text{c} + P_\text{e} + P_\text{t}}{\omega_\text{r} W} \Rightarrow \frac{1}{Q_\text{L}} = \frac{1}{Q_0} + \frac{1}{Q_\text{e}} + \frac{1}{Q_\text{t}} \tag{2.65}$$

The external quality factors Q_e and Q_t are typically normalized by the intrinsic quality factor Q_0 of the cavity:

$$\beta_e = \frac{Q_0}{Q_\mathrm{e}} = \frac{P_\mathrm{e}}{P_\mathrm{c}} \tag{2.66}$$

$$\beta_t = \frac{Q_0}{Q_\mathrm{t}} = \frac{P_\mathrm{t}}{P_\mathrm{c}} \tag{2.67}$$

The powers P_e and P_t are not losses that are dissipating as heat like P_c. They are dependent on the interaction strength of each coupler, see section (2.4). The coupling strength β of a coupler can take values from 0 to a couple thousand, depending on the coupler and cavity type. The range of $\beta < 1$ is referred to as weak coupling, where the coupler's power flow through the coupler is smaller than the cavity's surface losses. The opposite is referred to as strong coupling, where $\beta > 1$. The special case of $\beta = 1$ is called critical coupling. With Equation (2.66) and Equation (2.67) Q_L can be rewritten as:

$$\frac{1}{Q_\mathrm{L}} = \frac{1}{Q_0}(1 + \beta_e + \beta_t) \tag{2.68}$$

The pickup is designed to decouple small amounts of power in relation to the cavity losses ($P_\mathrm{t} \ll P_\mathrm{c}$). This ensures negligible effects on the cavity behavior, which are crucial for the measurement of SC cavities. The coupling factor of the pickup, β_t, is much smaller than 1:

$$\frac{1}{Q_\mathrm{L}} = \frac{1}{Q_0}(1 + \beta_e) = \frac{1}{Q_0}(1 + \beta) \tag{2.69}$$

The coupling factor β_e is commonly abbreviated as β. The coupling strength determines the reflection coefficient for a steady-state cavity operated at its resonance frequency [24].

$$P_r = \left(\frac{\beta - 1}{\beta + 1}\right)^2 P_f \tag{2.70}$$

Equation (2.70) can be rearranged to get a solution for β:

$$\beta = \frac{1 \pm \sqrt{P_r/P_f}}{1 \mp \sqrt{P_r/P_f}} \tag{2.71}$$

The choice of the upper or lower signs in equation (2.71) depends on the coupling strength. For strong coupling, the upper signs should be used, while for weak coupling, the lower signs are appropriate. The coupling strength not only affects the steady-state power ratio of P_f and P_r, but also impacts the transient behavior of the cavity when RF power is switched on and off. First, we consider the case in which RF power is switched on at $t = 0$. The field energy is then given by:

$$W(t) = W_0 \left(1 - \exp\left(-\frac{t}{2\tau_L}\right)\right)^2 \tag{2.72}$$

The reflected power P_r is the net difference between the forward power P_f and the power that enters the cavity P_i:

$$P_r = P_f - P_i = P_f - \sqrt{\frac{4P_f\omega_0 W}{Q_\mathrm{e}}} + \frac{\omega_0 W}{Q_\mathrm{e}} \tag{2.73}$$

By substituting $\beta = \frac{Q_0}{Q_\mathrm{e}}$ into Equation 2.73, it can be rewritten as a function with the parameter β:

$$P_r = P_f\left(1 - \frac{2\beta}{(1+\beta)}\left(1 - \exp\left(-\frac{t}{2\tau_L}\right)\right)\right)^2 \tag{2.74}$$

The transient behaviour for P_r is shown in Figure (2.5):

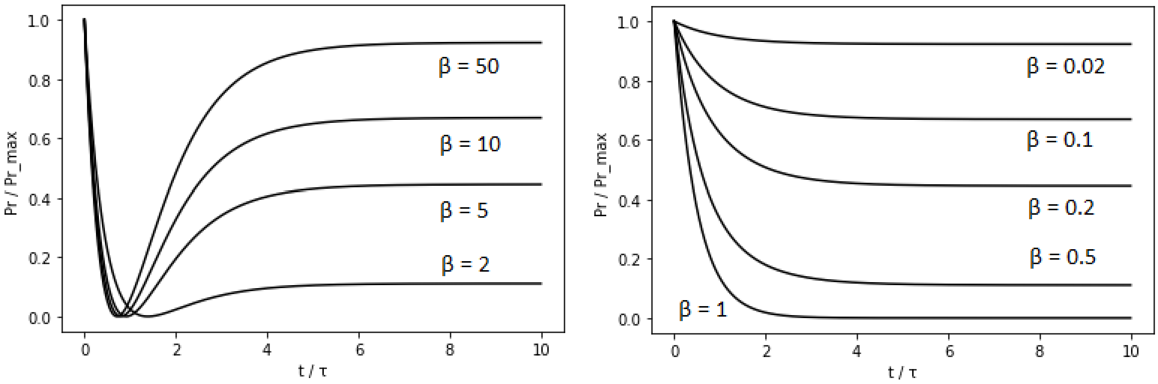

Figure 2.5: The reflection signal change for different β. In the left graph, the strong coupling case, and in the right graph, the weak case with β of equal steady state reflected power is shown.

For $t \gg \tau_L$, the reflection coefficient of equation (2.70) for the steady-state case is recovered:

$$P_r = P_f\left(1 - \frac{2\beta}{(1+\beta)}\right)^2 = P_f\left(\frac{1-\beta}{1+\beta}\right)^2 \tag{2.75}$$

Now we consider the cavity to be in the steady state with forward power P_f. The RF power is turned off, and the field energy will decrease:

$$W(t) = W_0\left(\exp\left(-\frac{t}{2\tau_L}\right)\right)^2 = W_0\exp\left(-\frac{t}{\tau_L}\right) \tag{2.76}$$

The reflected power is now given by the energy that is transmitted from the cavity through the coupler:

$$P_r = P_\mathrm{e} = \frac{\omega W(t)}{Q_\mathrm{e}} \tag{2.77}$$

Equation (2.77) can now be rewritten with equation (2.76) and $\beta = \frac{Q_0}{Q_\mathrm{e}}$ as:

$$P_r = P_\mathrm{e} = \frac{4\beta^2}{(1+\beta)^2} P_f \exp\left(-\frac{t}{\tau_L}\right) \tag{2.78}$$

For $t = 0$, Equation (2.77) can be used to calculate β from P_f and P_r.

$$\beta = \frac{1}{2\sqrt{\frac{P_f}{P_r}} - 1} \tag{2.79}$$

The advantage of Equation 2.79 is that it does not require extra knowledge about the coupling strength.

2.2.4 Geometry Factor R/Q

Particles are accelerated by the electric field component aligned with the beam axis. Therefore, an important cavity property is the concentration of the electric field on the beam axis. The ratio of impedance to quality factor quantifies this effect. The R/Q value is a geometric factor that can be used to compare cavities of different types in terms of efficiency.

$$\frac{R_a}{Q_0} = \frac{U_a^2}{\omega_\mathrm{r} W} = \frac{\left(\int E_z \cos\left(\frac{\omega_0 z}{\beta c}\right) dz\right)^2}{\frac{1}{2}\omega_\mathrm{r}\epsilon_0 \int_V |\mathbf{E}|^2 dV} \tag{2.80}$$

Drift tube structures increase R/Q with smaller apertures, which means more electric field of a given mode will be focused onto the beam axis and therefore increase the gradient for a certain power level.

In the case of superconducting drift tube cavities, RF breakdown is the limiting factor of performance. This leads to geometry optimization, which also includes the reduction of electric and magnetic peak fields. Electric peak fields are reduced by smoother surfaces and can be adjusted by variation of drift tube edge and aperture radius. An increase in R/Q by adjusting the two mentioned parameters will also lead to higher electric peak fields and must be carefully considered during the design phase.

2.2.5 Geometry Factor G

The intrinsic quality factor of a cavity is dependent on its frequency, surface resistance, dimensions, and geometry. This relationship can be demonstrated by rewriting Equation 2.58 with $P_\mathrm{c} = \frac{1}{2}R_s \int_S |\mathbf{H}|^2 dA$ and $W = \frac{1}{2}\mu_0 \int_V |\mathbf{H}|^2 dV$.

$$Q_0 = \frac{\omega_\mathrm{r}\mu_0 \int_V |\mathbf{H}|^2 dV}{R_s \int_S |\mathbf{H}|^2 dA} \tag{2.81}$$

The surface resistance itself depends on the resonance frequency. By eliminating R_s, we obtain the geometry factor G:

$$G = R_s Q_0 = \frac{\omega_\mathrm{r} \mu_0 \int_V |\mathbf{H}|^2 dV}{\int_S |\mathbf{H}|^2 dA} \tag{2.82}$$

G is dependent on the geometry but not the size of the cavity. This can be demonstrated by a uniform linear scaling of the cavity dimensions [25].

$$G \propto \frac{\omega_\mathrm{r} \mu_0 \int_V |\mathbf{H}|^2 dV}{\int_S |\mathbf{H}|^2 dA} \propto \omega_\mathrm{r} \frac{\alpha^3}{\alpha^2} \propto \omega_\mathrm{r} \alpha \propto \frac{\omega_\mathrm{r}}{\omega_\mathrm{r}} \propto \mathrm{const} \tag{2.83}$$

The use of an RF parameter that does not include the surface resistance is especially useful for comparing superconducting cavity geometry since the surface resistance, and therefore the intrinsic quality factor can vary greatly for the same structure.

2.3 Choice of Technology for Low Beta Accelerator Sections

This section examines the advantages and disadvantages of SC and NC technologies for RF linacs in the low to medium beta range. High-energy sections predominantly rely on superconducting SC elliptical cavities due to the absence of efficient normal conducting NC structures, for CW operation, in the high beta range. NC H-mode cavities exhibit a shunt impedance proportional to $1/\beta$, and their RF losses can, in general, not compete with SC elliptical cavities for continuous wave (CW) or pulsed operation. An exception to this case is given by very low β IH-structures ($\beta < 0.1$), which can compete in total grid power consumption. More information on IH structures can be found in [26]. If a high-energy section is part of the linac or the necessary infrastructure already exists, it shifts the SC threshold to lower energies.

Operating a superconducting linac requires expensive infrastructure like a cryogenics plant with an associated helium distribution and recovery system. Additionally, the accelerator components installed into cryo modules are not easily accessible after assembly. Research and development (R&D) of SC low β structures must account for additional effects like microphonics, Lorentz-force detuning, peak fields, and field emissions. This leads to increased setup times compared to normal conducting linacs. SC cavities are highly sensitive to surface cleanliness and require cleanroom setups with the corresponding expensive infrastructure, including ventilation systems, clean room inventory, ultrasonic baths, and HPR to perform tasks on open cavities. A task of 30 minutes on a normal conducting cavity can require up to multiple days when the cavity and new parts have to be inserted into the clean room and undergo HPR after installation. In the case of high-power accelerators, RF losses in NC cavities represent a dominating cost factor of the entire facility and require sophisticated cavity cooling systems. The choice between normal conducting and superconducting technology depends on various parameters:

1. Particle energy
2. Beam power
3. Beam current
4. Duty factor
5. Linac length

Generally, the beam energy and the cavity duty cycle are the predominant parameters for determining the appropriate cavity technology. During low-duty factor operation, also referred to as pulsed operation, normal conducting cavities can reach high gradients, up to 10 MV/m. As CW operation is approached, the achievable gradients drop significantly to around 1 MV/m. The particle energy naturally changes with the progression of the accelerator. When threshold energy is reached, the transition from NC to SC cavities becomes gradually more economically viable as β further increases. For example, the parameters of the 360 MHz CH cavity will be used to compare SC versus NC operation for different acceleration voltages. Calculations of cavity losses for both cases can be performed using the R/Q value of the cavity. The advantage lies in the fact that R/Q represents the efficiency of the geometry and is independent of surface resistance, which can vary significantly between the NC and SC case.

$$P_{\mathrm{c}} = \frac{U_a^2}{R_a} = \frac{U_a^2}{\left(\frac{R_a}{Q_0}\right) Q_0} \tag{2.84}$$

In both cases, the efficiency of the RF amplifier must be taken into account, which is typically $\eta_{amp} = 0.6$. Additional losses in the case of SC operation arise from static heat flux due to imperfect insulation, $P_{static} = 15\,\mathrm{W}$. The efficiency of the cryogenic system is estimated by:

$$\eta_{cryo}(T) = \frac{T}{293\,\mathrm{K} - T} \cdot 0.25 \tag{2.85}$$

This results in $\eta_{cryo}(4K) = 0.003$ for helium operation at 4 K. The total power consumption, which includes cavity, duty factor *df* and static cryogenic losses, is calculated as:

$$P_{Grid}(T) = \left(\left(\frac{U_a^2}{(\frac{R_a}{Q_0}) Q_0(T)} \right) \cdot \frac{df}{\eta_{amp}} + P_{static} \right) / \eta_{cryo}(T) \tag{2.86}$$

The quality factor of the 360 MHz niobium CH cavity has been measured at room temperature, yielding $Q_0 = 4300$. We can extrapolate the quality factor for the cavity if it was built from copper, resulting in $Q_0 = 11400$. The quality factors for the SC case are taken from post-HPR measurements. The 360 MHz cavity design is optimized for SC operation, which includes the reduction of peak fields. Normal conducting cavities are optimized towards higher shunt impedance and Q values. The R/Q of NC CH structures is very similar to the SC 360 MHz CH cavity, but intrinsic quality factors are higher, with $Q_0 = 17000$, compared to the extrapolated value of $Q_0 = 11400$. For the following comparison shown in Table 2.2, the parameters of the 360 MHz SC CH cavity and NC CH structures for CW operation have been used.

	NC			SC			
Losses Voltage	$Q_0/10^4$	P_c/kW	P_{Grid}/kW	$Q_0/10^8$	P_c/W	P_{Grid}/kW	P_{nc}/P_{sc}
1 MV	1.70	18.50	30.83	6.15	0.51	3.14	9.82
2 MV	1.70	73.99	123.32	6.08	2.07	3.89	31.70
4 MV	1.70	295.97	493.28	5.87	8.57	7.02	70.27
6 MV	1.70	665.93	1109.00	5.20	21.00	13.38	82.88

Table 2.2: Comparison of the power required to operate a 360 MHz CH cavity for each technology with a duty cycle of 100%. The normal conducting cases of 4 and 6 MV are purely hypothetical because thermal loads can not be handled by water cooling systems. The case of 2 MV/m is also extremely optimistic for NC CW operation. Still, the cavity losses could be handled by a water-cooled cavity that is constructed entirely from copper.

Most NC high beam power linacs are operated pulsed. Decreasing duty cycle *df* increasingly favors NC operation for two reasons: the maximum electric field gradient increases in pulsed NC operation, and the decrease of consumed grid power is greater than in the SC case. When the duty factor approaches zero, the room temperature NC cavity losses linearly approach zero but the SC losses approach the static losses of the cryogenics system. R&D on SC low β drift tube linac (DTL) structures over the past decades have led to a variety of sophisticated and matured designs. The most widely researched cavity types around the world are QWR, HWR and Spokes. These structures typically have two gaps and lead to longer drift lengths in the accelerator. In contrast, SC CH structures are compact structures, allowing for flexible adjustment of gap numbers and offering high acceleration efficiency. For example, the 360 MHz CH prototype cavity has 19 gaps with an acceleration length of $l = 0.791$ m and a voltage of 6.72 MV over the total cavity length of 1 m. The 217 MHz demonstrator (CH0) of HELIAC has 15 gaps over $l = 0.612$ m inner acceleration length with a voltage of 5.88 MV over the total cavity length of 0.863 m.

A promising new concept of NC accelerator technology is currently in the research phase at IAP Frankfurt. 3D-printed interdigital H-mode (IH) structures are expected to deliver higher gradients in pulsed operation at cryogenic temperatures compared to room temperature for the same RF power. Increased maximum gradients are expected due to operation at cryogenic temperatures. The quality factor of a 340 MHz copper-plated and vacuum-annealed pillbox cavity was measured in the temperature range of 4 K to 296 K [27].

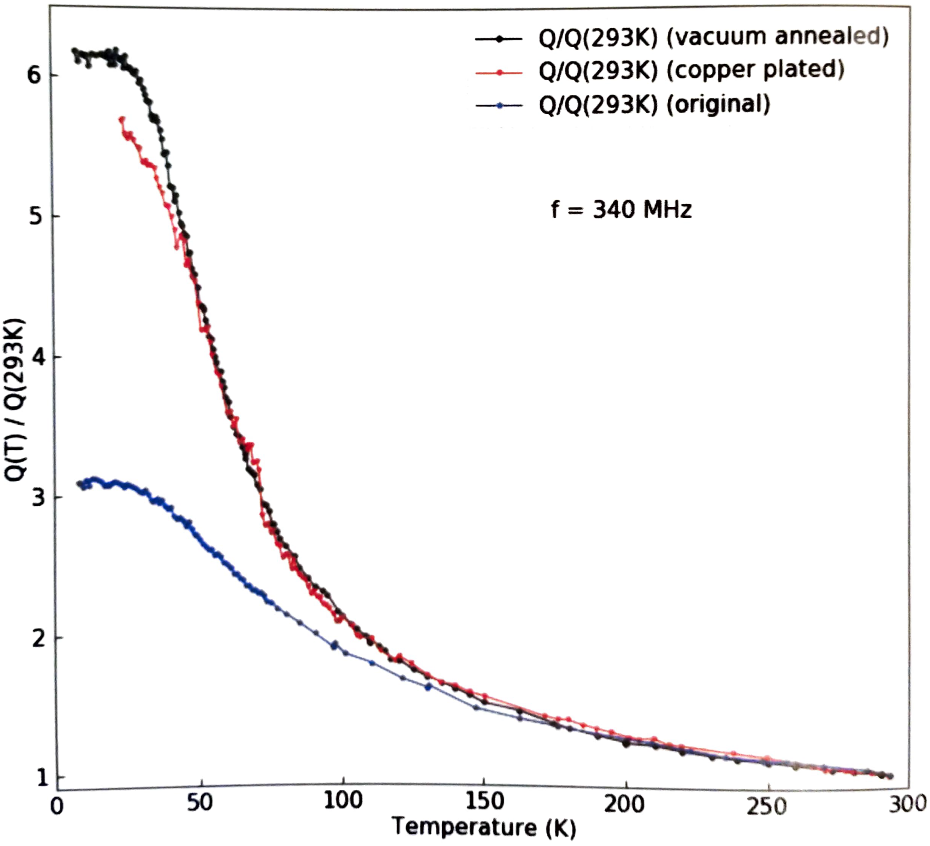

Figure 2.6: Intrinsic quality factor of a 340 MHz quarter wave copper resonator. [27]

Similar to the case of SC vs. NC operation, the efficiency change due to cryogenic operation can be estimated. A 433 MHz 3D printed IH cavity has been tested and showed an effective shunt impedance of 195.8 MΩ/m, which is competitive with conventional IH-cavities [28]. Since $R_a/Q_0 = const$, and the increase of R_a is proportional to Q_0, the decrease in required RF power is proportional to $1/(Q_0(T)/Q_0(293K))$. The total RF power consumption of NC operation at cryogenic temperatures can be calculated using the adjusted form of Equation 2.86:

$$P_{Grid}(T) = \left(\frac{U_a^2}{\left(\frac{Q_0(T)}{Q_0(293K)}\right) R_{a,293K}} \cdot \frac{df}{\eta_{amp}} + P_{static} \right) / \eta_{cryo}(T) \tag{2.87}$$

For Table 2.3, a pulsed normal conducting accelerator is considered with $E_a = 15\,\mathrm{MV/m}$, $I_{beam} = 15\,\mathrm{mA}$ at a duty factor of $df = 0.001$.

T/K	η_{cryo}	$Q_0(T)/Q_0(293K)$	$P_{Grid}(T)/(kW/m)$	$P_{\mathrm{Grid}}(T)/P_{\mathrm{Grid}}(293\,\mathrm{K})$	$P_{\mathrm{Grid}}(T)/P_b$
100	0.130	2.2	6.797	3.55	33.1
77	0.089	2.9	7.522	3.93	29.9
61	0.066	3.5	8.476	4.43	26.5
50	0.051	4.5	8.468	4.42	26.6
37	0.036	5.7	9.575	5.00	23.5

Table 2.3: With $P_\mathrm{c}(293\,\mathrm{K}) = 1.92\,\mathrm{kW/m}$ the cryo system is shown to increase the grid power consumption by RF losses. However, because of $P_b = 225\,\mathrm{kW/m}$, the beam power consumption dominates across the temperature spectrum.

In the case of normal conducting cavities at low temperatures, the grid power consumption is not lowered compared to operation at room temperature. The increase in intrinsic quality factor increases the shunt impedance and, therefore, the electric field for the same input power. For the required duty factor of $df = 0.001$, the required peak power is 1.92 MW/m in case of room temperature operation and 426.6 kW/m in case of operation at $T = 50\,\mathrm{K}$.

2.4 RF Coupling

The coupler is a device that inserts RF power by exciting the electromagnetic field of the operation mode. The coupling strength β_e is given by the power P_e that the coupler transmits into the cavity relative to the cavity losses P_c. This depends on the coupler's geometry and the cavity field at the coupler. The coupling strength influences the total quality factor of the resonator by:

$$\frac{1}{Q_\mathrm{L}} = \frac{1}{Q_0}(1 + \beta_e) \tag{2.88}$$

In NC cavities, RF power represents a significant portion of the operational costs. Therefore, the design strength of the coupler is chosen to be critical with $\beta = 1$ to avoid unnecessary reflected power. The high intrinsic quality factors, $Q_0 > 10^8$, of sc cavities result in extremely narrow frequency bandwidths, making it challenging for an RF control system to keep the cavity in resonance. This issue is resolved by employing strong coupling. The lower quality factor of the coupler widens the frequency bandwidth of the cavity at the cost of higher reflected RF power.

Another critical case for strong coupling is given by high-power beam loading. The additional power P_B diminishes the total quality factor:

$$\frac{1}{Q_\mathrm{L}} = \frac{1}{\omega_0 W}(P_\mathrm{c} + P_\mathrm{e} + P_B) = \frac{1}{Q_0}(1 + \beta_e + \beta_B) \tag{2.89}$$

The effect on the total coupling strength depends on the ratio $\beta_B = P_B/P_\mathrm{c}$. For NC cavities with moderate beam power, the effect on the total coupling strength is negligible, as the cavity losses are significantly larger than the beam power. For SC cavities, the beam losses are much greater than the cavity losses and result in necessary coupling strengths of $\beta > 1000$. This strong coupling does not allow for effective operation without beam loading, which is necessary for RF conditioning and measuring RF parameters before the first beam time. For this reason, SC cavities are equipped with at least two couplers: one coupler is designed without beam loading, and the other is designed to work with beam loading. The two most prominent coupling methods are inductive and capacitive coupling. All SC CH cavities are operated via capacitive coupling and therefore only this method will be explained in the next section.

Capacitive Coupling

Capacitive coupling involves the interaction of the coupler with the electric field of the resonator. While the coupler is positioned inside the beam pipe for elliptical structures, low-energy structures have couplers positioned inside the resonator. The RF is transmitted via a coaxial cable and the coupler is connected to the inner conductor. The coupler reaches inside the cavity and interacts with the electrical field in its vicinity. RF cables are standardized to $50\,\Omega$ to prevent reflection at their connection. This standard also applies to the coupler. The impedance of a coaxial waveguide is given by

$$Z = \sqrt{\frac{L}{C}} = \sqrt{\frac{\mu_0(\ln(b/a))^2}{4\pi^2\epsilon_0}} = \frac{\ln(b/a)}{2\pi}\sqrt{\frac{\mu_0}{\epsilon_0}} \tag{2.90}$$

where a is the radius of the inner conductor, and b the radius of the outer conductor. The condition of $Z = 50\,\Omega$ leads to the radii ratio:

$$\frac{b}{a} \approx 2.3 \tag{2.91}$$

The coupler distorts the electric field of the cavity. The electric field of the respective mode is bent towards the coupler surface. The induced charge can typically only be calculated from numerical simulations by solving Maxwell's Equation (2.1):

$$\nabla \cdot E = \frac{\rho}{\epsilon_0} \tag{2.92}$$

$$\rho = \epsilon_0 \nabla E \tag{2.93}$$

$$q = \epsilon_0 \int_V \nabla E dV = \epsilon_0 \int_S E dA \tag{2.94}$$

In the case of the E_{010} mode, the electric field exclusively has a z-component, and the coupler is positioned parallel to the electric field. A simplification allows us to find an analytical expression for the quality factor Q_e. For this, the electric field is considered to be uniform (with E_0) and interacts exclusively with the top surface of the coupler. The RF electric field oscillates with the mode frequency ω:

$$E(t) = E_0 \cdot \exp(i\omega t) \tag{2.95}$$

The induced charge on the top of the coupler results in:

$$q(t) = \epsilon_0 E_0 A_{C,top} \exp(i\omega t) \tag{2.96}$$

RF losses from the surface current ($I(t) = \dot{q}(t)$) are given by:

$$\langle P \rangle = \frac{1}{2} Z \langle I \rangle^2 = \frac{50\Omega}{2} \left(\frac{\epsilon_0 \omega E_0 A_{C,top}}{\sqrt{2}} \right)^2 = 50\pi^4 = 100\pi^4 \epsilon_0^2 f^2 E_0^2 a^4 \tag{2.97}$$

Field energy W of the cavity flows through the coupler and has to be derived from numerical simulation of the cavity. The expression for Q_e in this case is:

$$Q_\mathrm{e} = \frac{\omega W}{P} = \frac{W}{50\Omega\pi^3 \epsilon_0^3 f E_0^2 a^4} \tag{2.98}$$

2.5 Coupler Redesign

Initial baseline measurements of the 360 MHz cavity showed strong coupling with $\beta > 30$ at 4 K. The original power coupler with $\beta = 4.5$ was no longer available, and a redesign of the coupler was necessary. Post cold test, the cavity was inserted into the clean room at IAP and the coupler was removed to measure its geometry. The diameter of the stem is fixed at 4.2 mm to ensure an impedance of 50 Ω. The head height ($h = 4\,\mathrm{mm}$), diameter ($d = 8\,\mathrm{mm}$), and roundings ($r = 1\,\mathrm{mm}$) were taken from the original design. The stem and headpiece are connected via the threaded top piece of the stem, as shown in Figure 2.7.

Figure 2.7: On the left side, the original heavily overcoupled coupler is shown. In the middle are the dummy couplers of decreasing length. On the right are couplers for critical coupling at room temperature.

The new coupling strength is required to be strong with β in the range of 3 to 8 for an estimated intrinsic value $Q_0 = 6 \times 10^8$. At room temperature (RT), the intrinsic quality factor is lowered by multiple magnitudes to 4.3×10^3. The measurement of the dummy couplers and the final coupler at room temperature inside the clean room requires a coupler that is ideally critical with $\beta = 1$. A series of longer stems and two headpieces with bigger diameters were built to find a configuration where the critical coupling is achieved. The measurement of the dummy coupler quality factor was performed via a network analyzer inside the clean room at IAP.

S-Parameter

A network analyzer is used to determine the RF parameters of devices. It generates an RF signal that is sent through port 1 to the cavity, where it is, in general, partly reflected and transmitted. The reflected signal is measured through port 1 of the network analyzer, and the transmitted signal is measured in port 2 of the network analyzer. Figure 2.8 shows a schematic representation of the measurement.

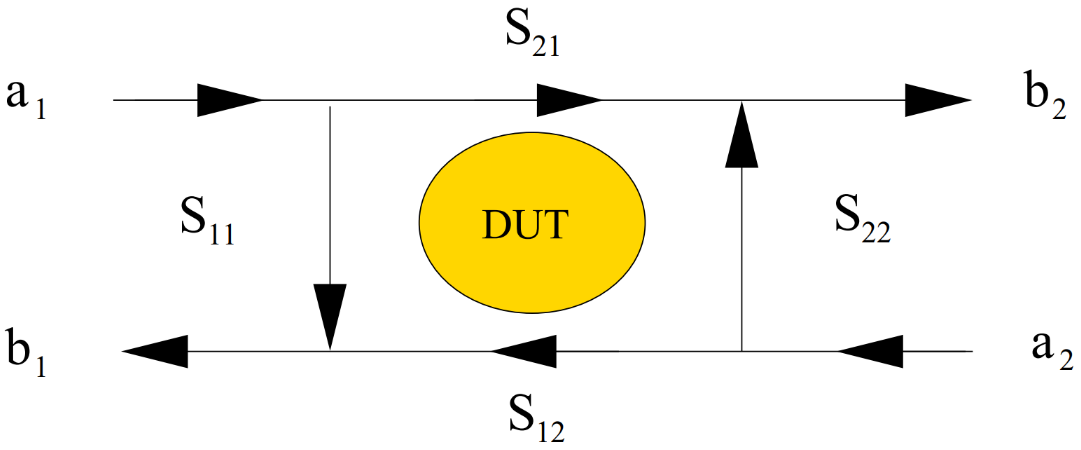

Figure 2.8: The **D**evice **U**nder **T**est (DUT) partly reflects the output signal a_1 of the network analyzer. The transmitted signal could be reflected from port 2 of the analyzer and is considered as an incoming signal a_2 to the DUT. This signal itself gets partly reflected and transmitted by the DUT.

This can be described by a 2x2 matrix $\tilde{\mathbf{S}}$, which contains the scattering parameters S_{ij}:

$$\begin{pmatrix} b_1 \\ b_2 \end{pmatrix} = \begin{pmatrix} S_{11} & S_{12} \\ S_{21} & S_{22} \end{pmatrix} \begin{pmatrix} a_1 \\ a_2 \end{pmatrix} \tag{2.99}$$

The equations can be solved for S_{11} and S_{21}:

$$S_{11} = \frac{b_1 - S_{21} a_2}{a_1} \tag{2.100}$$

$$S_{21} = \frac{b_2 - S_{22}a_2}{a_1} \tag{2.101}$$

Since port 2 of the network analyzer is $50\,\Omega$, there is no reflection of the transmitted cavity signal at the analyzer port 2 ($a_2 = 0$). The network analyzer measures the RF signal's voltage and results in the power $P_i = \frac{U_i^2}{Z_i}$ with $Z_i = 50\,\Omega$ for all components. The scattering parameters can, therefore, be rewritten as a ratio of RF power:

$$|S_{11}| = \left|\frac{b_1}{a_1}\right| = \sqrt{\frac{P_r}{P_f}} \tag{2.102}$$

$$|S_{21}| = \left|\frac{b_2}{a_1}\right| = \sqrt{\frac{P_\mathrm{t}}{P_f}} \tag{2.103}$$

S-parameters represent ratios of scattered waves in relation to the initial RF wave sent to the DUT. Scattering and RF losses result in attenuation, denoted as D, of the received signal compared to the initial signal. The attenuation D is a parameter that is based on the logarithmic scale with a base of 10 and is specified in decibels (dB):

$$D[dB] = 10 \cdot \log_{10}\left(\frac{P_2}{P_1}\right) \tag{2.104}$$

Using Equation(2.104), S-parameters can now be expressed in dB as:

$$|S_{11}| = \sqrt{\frac{P_r}{P_f}} = 10^{S_{11}[dB]/20} \tag{2.105}$$

$$|S_{11}|^2 = \frac{P_r}{P_f} = 10^{S_{11}[dB]/10} \tag{2.106}$$

Suppose we have a power level P_1 that is diminished by an attenuation D_1 to the power level P_2. When attenuations are serially connected, D_2 affects P_2, and so on. The total attenuation D_G is therefore the product of all D_i:

$$|D_G| = \prod_{i=0}^{N} |D_i| \tag{2.107}$$

The attenuation $D_G[dB]$ results from addition of all $D_i[dB]$:

$$D_G[dB] = \sum_{i=0}^{N} D_i[dB] \tag{2.108}$$

Attenuation $D[dB]$ represents a relative change in signal strength. To convert relative dB values to an absolute measure of power, we need to know the initial power level, which is commonly defined as $P_1 = 1\,\mathrm{mW}$ and specified in dBm. The RF powers P_f, P_r, and P_t can be expressed interchangeably in either watt (W) or dBm, and the relation between dBm and watt is shown in Figure 2.9.

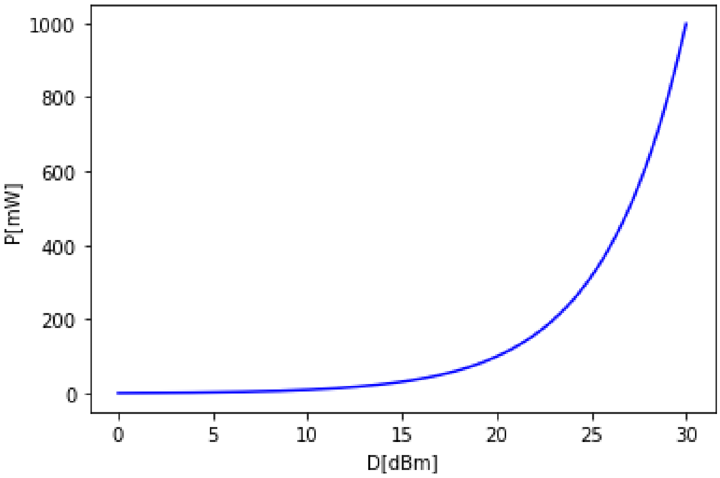

Figure 2.9: Illustrates the relation between $P[W]$ and $D[dBm]$.

As a rule of thumb, every increase of 3 dB, results in a doubling of the power, and every increase of 10 dB corresponds to a tenfold increase in power. Equations 2.71 and 2.102 allows for the calculation of β through network analyzer measurements:

$$\beta = \frac{1 \pm |S_{11}|}{1 \mp |S_{11}|} \tag{2.109}$$

The quality factor Q_e of the coupler results in:

$$Q_e = \frac{Q_0}{\beta} = Q_L \left(\frac{1+\beta}{\beta} \right) = Q_L \left(\frac{1 + \frac{1 \pm |S_{11}|}{1 \mp |S_{11}|}}{\frac{1 \pm |S_{11}|}{1 \mp |S_{11}|}} \right) \tag{2.110}$$

Equation 2.110 requires a coupling strength that yields sufficient RF power transmission into the cavity. This requires the quality factor Q_e to be reasonably close to Q_0, see figure 2.5. The intrinsic quality factor of SC cavities at room temperature is several magnitudes lower than at 4 K. The coupling strength at room temperature is so low, that almost no RF power is transmitted into the cavity and no resonance will be detectable in S_{11}. In the case of the 360 MHz CH cavity, the pickup was replaced by a coupler that is designed to be critical at room temperature. The coupler for operation at 4 K was now treated as a pickup:

$$Q_t = \frac{\omega W}{P_t} = Q_0 \frac{P_c}{P_t} \tag{2.111}$$

The cavity losses P_c are given by:

$$P_c = P_f - P_r - P_t \tag{2.112}$$

Equations 2.111 and 2.112 yield

$$Q_\mathrm{t} = Q_0 \left(\frac{P_f - P_r - P_\mathrm{t}}{P_\mathrm{t}} \right) = Q_0 \left(\frac{1 - \frac{P_r}{P_f} - \frac{P_\mathrm{t}}{P_f}}{\frac{P_\mathrm{t}}{P_f}} \right) \tag{2.113}$$

With the definition of the S-parameters in Equations 2.102 and 2.103, Q_t can be calculated from the measured S-parameters:

$$Q_\mathrm{t} = Q_0 \left(\frac{1 - |S_{11}|^2 - |S_{21}|^2}{|S_{21}|^2} \right) = Q_\mathrm{L}(1+\beta_e) \left(\frac{1 - |S_{11}|^2 - |S_{21}|^2}{|S_{21}|^2} \right) \tag{2.114}$$

Since the pickup is designed to have very low coupling strength $\beta_t \ll 1$, S_{21} can be neglected:

$$Q_\mathrm{t} = Q_\mathrm{L}(1+\beta_e) \left(\frac{1 - |S_{11}|^2}{|S_{21}|^2} \right) \tag{2.115}$$

Dummy Coupler Results

The experimental setup included the 360 MHz cavity located inside the clean room and two n-cables that connected the cavity to a network analyzer inside the material lock. The network analyzer can not be inserted into the clean room due to dust inside the casing. Before insertion into the clean room, the cavity, dummy couplers, and cables were cleaned by degreasing with acetone and isopropanol and removal of residual particles using pressurized nitrogen. The pickup for operation at 4 K was removed from the RF feedthrough and coupling strength was tested with different stem lengths and headpiece diameters.

Optimal coupling was achieved with a stem length $l = 150\,\mathrm{mm}$ and a headpiece diameter of $d = 12\,\mathrm{mm}$. This configuration resulted in $S_{11} = -29.24\,\mathrm{dB}$ and $\beta_e = 0.93$. The loaded quality factor was determined using the 3-dB method, resulting in $Q_\mathrm{L} = 2224$. This led to an intrinsic quality factor of $Q_0 = 4292$, which is consistent with past RF measurements and CST simulations. The results were cross-verified using a different coupler configuration with the same stem length and smaller headpiece diameter ($d = 10\,\mathrm{mm}$) with $\beta_e = 0.30$, resulting in $Q_\mathrm{L} = 3204$ and $Q_0 = 4298$. The headpiece with $\beta_e = 0.93$ was used to measure the dummy couplers, and the results are shown in Table 2.4.

length[mm]	$\|S_{21,r=12\,\mathrm{mm}}\|$[dB]	$\|S_{21,r=10\,\mathrm{mm}}\|$[dB]	$Q_{t,r=12\,\mathrm{mm}}$	$Q_{t,r=10\,\mathrm{mm}}$
130	34.53	35.7	1.22×10^7	1.15×10^7
128.5	47.53	49.92	2.43×10^8	3.16×10^8
127	60.66	60.1	5×10^9	3.16×10^9

Table 2.4: Displays the measured quality factors of the dummy couplers for two different couplers. The headpiece diameter was maintained at $r = 0.8\,\mathrm{mm}$. The previously installed coupler showed $Q_\mathrm{L} = 1,37 \cdot 10^7$ at 4 K with $\beta_e \geq 30$. In cases of such strong coupling, Q_L is approximately equal to the quality factor of the coupler: $Q_\mathrm{e} \approx Q_\mathrm{L} = 1.37 \times 10^7$.

The previously installed RF coupler with $l = 130\,\mathrm{mm}$ was initially shortened to $l = 128.5\,\mathrm{mm}$ from $l = 130\,\mathrm{mm}$ and resulted in $Q_{128.5\,\mathrm{mm}} = 2.42 \cdot 10^8$ from $Q_{130\,\mathrm{mm}} = 1.37 \cdot 10^7$. The intrinsic quality factor of the cavity was assumed to be equal to prior measurements in 2008 with $Q_0 = 6.5 \cdot 10^8$. The coupler was then further shortened to $l = 128.3\,\mathrm{mm}$ and resulted in the final quality factor of $Q_{128.3\,\mathrm{mm}} = 2.02 \cdot 10^8$.

2.6 Measurement of Q_0 and β at 4K

The quality factor that can be directly measured by any method is Q_L. In the case of very weak coupling, where $Q_\mathrm{e} \gg Q_0$, the total quality factor is approximately equal to the intrinsic quality factor: $Q_\mathrm{L} \approx Q_0$. The 3 dB measurement method would therefore directly yield Q_0. However, the measurement of the 3 dB frequency width, as discussed in Section 2.2.3, may not lead to accurate results in the case of SC cavities. In fact, even in the case of the strongly over-coupled 360 MHz cavity with $Q_\mathrm{L} = 10^7$, the 3 dB measurement could only roughly identify the power of Q_L. The design coupling strength for SC cavities is always strong with $\beta > 1$. The degree of over-coupling depends on the application. For RF power tests at 4 K, the coupling strength typically falls in the range of $1 < \beta < 10$ to account for the Q slope at medium and high field levels. At high field levels, the intrinsic quality factor drops exponentially with increasing field emission. Once the coupling strength transitions from strong to weak, the forward power required to increase field levels increases significantly due to decreasing β and an increase in P_r. The measurement of all relevant RF parameters required to determine Q_0 and the confirmation of strong coupling is achieved by the cavity response to low-level RF pulses. The cavity response for weak, critical, and strong coupling is illustrated in Figure 2.10.

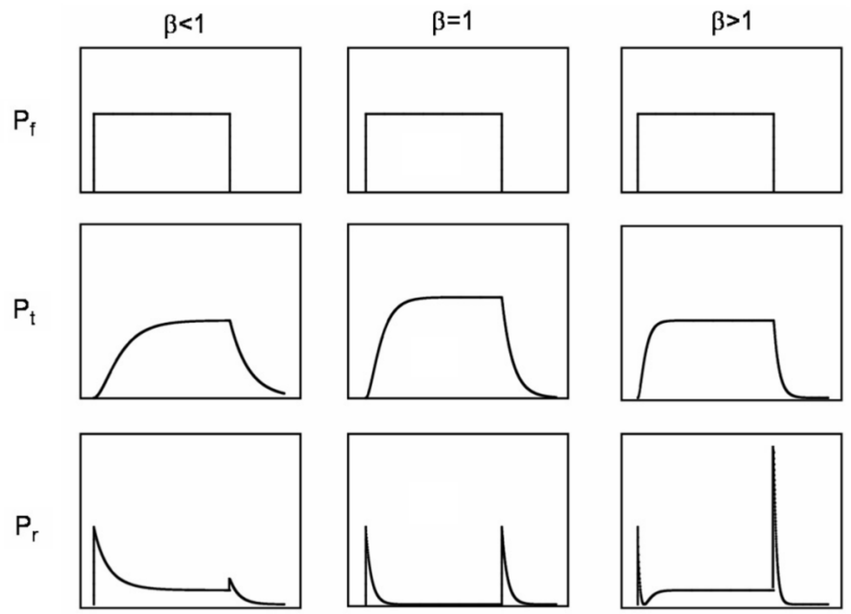

Figure 2.10: Cavity response to an RF pulse for all coupling cases.

The reflection always initially peaks at $P_r = P_f$ for any coupling case when RF power is turned on and then approaches the steady state reflection power. Once the RF power is switched off, a second reflection peak is observed. The stored field energy flows through the coupler and with increasing β, the RF power transmitted becomes larger. In the case of weak coupling, the second peak is smaller than the first peak, and vice versa. For critical coupling, the peak heights are equal to each other. The cavity response is recorded with an oscilloscope, which measures the voltage of the RF pulses. Using the relationship $P \propto U^2$, Equation 2.79 can be adapted to calculate β from the voltage peak heights.

$$\beta = \frac{1}{2\frac{U_f}{U_r} - 1} \tag{2.116}$$

The final parameter to be determined is Q_L. When the RF power is turned off, the transmitted power P_t declines exponentially with $P_\mathrm{t} \propto W(t) \propto \exp\left(\frac{t}{2\tau_L}\right)$. The same argument, made for the reflection signal earlier, holds true for the transmitted signal: The oscilloscope measures the voltage:

$$U(t) \propto \sqrt{P_\mathrm{t}} \propto \exp\left(-\frac{t}{2\tau_L}\right) \tag{2.117}$$

The time difference $\Delta t = t_2 - t_1$ between the values $U(t_1)$ and $U(t_2)$, with the condition $U(t_2) = U(t_1)/e$ results in $\Delta t = 2\tau_L$. The quality factor Q_L is given by:

$$Q_\mathrm{L} = 2\pi f \tau_L = \pi f \Delta t \tag{2.118}$$

The intrinsic quality factor can now be calculated using Equation 2.69:

$$Q_0 = Q_{\mathrm{L}}(1 + \beta) \tag{2.119}$$

In contrast to NC cavities, SC cavities do not have a constant intrinsic quality factor with increasing field levels. The Q-slope is discussed in detail in Section (5.6.3). The quality factor has a field level range in which its value is maximum, and this is always at low to medium field levels. There is a cutoff towards lower field levels, where the quality factor decreases sharply and rapidly. In the case of the 360 MHz CH cavity, this effect was observed for forward power P_f below 1 mW. The onset of the medium-field Q-slope largely depends on the preparation status of the cavity. A well-cleaned cavity will have less Q-degradation in the medium-field range. The maximum intrinsic quality factor of the 360 MHz CH cavity was found for forward powers in the range of 20 to 150 mW for $\beta \approx 3$.

2.7 Multipacting

Multipacting is a resonant RF process in which electrons repeatedly collide with the cavity surface and multiply via secondary electron emission. The electron avalanche absorbs RF power and hinders the further increase of cavity field levels. This phenomenon can be observed during pulsed operation, where the transmitted power rises and levels off at the multipacting barrier, shown in Figure 2.11.

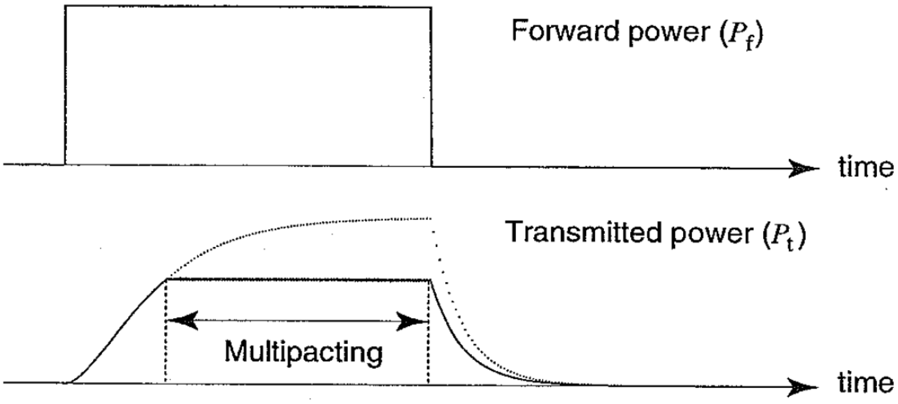

Figure 2.11: The forward power P_f is constant during pulsed operation, where the transmitted power rises exponentially with the time constant 2τ, which is dependent on the intrinsic quality factor Q_0. With the onset of multipacting, the cavity field level is capped at the specific barrier [25].

The multipacting barriers can be processed over time by RF operation at the respective levels. When a conditioned cavity is exposed to air, multipacting barriers often reappear.

The theory is based on the secondary electron coefficient (SEC), which quantifies the average number of new free electrons emitted when one electron collides with the cavity surface. The coefficient δ varies depending on the electron's kinetic energy, as well as the material and preparation conditions.

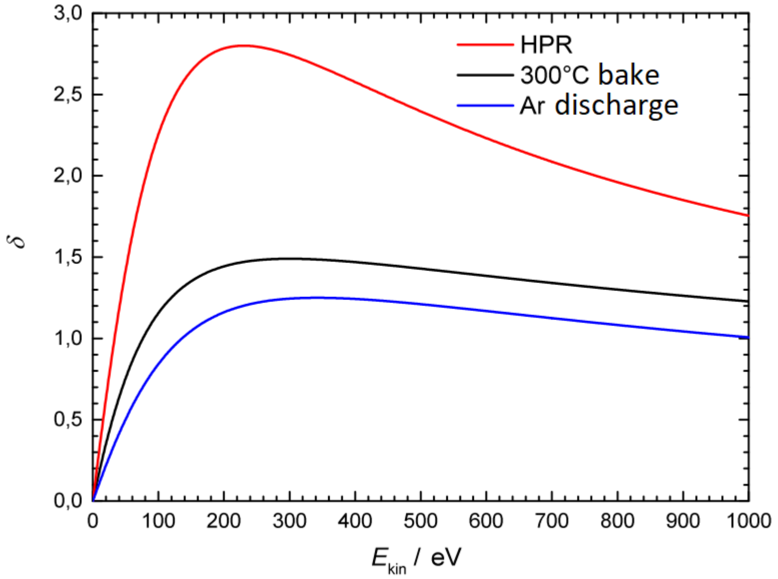

Figure 2.12: The secondary emission coefficient for niobium reaches peak value within 200 – 300 eV of kinetic energy.

The variation in SEC for the same material is attributed to the presence of a few monolayers of adsorbants on the surface, including hydrocarbons and polyethylene lubricants. Desorption, triggered by the impact of electrons, reduces δ over time and explains barrier processing.

At low kinetic energies, the electron interacts with the electrons within the first layers of the material and δ increases proportionally to E_{kin}. As E_{kin} increases, the electron penetrates deeper into the bulk material, producing secondary electrons further below the surface. Consequently, the number of escaping electrons decreases. The multipacing trajectory of the electrons is characterized by the number of resonant impact points (n-point multipacting) and the number of RF periods (multipacting order) the electron experiences before impact.

One-Point Multipacting

For resonant electron multiplication at the same cavity location, certain conditions must be met. The RF phase should remain constant across cycles ($\varphi_1 = \varphi_0$), and the SEC must be greater than 1 for the given impact energy. While surface field $E_\perp$ mainly accelerates the electrons, the magnetic field induces a quasi-cyclotron motion. To satisfy the RF phase boundary condition, the quasi-cyclotron frequency must be an integer multiple of the RF frequency $\omega_{RF} = N \cdot \omega_c$. Multipacting trajectories are typically small compared to the cavity size and therefore well-localized.

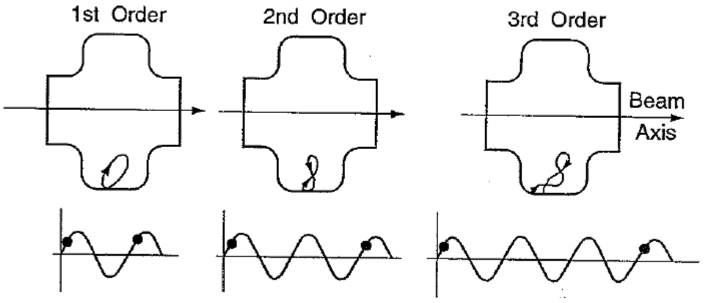

Figure 2.13: One point multipacting trajectories for the orders one to three [25].

The requirement for the possibility of multipacting can approximated by:

$$H_N \propto \frac{m\omega_{RF}}{N\mu_0 e} \tag{2.120}$$

A point of multipacting origin that satisfies the SEC $\delta > 1$ condition can theoretically have up to an infinite number of multipacting barriers, up to a field level proportional to $H_1 \propto \frac{m\omega_{RF}}{\mu_0 e}$. Experiments conducted over the last decades have shown that low beta structures are often confronted with heavier cases of multipacting at lower field levels than high beta elliptical cavities. The frequency dependence in Equation 2.120 contributes to the appearance of barriers at lower field levels. Additionally, low beta structures are more geometrically complex and offer more regions with low electric fields, even at high gradients E_a. Consequently, low beta structures can experience multipacting over a broader range of power. The impact energy is related to the electric field by:

$$E_{kin} = c_2 \frac{e^2 E_\perp^2}{m\omega_{RF}^2} \tag{2.121}$$

Here, $c_2 = 2 \pm 0.08$ is found for quasi-pillbox cavities [25]. The correction factor c_2 accounts for the fact that in quasi-pillbox cavities, the electric field is not purely perpendicular during the electron trajectory. For an energy range from 100 eV up to 1 keV, in the of a 217 MHz cavity, the length of a first-order 1-point orbit is approximately 2.7 – 8.6 cm.

Two-Point Multipacting

The resonance boundary condition between two points is met when $\omega_{RF} = ([2N-1]/2)\omega_c$, where the impact on the opposite point occurs after a phase shift of 180°. This leads to an inverted field distribution that leads back its origin. The simplest analytic case is given by two planar plates with an electric field $E = E_0 \sin(\omega_{RF} t)$, similar to an AC-driven capacitor. The acceleration of an electron within the electric field is given by

$$a(t) = -\frac{eE_0}{m_e}\sin(\omega_{RF} + \varphi_0) \tag{2.122}$$

The time evolution of the electron's position is calculated via double integration in time:

$$x(t) = \frac{eE_0}{\omega_{RF}^2 m_e}[\sin(\omega_{RF} t + \varphi_0) - \sin(\varphi_0)] - \frac{eE_0}{\omega_{RF} m_e} t\cos(\varphi_0) \tag{2.123}$$

Starting with the conditions of an emitted electron at $\varphi_0 = 0$ results in:

$$x(t) = \frac{eE_0}{\omega_{RF}^2 m_e}[\sin(\omega_{RF} t - \omega_{RF} t)] \tag{2.124}$$

The resonance condition requires that electrons collide with the opposite wall after the time period $t_N = \frac{[2N-1]\pi}{\omega_{RF}}$.

$$x\left(\frac{[2N-1]\pi}{\omega_{RF}}\right) = -\frac{(2N-1)\pi e E_0}{\omega_{RF}^2 m_e} = -d \tag{2.125}$$

The associated voltage V_N at which two-point multipacting of order N is possible can be expressed as:

$$V_N = E_0 d = \frac{d^2 \omega_{RF}^2 m_e}{(2N-1)\pi e} \tag{2.126}$$

The upper limit for two-point multipacting ($N = 1$) in a parallel plate arrangement with $d = 2.4\,\mathrm{mm}$ at $f_{RF} = 325\,\mathrm{MHz}$ results in $V_1 = 18.1\,\mathrm{kV}$.

3 Multi-Gap Cavities

3.1 $\beta\lambda/2$ - Structures

In previous chapters, we have seen that modes with electric field components along the beam axis accelerate charged particles. Each mode corresponds to a specific excitation frequency f_r. The electric and magnetic field oscillate at this frequency, defining the acceleration time frame for each gap as $\frac{1}{2f}$. When a particle is accelerated, it attains an average velocity $\overline{v}$ within the acceleration zone, located between the pre and post-acceleration velocity spans. The velocity $\overline{v}$ enables us to calculate the associated length of the acceleration cell, where the electromagnetic fields have not yet reversed their directions. The length is determined by

$$L = \frac{\overline{v}}{2f_r} \tag{3.1}$$

To express Equation 3.1 in terms of β, the relativistic velocity is defined as:

$$v = \beta c \tag{3.2}$$

Additionally, the relation between frequency f, wavelength λ and the speed of light is required:

$$c = f \cdot \lambda \tag{3.3}$$

Combining Equation 3.2 and Equation 3.3, we can rewrite Equation 3.1 as:

$$L = \frac{\beta\lambda}{2} \tag{3.4}$$

A compact accelerator design allows for the inclusion of multiple acceleration cells within a resonator. This is achieved by inserting drift cells that shield the particle during the time of reversed electromagnetic field. This concept forms the fundamental principle behind modern DTL structures, as in the case of the CH structure.

3.1.1 CH Structure

The CH structure is based on the pillbox and adheres to the design criteria of the $\beta\lambda/2$ design. Figure 2.1 demonstrates that the fundamental H_{211} mode within a pillbox arrangement is incapable of particle acceleration. There is no electric field component along the beam axis, making particle acceleration impossible.

In DTLs, electric fields along the beam axis are generated by the opposite charge of adjacent drift tubes. The periodic alignment of these stems takes advantage of the magnetic field distribution, inducing periodically inverted stem currents and creating the desired charge distribution within the drift tubes. The z-component of the magnetic field respects the boundary conditions of the tank, similar to the pillbox case from

Equation 2.34. This magnetic field follows a distribution in which the resulting electric field is at its maximum at the center and decreases toward the lids, as illustrated in Figure 3.1.

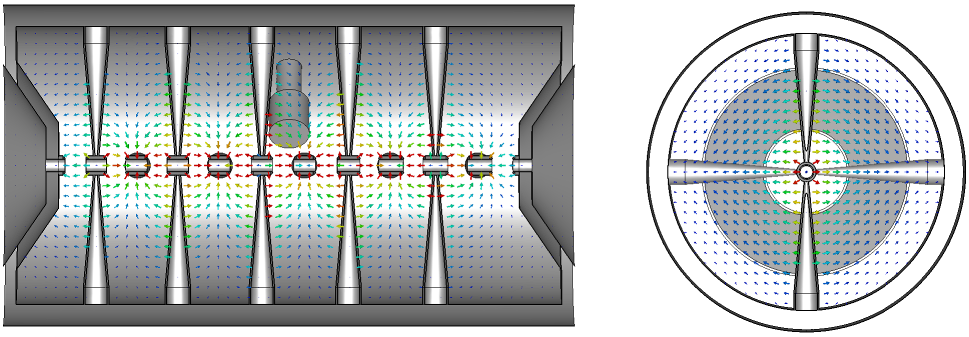

Figure 3.1: The insertion of stems and drift tubes into a pillbox resonator rearranges the electromagnetic field distribution of the TE_{211} mode previously displayed in Figure 2.1. The electric field of the TE_{211} mode is shown in the longitudinal and transverse plane, simulated with CST [23].

The inclusion of stems and drift tubes into the pillbox introduces significant changes in the total inductance and capacitance, redistributing the electric and magnetic fields. This redistribution results in a change in the stored electric and magnetic field energy within the resonator. An unsymmetric reduction in electric and magnetic field energy leads to a frequency shift in the excited resonator mode, which is also the fundamental principle behind tuners.

The insertion of drift tubes introduces an electric field component along the beam axis and increases the total capacitance of the resonator, thereby reducing the resonance frequency. In the case of the MYRRHA cavities, the frequency was reduced by 30% compared to a pillbox of an equal radius. Since cavity dimensions are inversely proportional to the frequency, this results in reasonably sized accelerators with reduced transverse dimensions at lower frequencies.

Returning to the case of superconducting CH cavities, a significant advantage of such a setup is mechanical stiffness and support. Superconducting DTLs are constructed from niobium sheets with a wall thickness of approximately 3 mm. This, combined with the decreased stiffness of niobium at low temperatures, makes superconducting cavities susceptible to mechanical vibration modes, referred to as microphonics. When a mechanical vibration mode is in close proximity to the RF resonance frequency, it can excite the mechanical mode, affecting the RF resonance frequency. Given the narrow frequency band due to the high-quality factor, this can render a cavity inoperable.

3.1.2 Elliptical Structure

The majority of SC cavities are elliptical cavities due to their efficiency in the medium to high β range of 0.5 to 1. Since electrons reach velocities above $\beta = 0.5$ for energies above $E_{kin} = 511\,\text{keV}$, electron accelerators are heavily reliant on this structure. High-energy sections for protons and light ions are also reliant on SC elliptical cavities, as shown in Chapter 2.3. The RF operation mode is TM_{010}, similar to the TM_{010} mode of a pillbox shown in Figure 2.1. The design of an acceleration cell is primarily dependent on two ellipses, shown in Figure 3.2:

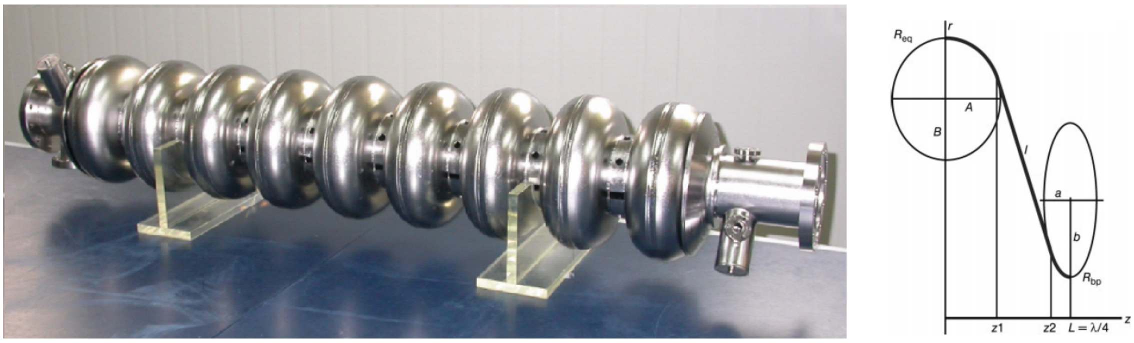

Figure 3.2: A prominent design of an elliptical cavity is the "tesla" structure, a 1.3 GHz 9-cell solution that is operated in the TM_{010} pi-mode [29]. The design parameters of half an acceleration cell is shown on the right [30].

The electric field of the mode is concentrated towards the cavity center and the magnetic field peaks in the elliptical outer cavity volume. Optimization of magnetic peak fields is achieved by adjusting ellipsoid parameters A and B, while electric peak fields respond to a and b. Additionally, the tilt of the resonator wall with length l increases stiffness and mechanical stability. There are different cell profile perturbations used to optimize the cavities for specific operations, such as the re-entrant and the low-loss shapes. Both of these shapes follow the same concept of minimizing H_p by increasing the surface area and, in the case of the low-loss cavities, also reducing the aperture. This results in RF loss savings of up to 23% to 34%, but there is a trade-off as the decreased aperture (from 70 mm to 60 mm) leads to increased longitudinal wakefields (by 18%) and transverse wakefields (by 65%). To mitigate this, precise cavity alignment is required to maintain beam emittance throughout the accelerator. For more detailed information on these optimized cavity projects, interested readers can refer to the references [31, 32, 33, 34, 35].

3.2 Comparison of SC CH Structure Performances

Existing CH cavities demonstrated mixed origins for field limitation in the past. The first CH prototype was limited by field emission, reaching $E_a = 7\,\mathrm{MV/m}$ [24]. A 325 MHz cavity showed low amounts of field emission and quenched due to magnetic heating [36]. CH0 of HELIAC showed moderate field emission and has quenched due to a combination of field emission and magnetic heating at $E_a = 9.6\,\mathrm{MV/m}$ [37].
Further preparations of this work were performed on the 360 MHz cavity and resolved the field emission limitation previously observed. The cavity showed similar performance behavior and limitation sources to CH0. The Q-E performance plots of all cavities show two different Q-slope responses, see figure 3.3.

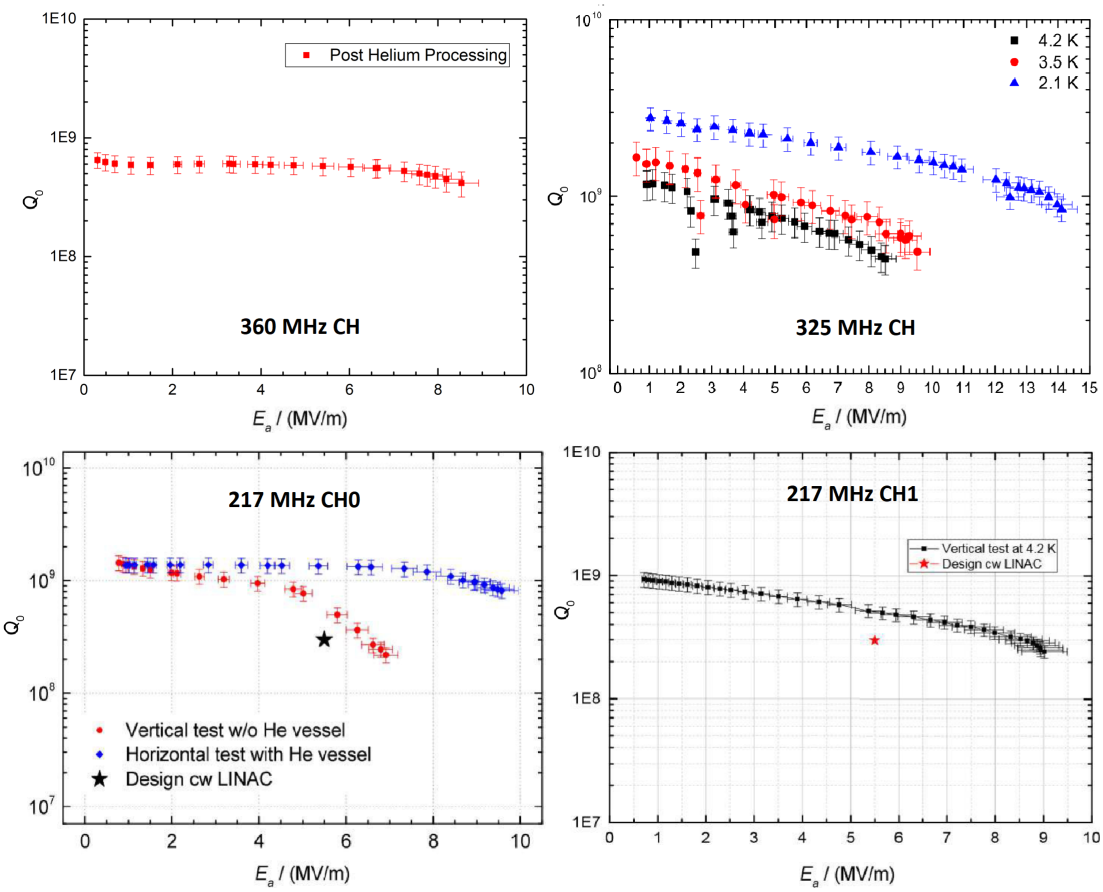

Figure 3.3: The Q-E performance plots of all CH cavities tested at 4 K, including a 2 K test for the 325 MHz CH. Two distinct Q-slopes are observed, where the left cavities show almost no Q degradation at all and the right cavities show an approximately linear decrease within the logarithmic plot [24, 37, 36, 38].

Considering the RF parameter listed in Figure 3.1, the cavities with weaker Q-slope have substantially higher R_a/Q_0 and lower magnetic peak field ratio B_p/E_a. The BCS thermal feedback model identifies the interaction between magnetic heating and BCS temperature dependence as the origin of the medium Q-slope. In this model, the Q-slope stems from the increased ohmic losses. The medium Q-slope is defined in the range of 40 to 100 mT. The quasi-constant Q-slope is observed for magnetic peak fields far below the threshold of the model. The onset of the Q-slope for the cavities without a semi-constant slope happens at field levels of $E_a > 6\,\mathrm{MV/m}$ and coincides with the onset of field emission. Since the magnetic field gradients below $E_a < 3\,\mathrm{MV/m}$ are below the magnetic threshold for the BCS thermal feedback model, it is unlikely to be the source of the Q decline. Furthermore, the overall geometric properties of all cavities are very similar. Important RF parameters of the cavities are shown in Table 3.1. For increasing magnetic peak fields, the magnetic heating losses should therefore lead to similar Q-slope behavior. With an onset at 1 MV/m the quasi-constant cavities should experience similar magnetic heating starting at 2 MV/m, which is not the case.

RF parameter	**360 MHz CH**	**325 MHz CH**	**217 MHz CH0**	**217 MHz CH1**
f/MHz	360	325	217	217
β	0.1	0.16	0.059	0.069
E_a/(MV/m)	8.7	8.5	9.6	9
E_p/E_a	5.6	5	6.3	6
B_p/E_a	5.7	13	5.7	<10
G/Ω	56	66	52	50
R_a/Q_0	3180	1260	3240	1070
E_p/(MV/m)	48.2	42.5	60.48	54
B_p/mT	49.6	110.5	54.7	90

Table 3.1: RF parameter overview of all SC CH cavities, including their measured maximum electric field [24, 36, 37, 38].

The Q-slope of the constantly declining cavities is quasi-linear for gradients below $E_a < 6\,\mathrm{MV/m}$ and further increases with the onset of additional field emission losses. Within the emission-free range, a linear Q-slope is caused by exponential losses. Measurements of the 325 MHz CH structure revealed the presence of multipacting over the entire field-level spectrum. Figure 3.3 shows distinct 'harder' barriers between 2 MV/m up to 12.5 MV/m and the underlying constant Q-slope. 217 MHz CH1 shows no barriers but a similar Q-slope. While the 325 MHz CH cavity has girders, the 217 MHz cavity has none. The most prominent difference lies in the tuner. Since the 360 MHz CH prototype was solely developed to prove the feasibility and efficiency of SC CH structures and therefore has no tuner. The 217 MHz CH0 has a tuner design that differs from the two remaining cavities. Figure 3.4 illustrates the difference in two main lamella parameters: gap distance and gap depth.

The design of the CH0 tuner lamella has a bigger gap distance and fewer gap depth, while simultaneously having a bigger lamella edge radius.

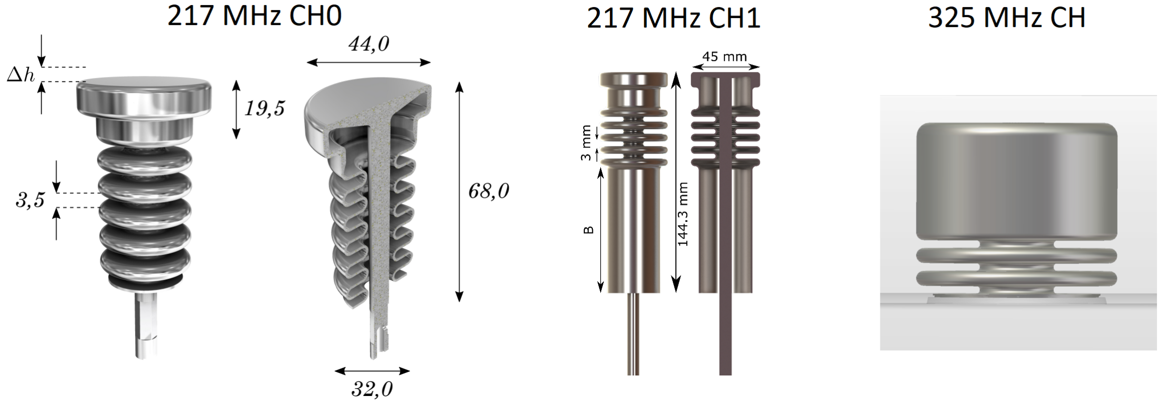

Figure 3.4: Comparison of the used tuners, a major difference is given in the gap distance of the 217 MHz CH0 which is significantly bigger with 3.5 mm compared to 2.4 and 2.6 mm of the other two tuners. Gap depth is also shorter with 9.25 mm compared to 14.7 and 25 mm [36, 37, 38].

These tuners can be tested by a cold test series with the 360 MHz cavity. If the cavity shows changed Q-slope behavior after installment, a new tuner design similar to CH0 could yield reduced RF losses. The performance curve of CH0 has shown, that a semi-constant quality factor over several MV/m can be achieved by CH structures. If CH1 had a semi-constant quality factor up to 6 MV/m, the RF losses difference would be:

$$\Delta P_{\mathrm{c}} = \frac{U_a^2}{\left(\frac{R_a}{Q_0}\right)}\left(\frac{1}{Q_0} - \frac{1}{Q_0}\right) = \frac{(6\,\mathrm{MV/m}\cdot 0.382\,\mathrm{m})^2}{1070\,\mathrm{M\Omega}}\left(\frac{1}{5\cdot 10^8} - \frac{1}{9\cdot 10^8}\right) = 4.36\,\mathrm{W}$$

The RF losses at 6 MV/m of CH1 are 9.82 W and investigation into the origin of the two different Q-slope behaviors could safe RF losses in the range of the projected loss difference in CH1 of 43.8 %.

4 CST Microwave Studio

CST Microwave Studio is a development environment used for the numerical calculation of various electromagnetic field problems, with each problem being addressed by a specific solver. RF resonator field distributions are calculated by the so-called 'eigenmode' solver, which operates in the frequency domain. Since cavity modes are oscillating field distributions, the solution is proportional to $e^{i\omega_\mathrm{r}t}$. The differential Maxwell wave Equations 2.5, 2.6 in its original form have to be solved:

$$\nabla \times \nabla \times \mathbf{E} = -\frac{1}{c^2}\frac{\partial^2 E}{\partial t^2} \tag{4.1}$$

$$\nabla \times \nabla \times \mathbf{H} = -\frac{1}{c^2}\frac{\partial^2 H}{\partial t^2} \tag{4.2}$$

To simulate these fields, CST Studio Suite uses the Finite Integration Method (FIT). The cavity is divided into a finite amount of tetrahedral volumes, and the local solutions to the wave equations are computed for each cell. The metallic surfaces along the volume elements represent the geometric boundary conditions of the resonator. Increasing the number of cells results in higher mesh density, and the average volume height and mesh density can be adjusted via a mesh variable in the eigenmode solver. Greater mesh density provides a more accurate representation of the geometry, improving the accuracy of the global solution.

The global solution has to satisfy all boundary conditions of each adjacent volume edge. With increasing volume number N the calculation effort grows as N^3. The simulation error reaches a minimum with decreasing volume size but then starts to increase due to rounding errors, that are fixed at an absolute value and become increasingly significant. Below a certain volume size, which is dependent on the mesh parameter h, the relative rounding error increases considerably, as depicted in Figure 4.1.

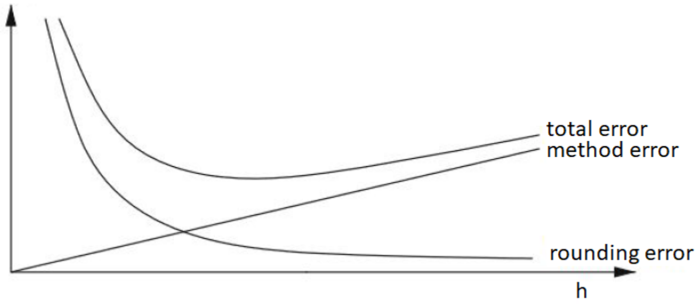

Figure 4.1: The total relative error is given by the sum of the relative method error that decreases with mesh number and relative error from rounding that increases with mesh number, modified [39].

CST normalizes the field solution for a total field energy of $W = 1\,\mathrm{J}$. Important RF parameters, that are introduced in chapter 2.2, can be calculated in the post-processing section. The simulations are performed with Perfect Electric Conductor (PEC) boundary conditions, which is an imaginary material with infinite conductivity. This has the effect, that the electromagnetic fields can not penetrate the surface, and the eigenvalue k_{mnp} of a calculated mode TE_{mnp} or TM_{mnp} is a real number. A complex part of an eigenvalue would lead to an exponentially decreasing term as part of the solution:

$$\exp(i\omega_{mnp}t) = \exp(ik_{mnp}ct) = \exp(i\,\mathrm{Re}\{k_{mnp}\}ct) \cdot \exp(-\,\mathrm{Im}\{k_{mnp}\}ct) \tag{4.3}$$

The inner surfaces of normal conducting resonators are typically from materials with high conductivity such as copper, where the field penetration depth δ is small and PEC represents an appropriate choice for the simulation.

CST simulations of the 360 MHz CH cavity were used to identify all inner cavity surfaces that could enable field emission onset. Surface field levels were simulated and analyzed for expected gradients above $E_a = 7\,\mathrm{MV/m}$ and led to the design of two different HPR nozzles, see Chapter 6.1.2.

5 Superconductivity

Superconductivity is a phase of matter in which electrical resistance vanishes completely when the material is cooled below a certain critical temperature. This discovery dates back to 1911 when Heike Kamerlingh Onnes observed an abrupt drop in resistance in mercury when it was cooled to around 4.2 K. One of the early observations in the study of superconductors was that the critical temperature (T_c) is dependent on the mass of the superconducting isotope. Specifically, it was found that T_c is inversely proportional to the square root of the mass ($T_c \propto \frac{1}{\sqrt{m}}$). This relationship suggested that superconductivity is a result of an interaction between electrons and the crystal lattice of the material.

The BCS[4] theory, named after Bardeen, Cooper, and Schrieffer, provides a microscopic model for understanding superconductivity. It is a quantum mechanical theory that explains how, at temperatures below T_c, electrons form pairs called Cooper pairs and condense into a single quantum state. These paired electrons are responsible for the zero electrical resistance observed in superconductors.

Another important theoretical framework for superconductivity is the Ginzburg-Landau theory. This theory takes a thermodynamic approach to the behavior of superconductors and provides macroscopic parameters that describe their properties. It describes the transition from the normal state to the superconducting state, known as the superconducting phase transition, and provides insights into the behavior of superconducting materials under the influence of magnetic fields. Both the BCS theory and the Ginzburg-Landau theory have been instrumental in explaining the properties and limits of superconductors, including their applications in particle accelerators and other technological devices. These theories have enabled the development of advanced superconducting materials that can operate at higher temperatures and magnetic fields, making them essential for modern particle accelerator technologies.

---

[4] Introduced in 1957

5.1 BCS Theory

The BCS theory describes superconductivity by explaining microscopic interactions between electrons with electrons in a crystal lattice. This new interaction allows for an attractive potential between electrons and the formation of Cooper pairs. The process begins with one electron-inducing lattice polarization in its vicinity by attracting the positively charged lattice ions. This displaces the ions from their point of origin, distorting the lattice. The locally increased positive charge density results in an attractive force that another electron experiences, shown in Figure 5.1.

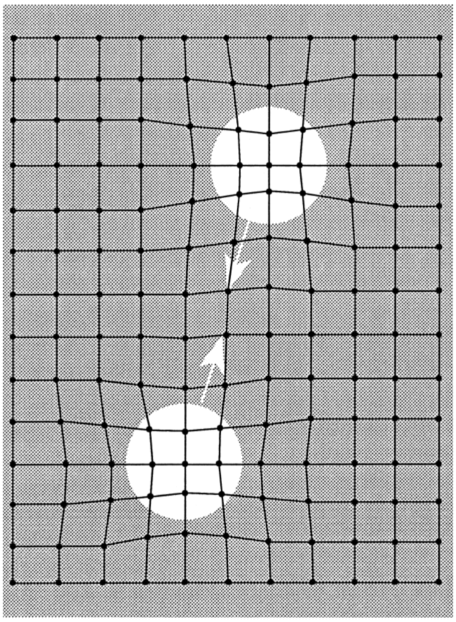

Figure 5.1: Polarization of the lattice attracts another electron [40].

The kinetic electron energy is typically in the range of a few eV. The corresponding electron velocities are very fast, with some percent of the speed of light. The response of the ions is limited by inertia due to their comparatively large mass. Therefore, the electrons leave a polarization trail in the lattice, in which another electron can lower its energy. If the orientation of the second electron momentum and its spin is anti-parallel to the first electrons, the attractive potential is large enough to overcome coulomb repulsion at a certain distance and allows for the formation of a Cooper pair $(-e, \vec{p}, \vec{s}; -e, -\vec{p}, -\vec{s})$. A lighter isotope has a quicker response time which results in a higher frequency of the lattice response and an increase of the attraction. Lattice frequencies can be described by harmonic wave functions with a well-defined wavelength. With equation $p = \frac{h}{\lambda}$ a momentum can be assigned to the lattice vibrations, and therefore represent particles referred to as phonons. Phonons are virtual particles that exclusively exist during the short correlation time of the electron-electron-lattice interaction, illustrated in Figure

5.2. Since cooper pairs only exist during the exchange of phonons, the condensation and breaking of cooper pairs is a dynamic process inside a superconductor. The coherence length ξ_0 represents the average distance of the cooper pair electrons and ranges from 100 to 1000 nm.

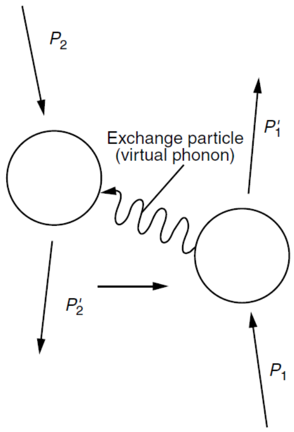

Figure 5.2: Feynmandiagram of electron-electron-phonon interaction [40].

The abrupt jump in resistance of a superconductor at the critical temperature T_C sets in because the forming cooper pairs have a total spin of 0 and do not follow the Fermi-Dirac statistic of fermions. Cooper pairs are bosons whose underlying statistics are fundamentally different because the Pauli exclusion principle does not apply. All cooper pairs are allowed to occupy the same energy ground state, forming a Bose-Einstein condensate. Since Cooper pairs do not transition between different states, no energy dissipation takes place and supercurrents remain collision-free.

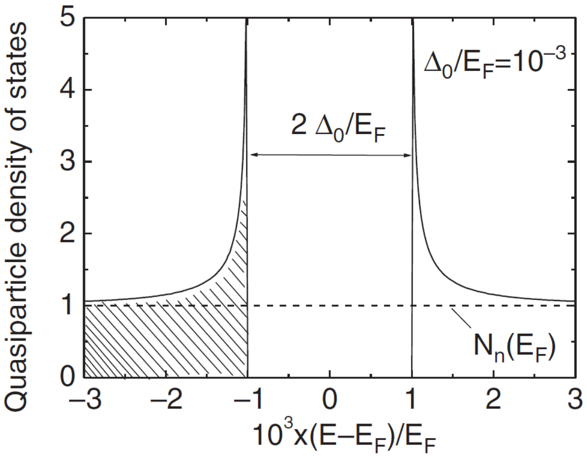

Figure 5.3: Density of states for quasiparticles [40].

When cooper pairs are excited above the ground state, they break into two unpaired electrons. These quasiparticles show a density of states distribution $N_S(E)$, which vanishes in the energy range of $E_F \pm \Delta_0$. For $|E - E_F| \geq \Delta_0$ reaches infinity for $E = E_F + \Delta_0$ and convergences towards the density of state distribution of non-interacting electrons, see Figure 5.3. The density of cooper pairs n_S is proportional to Δ_0^2 and increases with decreasing temperature. $2\Delta_0$ is the energy gap of the superconductor. The BCS theory finds the important relation between the energy gap and the critical temperature: $2\Delta_0(T = 0) = 3.5 k_B T_C$

5.2 Meißner-Ochsenfeld Effect and Characteristic Lengths

Fritz Walther Meißner and Robert Ochsenfeld demonstrated in 1933 that superconductors expel external magnetic fields when transitioning from the normal state into the superconducting state. Above the critical temperature T_C, the superconductor's volume is penetrated by the external magnetic field. When lowered below the critical temperature, the supercurrents compensate for the external magnetic field, resulting in $(B = 0)$, see Figure 5.4. This effect does not stem from Faraday's law 2.2 but from the onset of superdiamagnetism, where $\chi = -1$.

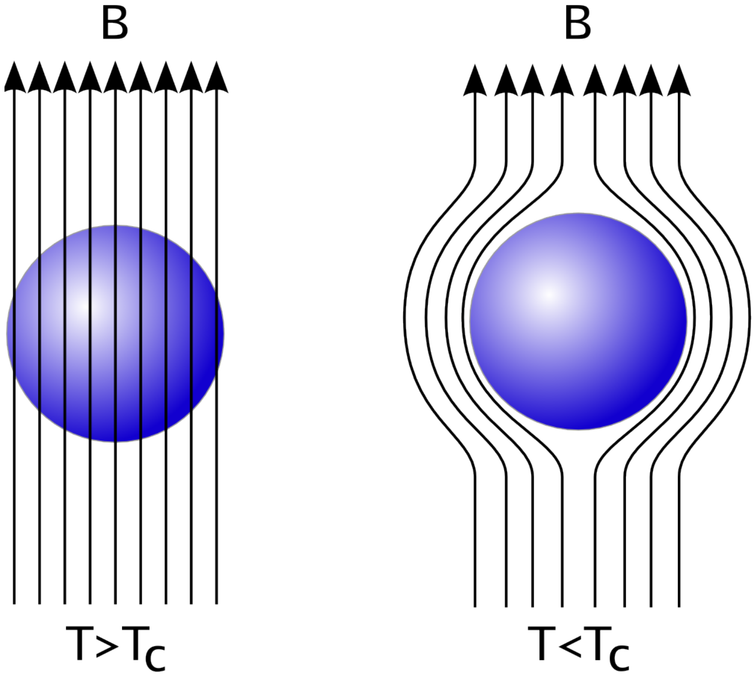

Figure 5.4: Meißner-Ochsenfeld shown where an external magnetic field is expelled from the superconductors volume [41].

This effect provided experimental validation that superconductivity represents a phase transition into a new state of matter. The external magnetic field is not completely ex-

pelled from the interior of the superconductor; it penetrates the surface and decays exponentially $B(x) = B_0 e^{-\frac{x}{\lambda_L}}$. Here, $\lambda_L = \sqrt{\frac{m}{\mu_0 q^2 n_s}}$ is the London penetration depth.
In Chapter 5.1, the BCS coherence length ξ_0 of Cooper pairs was introduced as the average distance of the paired electrons. The Ginzburg-Landau theory defines an additional coherence length $\xi_{GL} = \xi_0 \frac{\lambda_L(T,l^*)}{\lambda_L(T=0,l^* \to \infty)}$, with l^* being the free mean path of the electrons. ξ_{GL} is the smallest length in which cooper pair density can vary and is always larger than ξ_0. Consequently, the Cooper pair density cannot vary within distances smaller than the Cooper pairs themselves. The ratio $\kappa = \frac{\lambda_L}{\xi_{GL}}$ is known as the "Ginzburg-Landau parameter" and is independent of temperature and magnetic field but strongly depends on l^*.
In Section 5.4 we will see how κ can classify materials as type I or type II superconductors.

5.3 Type I Superconductors

In Chapter 5.2, we observed that superconductors expel external magnetic fields, referred to as the Meißner phase, which depends on temperature and applied magnetic fields. For a rod-shaped sample, the magnetic field is constant, except at the ends where the field is diverted.

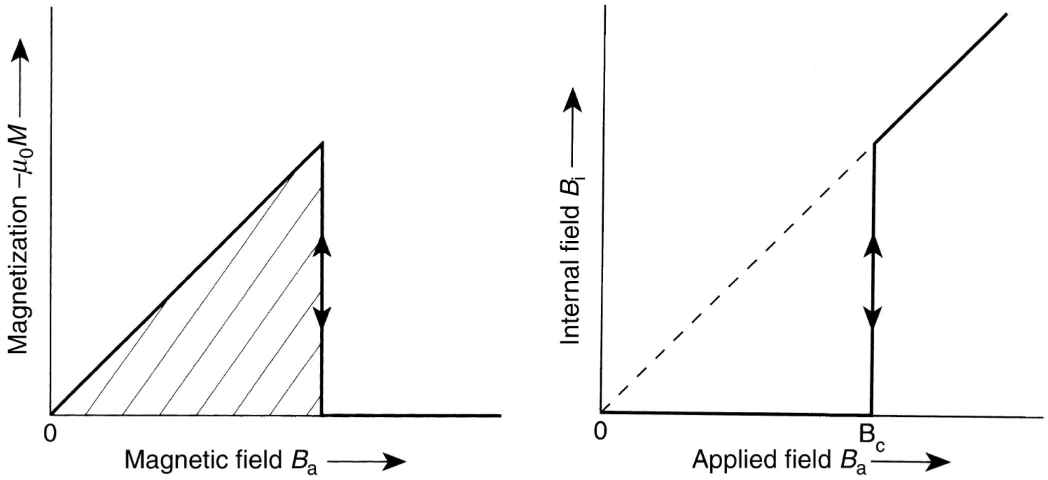

Figure 5.5: Magnetization of a type I superconductor [40]

The magnetization M increases linearly with the external magnetic field. The external magnetic field is compensated up to a critical value referred to as the critical field B_C. When B_C is exceeded, the superconducting state becomes unstable and the Meißner state vanishes, resulting in a jump in the internal magnetic field as the shielding supercurrent collapses, as shown in Figure 5.5. The temperature dependence is approximated by the empirical equation:

$$B_C(T) = B_C(0)\left[1 - \left(\frac{T}{T_C}\right)^2\right] \tag{5.1}$$

Equation 5.1 shows that the critical magnetic field increases as the temperature decreases. In section 5.6 the importance of magnetic shielding for cavity performance will be discussed.

5.4 Type II Superconductors

The penetration depth λ_L and coherence length ξ_{GL} are properties of the lattice material. In cases where $\lambda_L > \xi_{GL}$, the penetration of magnetic fields into the superconductor can become energetically favorable. λ_L increases slightly with the mean free path l^* of electrons, while ξ_{GL} decreases with $(l^*)^{\frac{1}{2}}$. For materials with $\kappa > \frac{1}{\sqrt{2}}$, two superconducting phases exist: the Meißner and Shubnikov phases. Below a critical field B_{C1}, the superconductor is in the Meißner phase and completely expels external magnetic fields. For $B_{C1} < B < B_{C2}$, the magnetic field penetrates the superconductor and magnetization decreases monotonically with increasing B in the Shubnikov phase, see Figure 5.6.

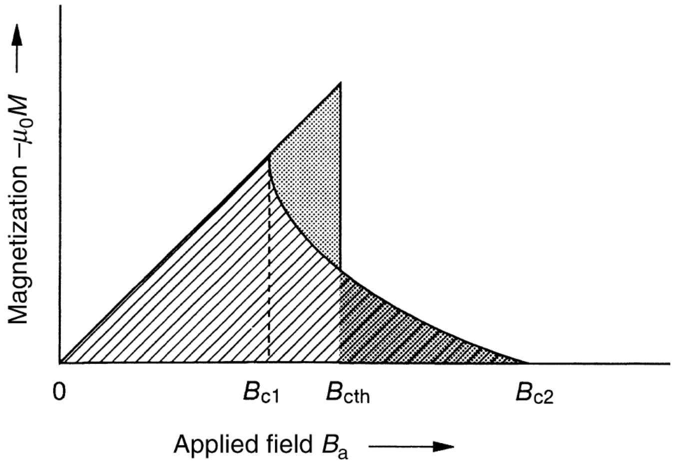

Figure 5.6: Magnetization of a type II superconductor [40]

The magnetic field penetrates the superconductor in the form of quantized flux lines known as vortices. Each vortex has the value $\Phi_0 = \frac{h}{2e} = 2 \cdot 10^{-15}\,\mathrm{Vs}$ and is surrounded by circular surface supercurrents that vanish towards its center, see Figure 5.7.

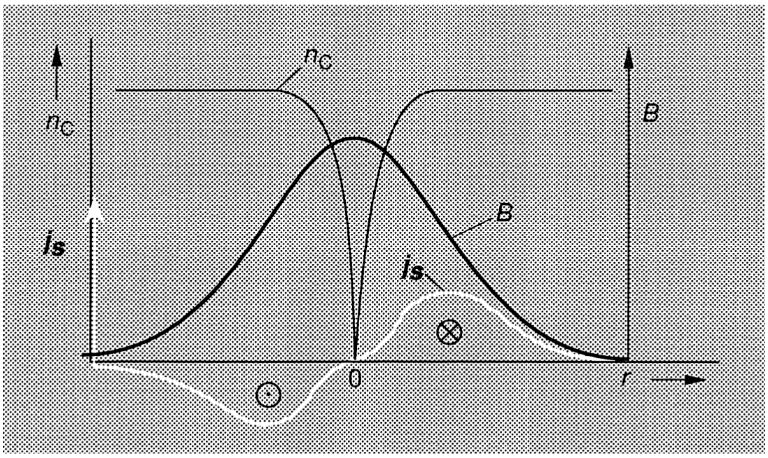

Figure 5.7: Magnetic field and cooper pair density distribution inside a vortex [40]

The radial decrease of the magnetic field depends on the penetration depth λ_L. The vortices are aligned in a triangular lattice, with one flux quantum at each lattice site. The lattice vortex density increases with increasing external magnetic field. For field levels slightly below B_{C2}, the vortex distance reduces to about $2\xi_{GL}$, and the circular supercurrents overlap strongly. Towards B_{C2}, the cooper pair density continuously approaches zero. Type II superconductors have critical magnetic fields that greatly exceed those of type I superconductors. An important example of a type II superconductor is niobium with a critical temperature of 9.2 K, which is the highest of all metals. Niobium has a high critical magnetic field of $B_{C2} = 240\,\mathrm{mT}$ and good material properties for manufacturing particle accelerators. The purity of niobium is quantified by the fraction of normal conducting resistance at room temperature and at 4 Kelvin: $RRR = \frac{R_{300K}}{R_{4K}}$. Superconducting cavities are typically built from niobium with $RRR > 300$.

5.5 Superconducting Cavities

Superconducting cavities are employed in applications that require high voltages, high-duty cycles, and short acceleration lengths. For these demands, RF losses of NC cavities are the dominant cost and can exceed 30 $\frac{\mathrm{kW}}{\mathrm{m}}$, requiring sophisticated cavity cooling systems. For RF superconductivity the resistance of the resonators does not completely vanish. Still, the losses are several magnitudes smaller, with losses in the range of a few $\frac{\mathrm{W}}{\mathrm{m}}$. During operation, helium must be continuously processed by a helium liquefier. The cooling machine's efficiency can be roughly approximated by the second law of thermodynamics using the Carnot process.

$$\eta_C = \frac{T_{cold}}{T_{warm} - T_{cold}} \tag{5.2}$$

When considering a starting temperature of 300 K, Equation 5.2 yields the theoretical upper limit efficiencies

- 0.014 for 4.2 K
- 0.006 for 1.8 K

The temperatures 4.2 K and 1.8 K are common operating temperatures for SC cavities. The actual power demands per 1 W of cryo power at 4.2 K requires 250 W and it's 1000 W at 1.8 K. For cavity losses of 20 W at 4.2 K the power required amounts to 5 kW. This is a significant improvement compared to typical normal conducting losses, which can go up to 100 kW.

The electromagnetic field inside the cavity is accompanied by surface currents that flow within a thin layer of depth δ. The surface resistance is defined as:

$$R_S = \frac{1}{\delta\sigma} \tag{5.3}$$

Here, σ represents the conductivity of the cavity material. The surface currents of SC RF cavities consist of both Cooper pairs and normal conducting electrons:

$$J = J_N + J_S \tag{5.4}$$

The normal current J_N is given by Ohm's law:

$$J_N = \sigma_N E_0 \mathrm{e}^{i\omega t} \tag{5.5}$$

The conductivity of the electrons is given by Drude's law:

$$\sigma_N = \frac{e^2 \tau n_n}{m_e} = \frac{n_n e^2 l}{m_e v_F} \tag{5.6}$$

τ is the mean time of flight of electrons, n_n is the density of electrons, l is the mean free path length, and v_F is the Fermi velocity. The RF surface supercurrents are periodic:

$$J_S = J_{S,0}\mathrm{e}^{i\omega t} \tag{5.7}$$

London's first law states that:

$$\frac{\partial J_S}{\partial t} = \frac{1}{\mu_0 \lambda_L^2} E \tag{5.8}$$

Inserting Equation 5.7 into Equation 5.8 yields:

$$J_S = \frac{-i}{\omega \mu_0 \lambda_L^2} E = -i\sigma_S E \tag{5.9}$$

$$\sigma_S = \frac{1}{\omega \mu_0 \lambda_L^2} = \frac{n_S e^2}{m_e \omega} \tag{5.10}$$

The surface resistance is the real part of the complex term:

$$R_S = \mathrm{Re}\left\{\frac{1}{\lambda_L \sigma}\right\} = \mathrm{Re}\left\{\frac{1}{\lambda_L(\sigma_N - i\sigma_S)}\right\} = \frac{1}{\lambda_L} \cdot \frac{\sigma_N}{\sigma_N^2 + \sigma_S^2} \tag{5.11}$$

The conductivity of Cooper pairs is significantly larger than that to electrons ($\sigma_N \ll \sigma_S$):

$$R_S \approx \frac{\sigma_n}{\lambda_L \sigma_s^2} \tag{5.12}$$

The surface resistance is proportional to the conductivity of the normal conducting electrons. The associated current is carried by the quasiparticles, that are generated from cooper pair breaking. The superconductor has an energy gap $E_g = 2\Delta(T)$. Figure 5.3 shows that electrons occupy the states inside the gap. In analogy to semiconductors, the conductivity σ_n can be calculated:

$$\sigma_n \propto l\mathrm{e}^{-\frac{E_g}{2k_B T}} = l\mathrm{e}^{-\frac{\Delta(T)}{k_B T}} \tag{5.13}$$

Inserting equations (5.13) and (5.10) into (5.12):

$$R_S \propto \mu_0^2 \lambda_L^3 \omega^2 l \cdot \mathrm{e}^{\frac{-\Delta(T)}{k_B T}} \tag{5.14}$$

The surface resistance for RF supercurrents increases exponentially with temperature and square with frequency. The BCS resistance of niobium is approximately given by:

$$R_{S,BCS} = 9 \cdot 10^{-5} \frac{f^2}{T} \mathrm{e}^{-\frac{17.67}{T}} \tag{5.15}$$

with the frequency in GHz and the Temperature in K.

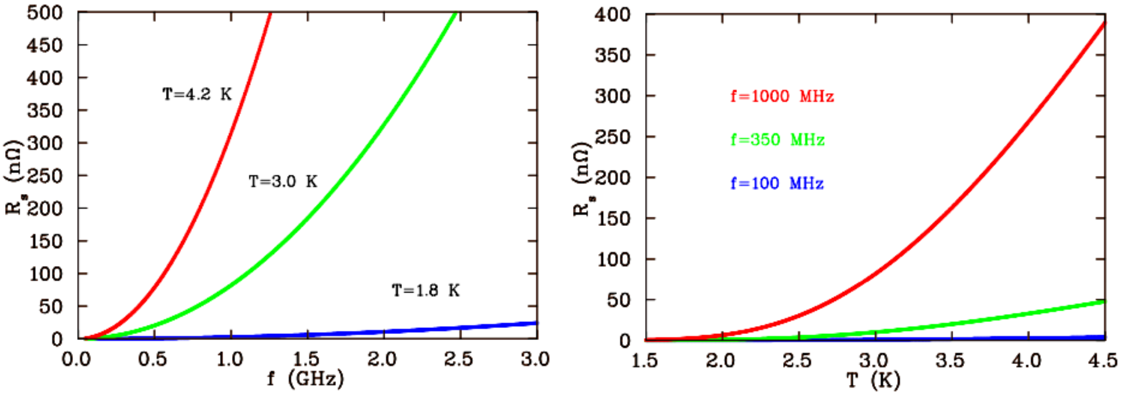

Figure 5.8: The BCS resistance of sc cavities increases quadratically with f. 4.2 K or 2 K are typical operating temperatures of sc accelerators. The BCS resistance of sc cavities increases exponentially with T. The frequency dependence is shown for low, common CH cavity frequencies and high frequencies that are typical for elliptical cavities [24].

The frequency-dependent BCS resistance increase is larger at 4 K than at 2 K, and demands higher cooling power of the cryo system for higher frequencies. Depending on the operation frequency and duty cycle of the accelerator, a decrease in helium temperature can become more economical. This is achieved by pumping 4.2 K helium from norm pressure to lower pressures. The temperature shift to 2 K becomes feasible above 700 MHz. The total resistance of a superconductor is given by the BCS resistance and an additional term, called residual resistance R_0.

$$R_S = R_0 + R_{S,BCS} \tag{5.16}$$

The residual resistance is typically in the range of tens of nΩ and increases with trapped magnetic flux, lattice impurities, and defects that diminish the work function ϕ. These factors will be discussed in the next Chapter 5.6.

5.6 Limiting Effects of SC Cavities

Cavity performance is assessed based on two main RF parameters: Q_0 and E_a. The quality factor Q_0 is inversely proportional to losses. At low field levels, the losses are primarily due to RF losses, which depend on the surface resistance. However, as the gradient increases, additional effects set in, further reducing the quality factor. Eventually, the breakdown of the superconducting state occurs at a certain gradient value, which is below the limit that the BCS theory predicts. Chapter 6 will introduce preparation methods that have been shown to address the following effects.

5.6.1 Residual Resistance

The performance of SC cavities is lower than the BCS theory predicts. The BCS resistance equation 5.15 leads to higher Q_0 values than observed for a given temperature and frequency. In case of the 360 MHz CH cavity, the theoretical value for Q_0 is given by:

$$Q_{0,BCS} = \frac{G}{R(f = 0.36\,\mathrm{GHz}, T = 4.2\,\mathrm{K})_{s,BCS}} = \frac{56\,\Omega}{41.34\,\mathrm{n}\Omega} = 1.35 \times 10^9$$

The measured quality factor was consistently close to 6.5×10^8 at low field levels after HPR treatment. Therefore, the total surface resistance at low levels amounts to

$$R_s = \frac{G}{Q_0} = 86.15\,\mathrm{n}\Omega$$

The difference of $44.81\,\mathrm{n}\Omega$ is attributed to two resistances related to trapped external magnetic fields and the forming of hydrides during cooldown from room temperature.

Hydrides

One well-understood loss mechanism of SC cavities arises from the formation of normal conducting hydrides during cooldown, referred to as Q-disease. The extent of the hydride formation depends on the amount of dissolved hydrogen present and the time required to overcome the critical temperature band of $60 - 150\,\mathrm{K}$, where hydride formation occurs. One of the main hydrogen contamination sources is chemical etching. The diffusion rate heavily depends on acid temperature and is sufficiently low below 15° C [30]. The risk of Q-disease is present for hydrogen concentrations above 2 ppm, and it becomes almost certain for concentrations above 10 ppm. Degassing of chemically etched cavities has become the standard, where the cavity is heated to 600° C to 800° C under UHV. The standard for SC cavities is the 'fast' cooldown, which is defined by the time required to pass the critical temperature band within 1 h. CH cavities are chemically etched using Buffered Chemical Polishing (BCP) with an appropriate bake-out protocol. The effect of slow and fast cooldown for a 325 MHz CH cavity is shown in Figure 5.9.

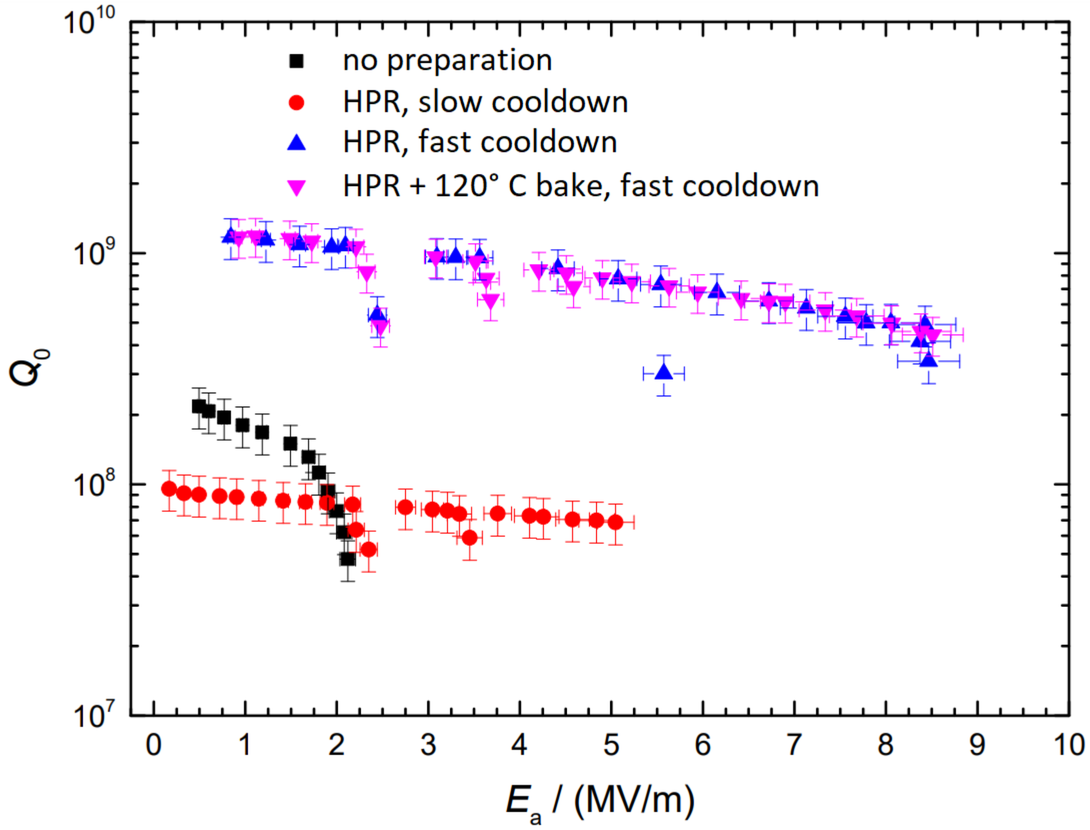

Figure 5.9: The difference between slow (24 h, red) and faster (2 h, blue, purple) cooldown is shown. Forming of hydrides leads to a decrease of one magnitude in quality factor compared to fast cooling. Measurements were performed at 4 K, modified [36].

A time of 2 h spent within the critical temperature window reduced the quality factor by roughly one magnitude. The additional heating from hydrides at 1 MV/m is given by:

$$\Delta P_{\mathrm{c}} = \frac{(E_a \cdot l)^2}{\frac{R}{Q}} \left(\frac{1}{Q_{0,slow}} - \frac{1}{Q_{0,fast}} \right) = 2\,\mathrm{W}$$

Trapped Magnetic Flux

Niobium is a type II superconductor that expels all external magnetic fields below H_{c1}. However, in resonators, the meißner effect is disrupted by lattice defects and inhomogeneities in the bulk material, causing 'pinning' of DC flux lines. The oxide layer is suspected to be the origin of flux trapping [25]. Each flux quantum possesses its own vortex current with a normal conducting core. The DC field decays over the distance λ_L from the center, with a core size of ξ_0. If 100% of the external magnetic field H_{ext} would be trapped in an area A, the number of fluxoids is given by:

$$N = \frac{AH_{ext}}{\Phi_0} \tag{5.17}$$

$\Phi_0 = \frac{h}{2e} \approx 2 \times 10^{-11}\,\mathrm{Tcm}^2$ is the flux quantum. In Figure 5.7, the distribution of magnetic field, supercurrents, and nc density of states of a vortex are shown. The normal conducting area is given by $A_{nc} = N\pi\xi_0^2$. The additional resistance due to flux pinning, denoted as R_{mag}, is the ratio of the normal conducting to superconducting area:

$$R_{mag} = N\frac{\pi\xi_0^2}{A}R_{nc} = \frac{H_{ext}\pi\xi_0^2\mu_0}{\Phi_0}R_{nc} \tag{5.18}$$

The critical magnetic field $H_{c2} = \frac{\Phi_0}{2\pi\mu_0\xi_0^2}$ represents the upper limit of a type II superconductor. This allows us to rewrite Equation 5.18 as:

$$R_{mag} = \frac{H_{ext}}{2H_{c2}}R_{nc} \tag{5.19}$$

Niobium with $RRR = 300$ has the critical magnetic field of $H_{c2} = 240\,\mathrm{mT}$ and a normal conducting surface resistance of $R_{nc} = 1.5\,\mathrm{m\Omega}$ at a frequency of 1 GHz. The conductivity is given by $\sigma = \sqrt{\frac{1}{\rho\mu_0\mu_r f}}$, and the resistance is inversely proportional to σ and results in Equation 5.20[25]:

$$R_{mag} = 3000[n\Omega]H_{ext}[mT]\sqrt{f[GHz]} \tag{5.20}$$

The additional magnetic resistance for the 360 MHz CH structure with the magnetic field in Germany of $H_{ext} = 50\,\mathrm{\mu T}$ results in $R_{mag} = 90\,\mathrm{n\Omega}$. This is twice the BCS resistance value and diminishes the Q-value and maximum gradient, similar to the hydride example. Superconducting RF resonators require shielding from the magnetic field. High-permeability metals (μ-metals) reach values of $\mu_r = 10^5$ and surround the cryostat. The magnetic field is guided by the μ-metal and lowers the penetrating magnetic field by a factor of 10 to 50. In the case of the cryostat at IAP, the remaining magnetic field was measured to be 1.2 µT and results in a magnetic residual resistance of $R_{mag} = 4\,\mathrm{n\Omega}$.

5.6.2 Field Emission

The emission of electrons from material surfaces occurs at high electric field levels. Conducting electrons inside a metal are typically bound by a potential of as few eV. The vacuum or gas inside the cavity acts as an insulator, which is approximated by an infinitely wide potential barrier. When a constant electric field is applied, the outer potential energy for an electron is given by a constant slope.

$$V(z) = -eEz \tag{5.21}$$

Metals contain a high density of free electrons in their conduction band, which interact with the external electric field and rearrange accordingly. The displacement of the electrons results in an electric charge on the surface, equivalent to a hypothetical positive charge placed in front of the surface. This charge is used to calculate the total potential.

$$V_{II}(z) = -eEz - \frac{e^2}{16\pi\epsilon_0 z} \tag{5.22}$$

The binding energy is represented by a flat negative potential $V_I = -\phi$ on the metal side, while in a vacuum, $V = 0$. The electric field results in the discussed total potential as described in Equation 5.22, illustrated in Figure 5.10.

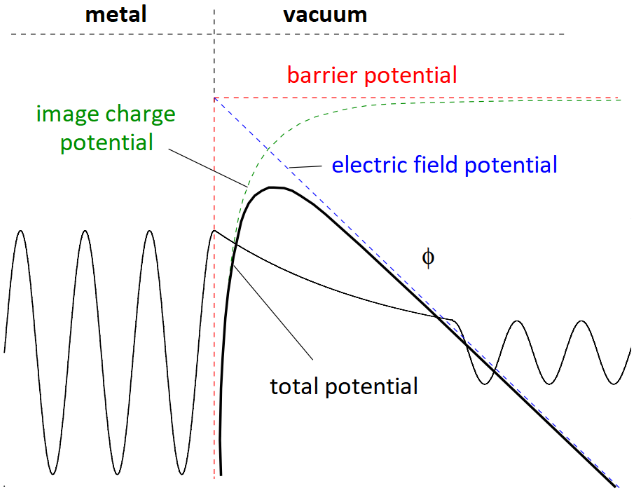

Figure 5.10: The total potential barrier outside of the metal surface for an electron, modified [24].

The solutions of the electron states are determined by solving the Schrödinger equation for the given regions and with respect to the boundary conditions. The probability of residence declines exponentially inside the potential barrier and becomes non-zero in region III, where the potential is approximately given by $V_{III}(z) = -eEz$. R.H. Fowler and L. Nordheim have solved the tunneling current density for this case[5].

$$j = \frac{e^2E^2}{8\pi h\phi t^2(z)} \exp\left(-\frac{8\pi\sqrt{2m(e\phi)^3 v(z)}}{3heE}\right) \tag{5.23}$$

In the case where $t(z) = 1$ and $v(z) = 1$," representing a triangular potential, the current density follows the modified Fowler-Nordheim law [25].

$$j(E) = \frac{A_{FN}E^2}{\Phi} \exp\left(-\frac{\beta_{FN}\phi^{\frac{3}{2}}}{E}\right) \tag{5.24}$$

Here, $A_{FN} = 1.5 \cdot 10^6$, E is the electric field at the surface of the field emission in MV/m, and Φ is the work function of the material. Due to the exponential nature of the emission current, the intrinsic quality factor falls rapidly with increasing electric field.

Electrons that tunnel through the barrier are further accelerated in the RF field of the cavity and hit the cavity wall. This effect can lead to high amounts of x-ray radiation (bremsstrahlung) and produces heat at the collision area. The RF power absorbed by the electron beam is assigned to the total cavity losses P_c and the intrinsic quality factor drops.

Field emission is shown to be heavily reliant on surface preparation and cleanliness. Microcontaminants are identified as dominant emitters. HPR and clean room assembly can drastically improve cavity performance, as discussed in Section 8.5. Further in-situ processing options for emitters include RF cw conditioning, pulsed high RF power, and helium processing. Emission currents are observed well below the associated theoretical field levels. This amplifying property of an emitter increases the effective local field strength by the factor β_{FN} and is determined by its geometry. With a decreasing emitter peak radius, the enhancement factor rises. The macrostructure alone would yield enhancement factors β_1 well below the observed values β_{FN}. Due to the surface roughness, an additional field enhancement β_2 takes place. This 'tip-on-tip' model gives the expression $\beta_{FN} = \beta_1 \cdot \beta_2$ [25]. The field emission current is supplied by the active emitters, typically representing 10% of the total potential emitters. When the current is intense enough and impact is made in a region of the high magnetic field, field-emission-induced thermal breakdown via BCS feedback model occurs. A fraction of the electron energy is converted into x-ray 'bremsstrahlung' at impact. This can lead to high doses of x-ray radiation emitted by the cavity, ranging from microsieverts up to sieverts per hour. A scintillator has been used to determine the radiation flux at the working station close to the cavity. Variations in radiation strength could be observed during emitter processing procedures such as helium processing, which will be discussed in Section 6. During the measurement evaluation, the term 'onset' of field emission will be used for every performance result discussion. The field emission current rises exponentially, and technically,

---

[5] Published in 1928

quantifying an onset value is inappropriate. In this context, the term ’onset’ is defined as the field level at which x-ray radiation originating from the cavity can be detected directly above the cryotank lid by the scintillator detector.
The Fowler-Nordheim equation can be converted to determine β_{FN} of the dominant emitter. Applying the emitter area A_e to Equation 5.24 results in the tunnel current $I(E)$ that can be brought into the following form:

$$\ln\left(\frac{I(E)}{(\beta_{FN}E)^{2.5}}\right) = \ln\left(\frac{A_{FN}A_e}{\phi}\right) - \frac{B_{FN}\phi^{3/2}}{\beta_{FN}E} \tag{5.25}$$

Plotting of $ln\left(\frac{I(E)}{(\beta_{FN}E)^{2.5}}\right)$ against 1/E results in a straight line for data points affected by field emission. The enhancement factor β_{FN} can be calculated from the slope m

$$\beta_{FN} = \frac{B_{FN}\phi^{3/2}}{m} \tag{5.26}$$

The work function is $\phi = 4.4\,\mathrm{eV}$ for niobium. The tunneling current is derived from the difference between the total losses and the ohmic losses P_c. To receive the ohmic losses at high field levels, the total losses are fitted at low field levels, where no field emission is present. Values for β_{FN} can range from 100–10000 depending on surface cleanliness. Post HPR and RF processing the 360 MHz cavity exhibited an enhancement factor $\beta_{FN} = 190$ compared to the baseline measurement, where the cavity showed $\beta_{FN} = 96$.

5.6.3 Q-Slope

Niobium cavities exhibit different behaviors for Q_0 with an increase in E_a and are characterized by three field strength sections. These regions are associated with different mechanisms causing the low-, medium-, and high-field Q-slope. Studies on the Q-slope have predominantly been conducted on elliptical cavities at 2 K. In Chapter 3.2, the Q-slope behaviors of CH cavities are summarized and analyzed with the information from this chapter.

Low-Field Q-Slope

An increase in Q is observed at low field levels and reaches its maximum in the range of 15–20 mT. The maximum Q value is expected to correspond to the traditional BCS resistance value [30]. Baking at 100 °C for 48–60 h or 120 °C for 60 h enhances the low-field Q-slope. Subsequent HF rinsing restores the Q-slope to its behavior before the baking and suggests that the formation of metal-oxide layers on top of the bulk niobium surface introduces localized states in the gap region, that effectively reduce the gap. These states effectively reduce the energy gap. At low RF fields, these states remain out of thermal equilibrium due to a mismatch between the photon absorption rate from the RF field and the quasiparticle relaxation rate by phonon scattering [30]. As the field levels increase, these states reach thermal equilibrium, and the full energy gap is restored.

Medium-Field Q-Slope

A Q-drop in the range of 20 to 80 mT by a factor of 2 up to 8 can be observed for most structures. The drop in Q corresponds to an increase in resistance and, therefore, cavity losses. Experiments have shown that the metal-oxide layers do not affect the medium Q-slope, as evidenced by HF rinsing and regrowth of the oxide layer before each test. Typically, x-ray radiation 'onsets' for higher field levels, and electron emission does not play a dominant effect in this range. All models are based on the interaction of the peak magnetic field with the SC surface and are suited to explain the medium Q-slope for different cavity frequencies.

The 'Thermal Feedback' model is based on the increase of BCS resistance due to RF heating. This effect is driven by the exponential temperature dependence of the BCS resistance. For high-frequency cavities ($f > 2.5\,\mathrm{GHz}$), this model led to the 'global thermal instability'(GTI) effect, which predicted cavity quenching below the critical magnetic fields. GTI was confirmed through measurements of several elliptical cavities above 2.5 GHz [42], [43]. For frequencies below 2.5 GHz, the observed medium Q-slope is stronger than the thermal feedback model with standard BCS resistance predicts, and no GTI is observed. Important parameters for the medium Q-slope include the phonon mean free path and thermal conductivity. Large grain cavities with higher thermal conductivity and higher phonon peak show lower medium-field Q-slope. The results of the thermal feedback with non-linear BCS for low-frequency structures are mixed. Fitting of experimental data for baked cavities required only the quadratic contribution of the non-linear BCS effect, since the full non-linear effect would overestimate the q-slope. The full non-linear BCS model has been successfully applied to explain experimental data of non-baked cavities.

High-Field Q-Slope

At peak magnetic fields above 90 mT a rapid increase in Q-slope is observed, even in the absence of field emission. A known treatment for high-field Q-slope reduction is a mild cavity bake at 120° for 48 h under ultra high-vacuum. The electric field is ultimately limited by cavity quenches or the breakdown of superconductivity.

The origin of these anomalous losses is not yet clarified and an ongoing research field in the SRF community. Multiple mechanisms are expected to affect these high-field losses. Analysis of material properties and treatment effects is performed on niobium cavities and samples. Cavities allow direct measurement of performance changes, heat responses, quench behavior, etc., while samples are used to directly spectroscopically examine the changes in the bulk and surface layers. Temperature mapping shows the existence of localized hot spots within the magnet field region of elliptical cavities. The onset field level of the high-field Q-slope is widely found to be associated with surface roughness. This correlation is consistent with the observed difference between electropolished (EP)- and BCP-treated cavities. EP cavities have fewer surface roughness of 1 to 5 µm compared to BCP cavities with 5 to 10 µm. Mild baking of 120°C for 48 h showed an overall improvement of the high-field Q-slope and is currently the most effective and reliable treatment option. EP cavities benefit more from this procedure than BCP cavities. In addition to the etching method used, the baking results are further found to be dependent on the niobium crystal structure in combination with the material processing method used. The standard procedure before etching is shown in Figure 5.11.

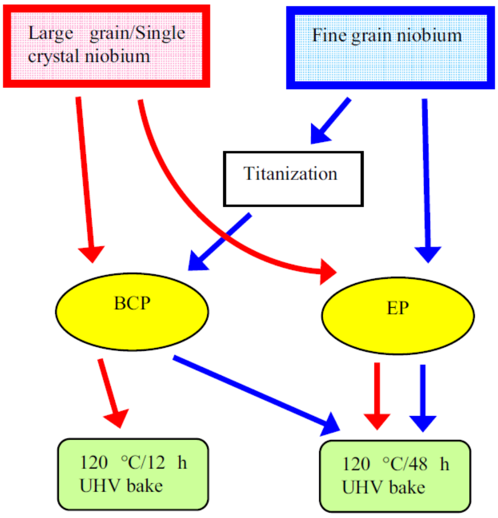

Figure 5.11: The difference in baking time refers to the minimal time required to see the full baking effect. All EP and fine grain BCP cavities require 48 h bakes, while large grain BCP cavities need at least 12 h baking time [44].

Theoretical predictions of RF losses from vortices at high field levels are consistent with the formation of hot spots. Two different types of vortices are possible candidates for this effect. Pinned vortices can form spatially inhomogeneously during cooldown from residual DC magnetic field at impurities and crystal defects. The pinning strength of pure niobium is fairly weak compared to NbTi and Nb_3Sn and allows for vortex displacement at thermal gradients of

$$|\nabla T|_c \approx \frac{J_c \mu_0 T_c^2}{2 B_{c1} T} = 1.5\,\mathrm{K/mm} \tag{5.27}$$

where $J_c = 1\,\mathrm{kA/cm^2}$ is the critical depinning current density, $B_{c1} = 170\,\mathrm{mT}$ is the lower critical field at $T = 2\,\mathrm{K}$, and $T_c = 9.25\,\mathrm{K}$ is the critical temperature. Depinning of vortices and changes in cavity hot spots with a temperature gradient was observed at JLab, where a heating unit provided the temperature gradients of 0.5 K [45]. Thermal mapping showed a permanent redistribution of hot spots after the local heat treatment. It is expected that thermal gradients allowed for redistribution of vortices over a larger

area.
Vortices can locally form at fields close to the lower critical magnetic field B_{c1}, as the critical field is dependent on the geometry and its associated demagnetization coefficient $D(\mathbf{x})$. The local critical magnetic field threshold is given by:

$$B_{c1}(\mathbf{x}) = B_{c1} \cdot (1 - D(\mathbf{x})) \tag{5.28}$$

A vortex enters the surface as the local critical field is surpassed. When the RF field changes direction, the initial vortex is pulled toward the surface again and a formed anti-vortex penetrates the surface and both vortices annihilate themselves. This procedure repeats for every RF cycle.
Heating from vortices produces weak local temperature increases that massively impact the local BCS resistance. This non-linear effect is estimated by [46]:

$$R_s(r) = R_{BCS}(T_0, \omega)\coth^{\sigma}\left(\frac{\pi r}{4d}\right) \tag{5.29}$$

$$\sigma(B_p, T_0, \omega) = P_0(B_p, T_0, \omega)\frac{\Delta}{k_b \pi \kappa(T_0) T_0^2} \tag{5.30}$$

Here, P_0 represents the dissipated power at the local heat source of size r_0, κ denotes the thermal conductivity, Δ is given by the energy gap, and T_0 is the helium bath temperature.
Niobium is also an active metal that reacts with water, producing high partial pressures of hydrogen.

$$x\mathrm{Nb} + y\mathrm{H_2O} \rightarrow \mathrm{Nb}_x\mathrm{O}_y + y\mathrm{H_2} \tag{5.31}$$

All processes that remove the protective oxide layer trigger this process, resulting in adsorbed hydrogen that is sealed into the bulk by the new oxide layer. The sealed hydrogen can potentially form blisters and Nb-H phases. For EP an anodic current is applied, that ideally suppresses hydrogen evolution at the Nb surface [47]. In reality, current distribution and shielding from polarization current can enable hydrogen evolution. The BCP etching rate is controlled by temperature, with an additional dependence on the hydrogen diffusion rate with temperature. For this reason, BCP acid temperature is typically kept below 15°C.
Hydrogen concentration distribution of BCP-treated niobium samples was measured before and after low baking at temperatures ranging from $90 - 140°\mathrm{C}$ for 48 h, see Figure 5.12.

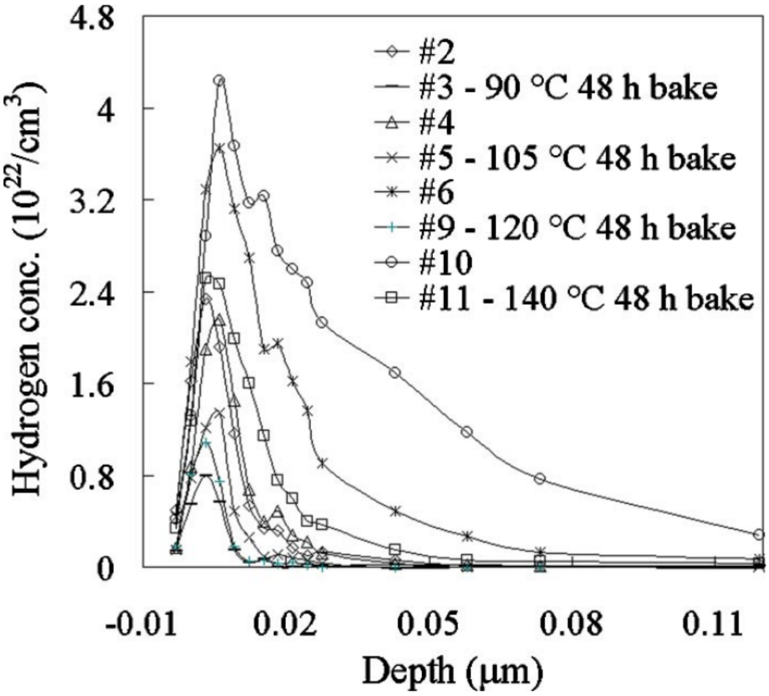

Figure 5.12: Change of hydrogen concentration in the surface layer depends on temperature and is consistent with the observed Q-slope benefits.[48]

The 140°C sample showed small amounts of released hydrogen and suggests that hydrogen was able to redistribute into the bulk. It is not clear how hydrogen can pass the oxide barrier, a plausible explanation is that vacancies and oxygen atoms have increased mobility during the bakeout, allowing hydrogen to redistribute. Desorption of hydrogen is considered less likely because the oxide layer does not dissociate significantly up to 200°C [49]. These findings show that hydrogen concentration at the surface layer is correlated with the Q-drop. A more complete model is expected to involve effects from hydrogen and oxygen, which are present in large quantities within the RF penetration depth.

6 Preparation of the 360 MHz CH Cavity

The performance of superconducting accelerators depends on the quality of the base material used and its surface properties. High-purity niobium is crucial for cavity performance and is quantified by the residual resistance ratio (RRR) value. The RRR value is calculated as the ratio of the normal conductive resistance at 300 K to the normal conductive resistance at 4 K.

As discussed in Chapter 5, it was shown that electrical and thermal conductivity are generally proportional to each other for many materials. Higher electrical conductivity also leads to higher thermal conductivity in the case of niobium. The heat generated during operation can be dissipated more efficiently from the cavity to the helium bath compared to an identical cavity with a lower RRR value. Chapter 5.1 demonstrates the temperature dependence of the BCS resistance, revealing a rapid increase in resistance with temperature. If heat dissipation is insufficient, it can trigger a feedback effect leading to the breakdown of superconductivity. High electromagnetic field strengths can generate heat due to electric and magnetic effects.

In this work, in-situ treatment options were performed to a 360 MHz CH cavity. These processes are employed to optimize electrical or magnetic properties in the field of superconducting cavity preparation. The ultimate goal of these treatments is to enhance accelerator performance, which is determined by measuring the Q/E curve.

6.1 High Pressure Rinsing at HIM

High-pressure rinsing is a fundamental treatment in the field of superconducting resonator preparation. HPR is a standard procedure after chemical surface treatments to remove residues and particles. Furthermore, it is used in recovery protocols of cavities with dropped performance. Possible causes of dropped performance range from contamination of the resonator due to faulty or unintended ventilation, accidents, material failure, and degradation of surfaces due to particle impact during operation. HPR treatment was performed in collaboration with the Helmholtz Institute Mainz (HIM). Preparation on open superconducting cavities has generally to be performed in a clean room setting to minimize contamination of inner surfaces.

6.1.1 Clean Room

One of the primary sources of contamination is airborne particles. These particles can settle on the cavity's surface during the manufacturing process, adversely affecting its performance. Therefore, clean rooms must be designed to maintain a high level of air cleanliness, typically achieved through advanced filtration systems, airlocks, and positive air pressure. This ensures that the air inside the clean room is continuously replaced with filtered air. Clean rooms are exclusively classified by their particle size and concentration per cubic meter of air according to the ISO 14644-1 standard. This classification ranges

from ISO 1 to ISO 9, with ISO 1 allowing the lowest concentration of 0.1 µm particles, and increases from there with each classification grade.
The clean room at HIM is divided into an ISO-class 6 (clean room 1) and an ISO-class 4 (clean room 2) area. These rooms, along with the adjacent gray rooms and airlocks, form an area of 155 m^2. Clean room 2 maintains slightly higher pressure compared to clean room 1 to prevent particles from entering through the air slits of the connecting door and material lock. This principle applies to all adjacent rooms of different ISO classifications. A schematic overview of the clean rooms is shown in Figure 6.1.

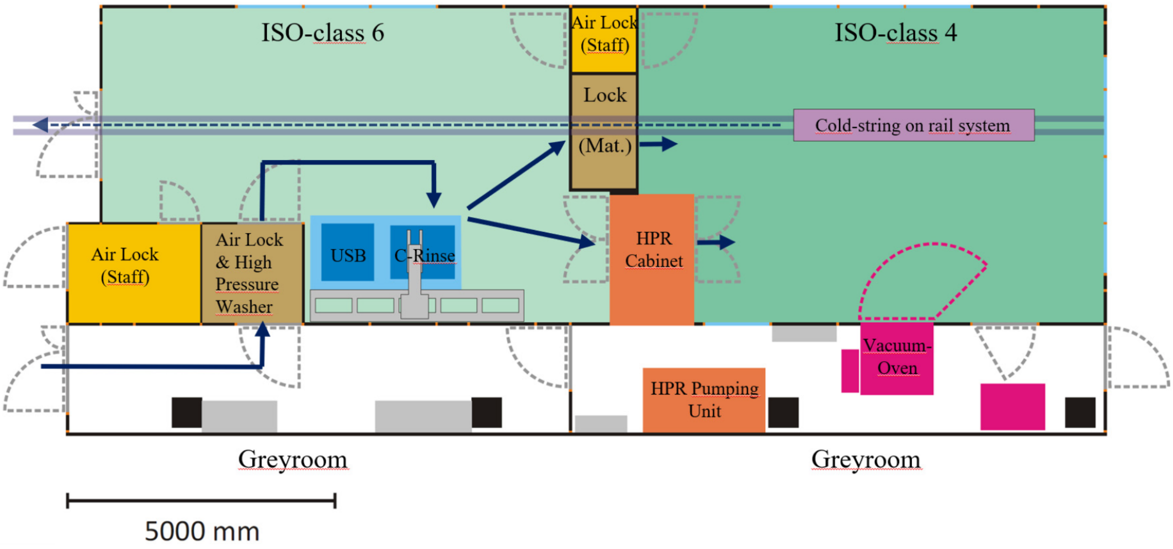

Figure 6.1: Sketch of clean room at HIM, [50].

Clean room 1 is used to clean and prepare components and cavities for HPR treatment and assembly inside clean room 2. It has two mobile ultrasonic baths for small to medium-sized components. Cavities, on the other hand, are cleaned by an installed ultrasonic bath and conductivity sink. A lifter is installed on the wall next to the sinks and allows for safe operation. Cavity transportation is performed using a mobile lifter. The lifter itself produces particles from abrasion during operation. The number of particles produced lessens with decreasing lifter velocity [51]. To reduce contamination risk, Slow movements are generally recommended for all applications inside a clean room. The HPR cabinet is accessible from clean rooms 1 and 2. After ultrasonic cleaning and conductance rinse, the cavity is placed on a rotatable table inside the cabinet via a mobile lifter. The table has three conical recesses that secure and align the cavity. Alignment deviations can be compensated through three adjusting screws that change the table's inclination. The HPR wand, controlled via a terminal located next to the cabinet in clean room 1, can be equipped with different nozzles to adjust the spray angle and water flow. After cleaning, the cavity is transferred to clean room 2 for drying and assembly. In clean room 2, the cavity is permanently mounted on the mobile lifter, elevated below the ceiling where laminar flow accelerates the drying process and further reduces particle contamination. Assembly is the final critical step, which has to be performed carefully, to avoid cavity contamination. Cleanroom 2 is equipped with a particle counter and a deionized nitrogen gun to remove all components from residual particles after the ultrasonic bath. All flanges, gaskets, screws, and washers are sprayed above the particle counter until no more particles are detected. They are then placed on a separate stainless steel table. This table is regularly cleaned and covered in clean room wipes to minimize particle generation. During assembly, the cavity on the mobile lifter is aligned to ensure that the corresponding flange opening points obliquely toward the floor, preventing particles from falling into the cavity during the screwing process. After assembly, the cavity is leak-tested and then discharged from the clean room.

6.1.2 HPR Preparations

Before conducting HPR on the 360 MHz cavity, several tasks needed to be addressed:

- The geometric structure of the cavity required a new nozzle layout to optimize rinsing results.
- Given the restrictive geometric parameters of the cavity concerning HPR application, it was decided to practice the HPR procedure on a CH dummy with a similar aperture.
- Cavity preparation takes place inside a clean room setting at HIM, necessitating adherence to existing clean room standards. A new mounting system was developed and built in collaboration with the mechanical workshop of IAP to meet these requirements.

Nozzle Layout

The goal of HPR is to remove impurities and particles from the inner cavity surfaces. For CH structures, using additional purge ports to cover the surfaces has become a standard practice. However, the 360 MHz prototype is unique in that it has no purge ports and can only be purged via the beam axis. This presents the challenge of designing a nozzle layout that prioritizes critical surface areas. To address this issue, RF simulations were conducted using CST [23] to identify these areas. The CST eigenmode solver was employed to calculate the electromagnetic fields of the H_{211} mode.

The field level was scaled up to the highest measured voltage, and the associated peak electric field levels on all surfaces were analyzed. The Fowler-Nordheim enhancement coefficient was used to estimate the emitter's field level based on the corresponding surface's peak electric field. The enhancement coefficient of the 360 MHz prototype was determined to be 240 during the cold test of its highest performance. This resulted in field levels at the emitters reaching GV/m for a few MV/m. The identified critical areas with peak electric field levels are shown in Figure 6.2.

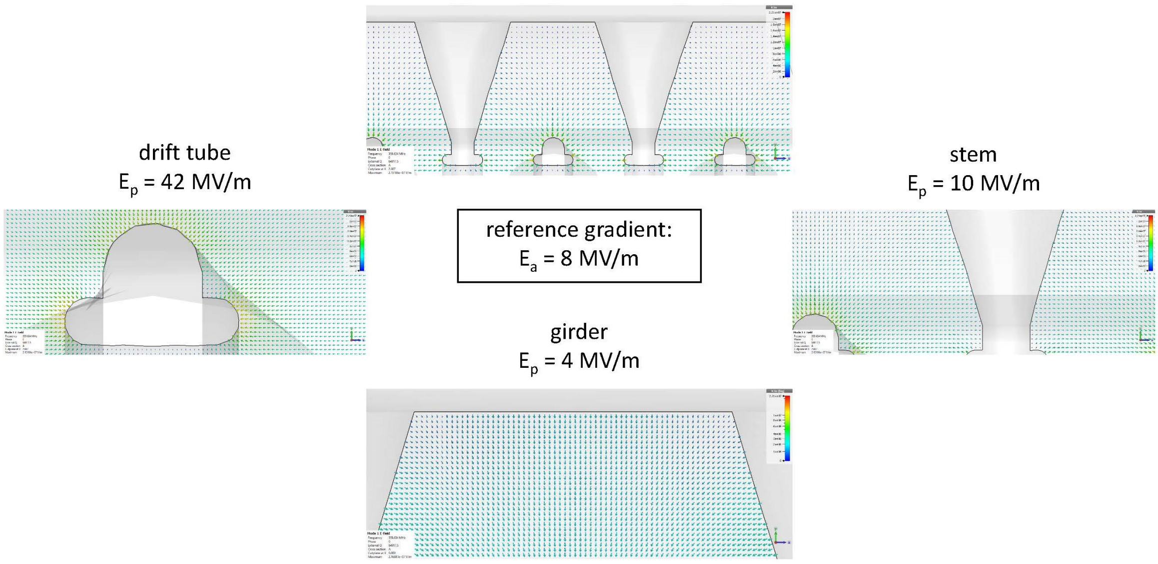

Figure 6.2: Electric field inside an acceleration cell of the 360 MHz CH cavity. Due to the electric field flatness within the resonator, any inner cell can be used as a proxy for the determination of critical surfaces within all cells. Simulations have been performed using CST [23]

.

Historically, all CH structures have been purged by Research Instruments[6] using a 15° tangential nozzle. The area coverage of the cells can be examined through drawings due to the cylindrical symmetry. For the 360 MHz cavity, it was decided to perform HPR cycles with two different water angles. The 15° nozzle, already available at HIM, was set as the first set angle. The second angle was chosen to reduce blind spots and therefore increase total area covered. An angle of 27° was selected, as it offered significant additional area coverage and could be manufactured based on existing confidential nozzle designs from RI.

CH Dummy HPR Test

The cavity aperture of the 360 MHz CH structure is only 25 mm, which raised concerns for the safety of the inner cavity surface during the purge. The HPR lance has a diameter ranging from 14 to 15 mm, resulting in a remaining space of 5 mm between the lance and the beam axis surfaces. This value only holds true under perfect alignment of the cavity relative to the HPR lance. The length of the dummy cavity is only 0.3 m compared to the 1 m of the prototype. The main task of the CH dummy was to investigate if it was possible to successfully apply the HPR to a structure of the given aperture. We will see in section 6.1.4, that length discrepancy led to unexpected challenges.

---

[6] `https://research-instruments.de/en/`

The dummy cavity consists of a concept similar to that of a CH structure. Four stainless steel plates hold three cross plates arranged perpendicular to each other. The cross plates have a central hole of 25mm, over which a plastic imitation of a drift tube is screwed on. Two lids fix the assembly and are placed on a plexiglass cylinder, which stops the high-pressure jet. The dummy is fixed and aligned in the HPR table by means of three conical stainless steel feet, which are attached to the lower lid. Prior to the cleaning of all parts for the assembly in the cleanroom, the dummy was assembled in the experimental hall, see Figure 6.3.

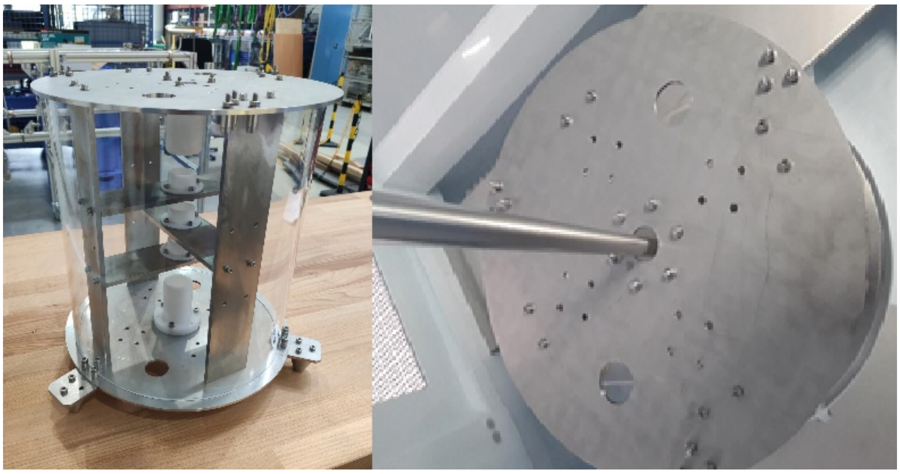

Figure 6.3: CH dummy was successfully assembled and purged with 100 Bar at HIM.

The dummy was then disassembled and prepared for assembly in the ISO class 6 clean room. All stainless steel parts and screws were pre-cleaned with acetone, followed by an ultrasonic bath. The drift tubes and the plexiglass cylinder were carefully wiped with isopropanol. Subsequently, the dummy was reassembled and placed in the HPR cabinet. The alignment between the HPR and the dummy was tested and revealed a slight offset of the lance from the aperture center. When rotated, the lance moved along an elliptical path inside the aperture, with a minimum residual space of 2 mm. Using this setup, the cavity was successfully purged with the 27° nozzle up to 100 % pumping power, equivalent to 103 bar of water pressure. For this pressure, a maximum lance vibration amplitude of 1.5 mm was observed through video analysis. Lance vibration was most pronounced during drift tube purging and disappeared during cavity wall purging. The offset of the lance from the aperture center point caused self-centering within the drift tubes, leading to vibration. Although lance vibrations were initially considered a significant concern, they did not cause any complications during the HPR tests. Before the dummy test, the HPR had only been performed with a SPEC nozzle for cleaning elliptical cavities and vacuum parts. This nozzle has larger water holes than the 15° and 27° nozzles. For comparison, the SPEC nozzle was tested up to 100 % of pumping power and compared to the 27° nozzle, as shown in Figure 6.4.

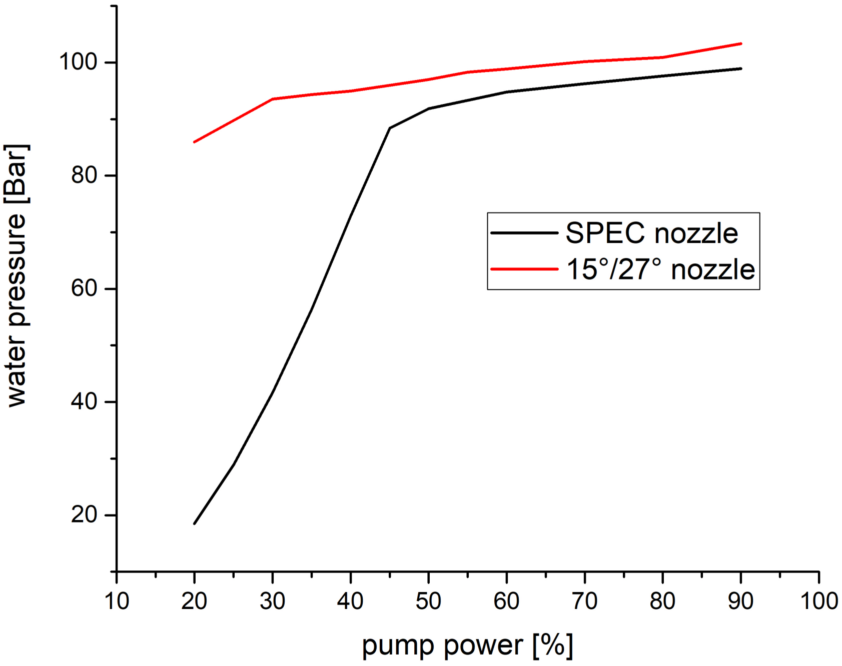

Figure 6.4: Pump power vs. water pressure for SPEC- and 15°/27° nozzle

The reduced diameter of the 15°/27° nozzle shows higher water pressure at lower pumping power. The 15° and 27° nozzles reach near maximum water pressure at 30 % of the pumping capacity. Any increase beyond this point in pumping capacity places additional load and stress on the compressor. Consequently, the pumping capacity has been limited to 30 % for the 360 MHz cavity HPR protocol, which corresponds to a pressure of 97 Bar. Each HPR test with the dummy cavity took about 1 minute, in contrast to the cavity HPR protocol which is set for 6 hours per nozzle and 12 hours in total.

Cavity Mount

The cavity mount was developed under the conditions set by the infrastructure of HIM. Cavity transportation is performed using mobile lifters at all times and requires cavity handover in between lifters. Additionally, the cavity has to be rotated after each HPR cycle to pour the remaining water out. Because HPR preparation occurs in a cleanroom setting, the mounting system is constructed from stainless steel, as aluminum, typically used for room temperature cavity applications, would develop an oxidation surface layer unsuitable for cleanroom use.

Each lifter is equipped with a stainless steel plate that forms the foundation for two diagonally placed stainless steel rods used to lift the cavity. This configuration allows for cavity rotation, necessary between HPR cycles to drain any remaining water. The pre-existing mount layout, designed for vertical cold tests, includes four threaded stainless steel rods, two aluminum lids, and two aluminum rings. The cavity is attached to the rings via clamps that connect to the reinforcement rings of the cavity. The upper lid connects to the mount system of the cryostat cover. The rods bring all components together and are secured in place with nuts and shims. The aluminum components were replaced with stainless steel, and the lids were modified to meet the specifications of the HPR table. For transportation and rotation, solid stainless steel corner pieces were attached to two plates with cylindrical cutouts.

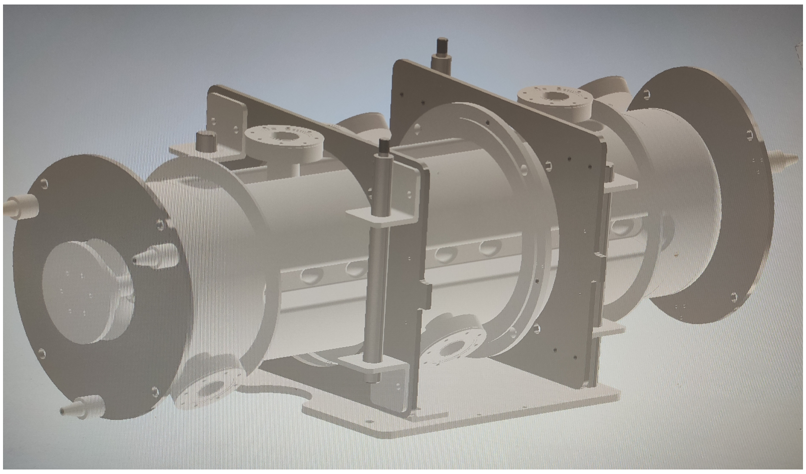

Figure 6.5: 3D model of the mounting system, created in Inventor [52].

All components are shown in Figure 6.5 and their respective weights are listed in Table 6.1. The total weight of all mount components and the cavity is 88 kg. The associated center of mass is located 0.3 m in front of the lifter, resulting in a substantial torque, necessitating the use of sturdy support forks and plates. The forks were made of stainless steel rods with a diameter of 30 mm. The forks were turned to a 16 mm diameter at the ends and were equipped with an M16 thread to ensure fork stability inside the support plate. The support plate was built from 20 mm thick stainless steel, while the lids and mount plates were constructed with a thickness of 10 mm. None of the plates and rings were delivered in a condition that is appropriate for cleanroom operation, so the surfaces had to be ground at IAP. Figure 6.6 displays the surface finish of the components before and after surface polishing.

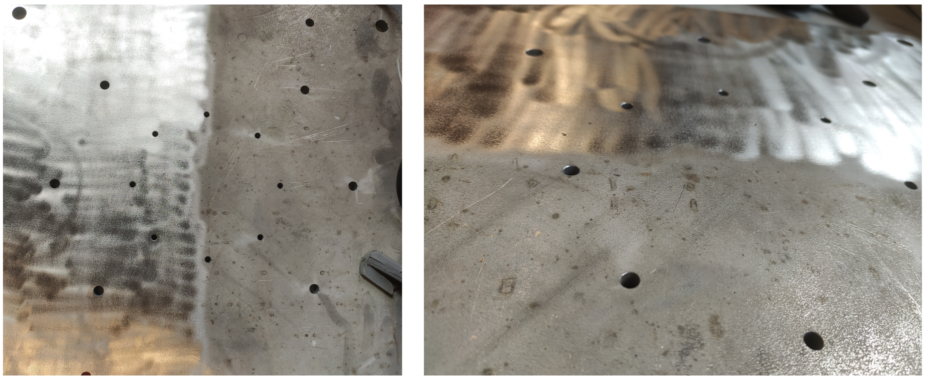

Figure 6.6: All stainless steel mount components had to be ground down as preparation for degreasing and ultrasonic bath cleaning at HIM. The picture shows a support plate as an example.

part	weight	quantity
lid	10 kg	2
corner piece	1 kg	8
mobile lifter mount plate	10 kg	2
cavity	40 kg	1
rod	3 kg	2
ultrasonic bath mount plate	15 kg	1

Table 6.1: List of all mount components and their respective weight. The total weight of the mounting system accumulates to 109 kg.

All parts were transported from IAP to HIM and the fixture was test-assembled without the cavity. Subsequently, a series of modifications were necessary because the cavity and the mounting system had small deviations from their models. The mounting system requires very small tolerances to ensure the safety of the operators and the clean room under cavity rotation. Before insertion into the clean room, the mounting system has been tested, see Figure 6.7.

Figure 6.7: The mount was successfully tested with a mobile lifter in the experimental hall at HIM.

6.1.3 HPR Protocol

Rinsing programs are customized and managed through the HPR terminal in clean room 1. Figure 6.8 shows the settings of the rinsing protocol used.

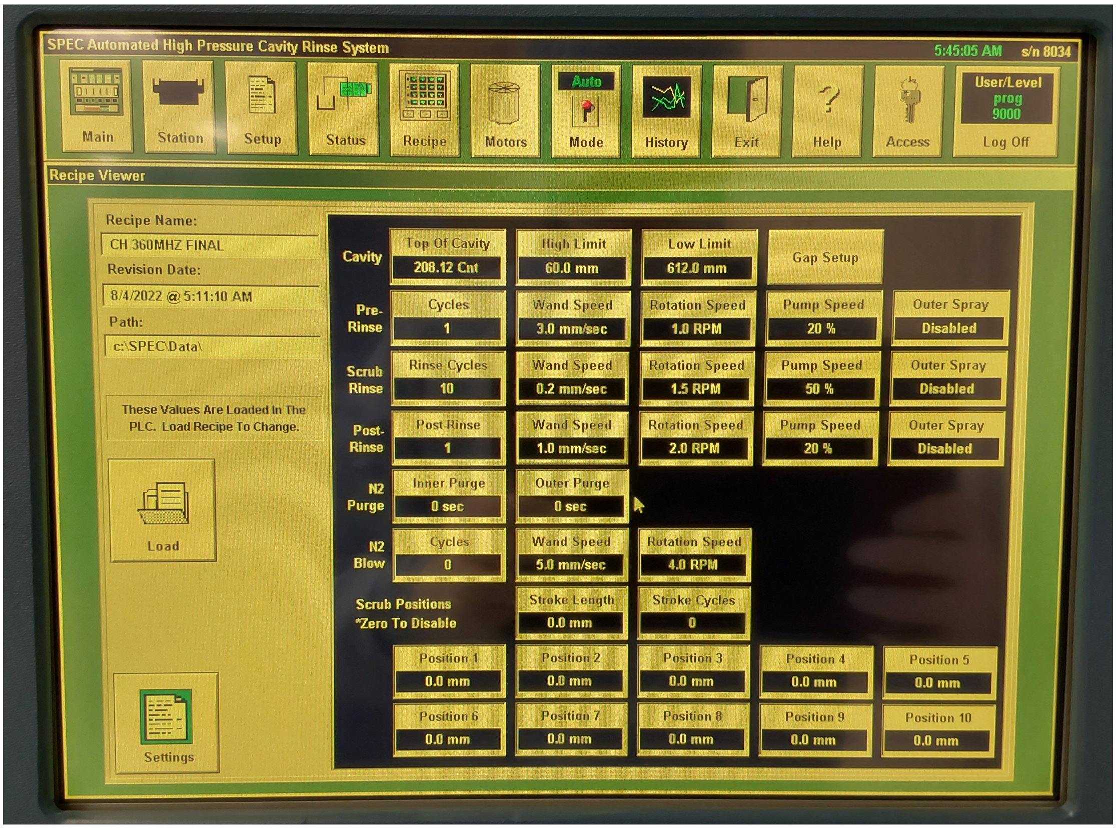

Recipe Name:
CH 360MHZ FINAL
Revision Date:
8/4/2022 @ 5:11:10 AM
Path:
c:\SPEC\Data\

These Values Are Loaded In The PLC. Load Recipe To Change.

Cavity	Top Of Cavity 208.12 Cnt	High Limit 60.0 mm	Low Limit 612.0 mm		
Pre-Rinse	Cycles 1	Wand Speed 3.0 mm/sec	Rotation Speed 1.0 RPM	Pump Speed 20 %	Outer Spray Disabled
Scrub Rinse	Rinse Cycles 10	Wand Speed 0.2 mm/sec	Rotation Speed 1.5 RPM	Pump Speed 50 %	Outer Spray Disabled
Post-Rinse	Post-Rinse 1	Wand Speed 1.0 mm/sec	Rotation Speed 2.0 RPM	Pump Speed 20 %	Outer Spray Disabled
N2 Purge	Inner Purge 0 sec	Outer Purge 0 sec			
N2 Blow	Cycles 0	Wand Speed 5.0 mm/sec	Rotation Speed 4.0 RPM		
Scrub Positions *Zero To Disable		Stroke Length 0.0 mm	Stroke Cycles 0		
	Position 1 0.0 mm	Position 2 0.0 mm	Position 3 0.0 mm	Position 4 0.0 mm	Position 5 0.0 mm
	Position 6 0.0 mm	Position 7 0.0 mm	Position 8 0.0 mm	Position 9 0.0 mm	Position 10 0.0 mm

Figure 6.8: Rinsing parameters of the 12 hour cleaning cycle.

The parameters are setting the vertical rinsing range, the lance velocity, the table rotation speed, and the pumping speed. In the cavity row, there are three parameters: Top of cavity is the reference height to which the nozzle is driven when the program is started and was chosen to be slightly above the beam axis flange. From there, the nozzle will be driven to the high limit point, which is a relative displacement from the 'Top of Cavity'. After reaching the high limit, the program automatically starts the rinsing cycle. With a value of 60 mm the nozzle was placed deep enough inside the cavity, that all spraying fans were exclusively rinsing the cavity and not the HPR chamber. The low limit is the relative displacement from the 'Top of Cavity' height, where the rinsing stops and the lance is driven back to the 'High Limit' before starting the next rinse cycle. The pre-rinse is a quick preparation where the cavity is pre-wet before the main "Scrub Rinse" and finished by a final and quick "Post Rinse". In figure 6.8 the parameters of each rinse type are shown. The "Scrub Rinse" parameters were adjusted for the 360 MHz cavity

from confidential internal documents given by Research Instruments and can therefore not be discussed in this work.
The protocol was used a total of four times, resulting in 12 h of rinsing time. Two times with the 15° nozzle, where the cavity was rinsed from both sides and then the procedure was repeated with the 27° nozzle.

6.1.4 CH Cavity HPR

The HPR preparation of the 360 MHz cavity involves the mounting of the holder and pre-cleaning inside the experimental hall, as well as the cleaning work and flange assembly inside the clean room. The design and testing of the mount system are discussed in section 6.1.2. After assembly, the cavity was degreased using acetone. During the cleaning process, silicone lubricant was found in the blind holes of the flanges. This necessitated the ultrasonic cleaning of the cavity with the flanges removed. Inside the material lock, the flanges were disassembled, and the cavity surface was cleaned from residual dust with ultra-pure water, after which it was left to dry overnight before insertion into clean room 1, as shown in Figure 6.9.

Figure 6.9: The cavity was cleaned from residual dust with ultra-pure water.

The cavity was then transferred to the ultrasonic bath's lifter using the cleanroom's mobile lifter. During the transfer, the weight of the cavity caused the ultrasonic bath lifter to tilt slightly, making it impossible to transfer smoothly through the apertures of the corner pieces. The resulting abrasion posed a contamination hazard to the cavity, and, therefore, the corner pieces were removed before running the ultrasonic bath, and the aperture was increased from 32 mm to 35 mm at IAP. The corner pieces were then pre-cleaned with acetone and cleaned by ultrasonic bath before insertion into the clean room. The transfer between lifters was then performed smoothly, and the ultrasonic cleaning of the cavity was carried out. The cavity was first cleaned in an alkaline solution for 1 h and then rinsed in a conductivity sink until the water conductivity of 0.05 µS/cm was reached. The lack of rinsing flanges led to poor water circulation in the bottom half of the cavity. Achieving the target value was accelerated by moving the cavity out of the bath and rinsing the critical area multiple times with an ultra-pure water spray head by hand.

The lance-cavity alignment was evaluated by moving the lance right above the cavity top and then rotating the cavity. Greater misalignment resulted in a bigger perceived elliptical path of the lance during cavity rotation. The ellipse could not be optimized below a minimal radius of 11 mm, with a center displacement from the aperture mid of 10 mm. These findings led to the investigation of the HPR system alignment. The lance was checked for both lot and transverse translation after height changes using a 1 m long stainless steel corner piece. The lot showed no angular divergence from table height to roughly 0.6 m. The lance was perfectly centered at table height and showed a transverse position shift of 8 cm per meter of height difference. The source of this shift was the improper alignment of the rail, which directs the movement of the HPR system. The rail was manually adjusted for 2 days, resulting in a residual transverse movement of 2 mm per meter of height difference. The lance-cavity alignment was again tested for both cavity directions. The lance remained inside the aperture under rotation for the first cavity direction. The cavity was then removed from the HPR cabinet and flipped via the mobile lifter. For this cavity orientation, the lance showed a larger ellipsis that could not be optimized to have the lance stay inside the aperture under rotation. The source of the error was bent threaded rods and a displaced lid from the cavity center. The resulting precision of the cavity could not be compensated for by the fine adjustment screws of the HPR table. Enlarging the drill holes from 18 mm to 22 mm of the respective end-plate allowed the cavity to be aligned centrally to the cavity despite slightly bent threaded rods. With these adaptations, the lance remained inside the top flange aperture under rotation for both orientations.

Before the automatic HPR test could be performed, the lance and nozzle had to maintain a sufficient distance of at least 2 mm from all drift tubes for the entire path. The lance was driven into the cavity step by step, where after each step the cavity fully rotated to ensure collision-free purging. During this iterative process, the lance and nozzle were observed through a telescope mirror until the nozzle passed the center drift tube. The HPR table fine adjustment is specific to each orientation and therefore has to be corrected each time the cavity is flipped. Practicing the process reduced the time spent inside the HPR cabinet to 5 minutes. The HPR was successfully tested for both orientations at 100 Bar of water pressure. Several actions and modifications that posed a risk for the introduction of particles to the cavity were performed after the first ultrasonic bath. Before executing the full HPR protocol, an additional ultrasonic cleaning was performed. The full HPR protocol consists of 12 hours of total rinsing time at 97 Bar, performed with the setup displayed in Figure 6.10. The settings of all parameters are listed in Section 6.1.1.

The cavity was dried for 3 days under laminar flow in clean room 2 and assembly of all flanges was performed. Each component, such as threaded rod, gasket, angle valve, etc., was sprayed with ionized nitrogen over a particle counter until no particles could be observed. The abrasion during the fastening of the parts itself leads again to the generation of new particles. For this reason, all flanges were aligned at an angle towards the floor during their assembly. The cavity was then leak tested in the clean room, where a leak rate of only 10^{-6} mbar/(l/s) was achieved. This leak rate ensured that no particles could enter the cavity during transport to Frankfurt and that the remaining work could be performed at IAP.

Figure 6.10: HPR setup at HIM: The cavity is positioned on an adjustable rotating table, from the top the lance is injected into the cavity through a beam axis flange.

6.2 RF Processing

RF processing of SC cavities is a widely and successfully used procedure to eliminate emitters and increase the maximum gradient. During this conditioning event, a particle explodes, leaving a crater and an area with melted material behind. These phenomena are referred to as "starbursts". The molten area of a starburst can extend up to hundreds of micrometers. Calculations of the heating due to field emission result in a possible melting radius $r_{melt} = 0.2\,\mu\text{m}$ [53] and dismisses field emission as the sole mechanism of the processing event. DC field experiments observed the formation of plasma in field emission experiments.

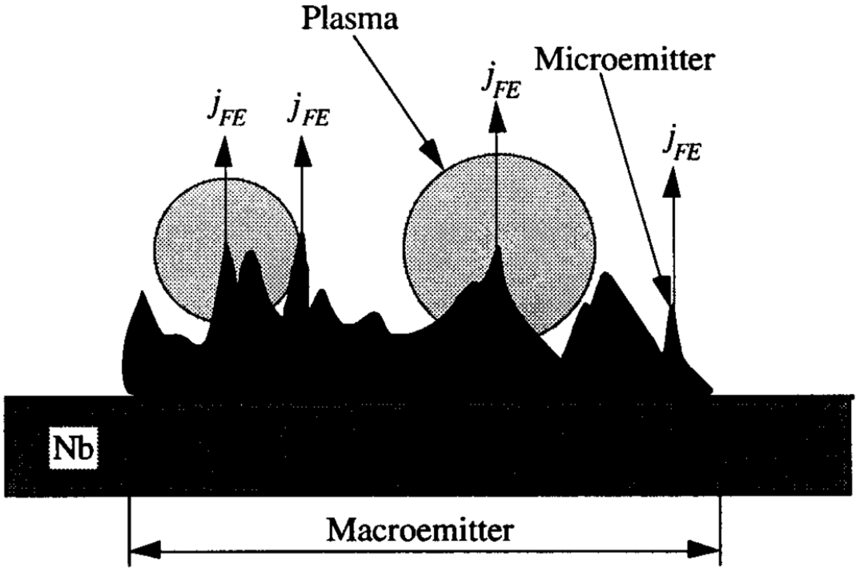

Figure 6.11: Emitters are composed of their macro size and microscopic surface texture [53].

Microemitters are the dominant source of emission current and heat-up. When the current density exceeds a threshold of $5 \times 10^{10}\,\text{A/m}^2$, the microemitter melts. The heating initiates local degassing of adsorbed neutral gas. At electric peak fields above 30 MV/m, the electrons gain 30 eV within a micron of the RF surface and are capable of ionizing the gas. Ion bombardment of the emitter produces further heat and emits further particles, resulting in an avalanche mechanism. When a microemitter explodes, the gas density is further increased. The avalanche ion bombardment is assumed to be the main contributor to the melting of the macro emitter, shown in Figure 6.11, as the electron current alone is insufficient. The addition of helium gas has been shown to help emitter processing [54], [55] and will be further discussed in chapter 6.3.

After the processing event, the field emission significantly decreases. The effect is quite substantial and leads to an increase of quality factor Q_0 at higher field levels, since total

RF losses and x-ray intensity decrease. RF processing can be performed from CW down to low-duty cycles in high pulsed power (HPP) operation.

CW Processing

For CW processing, the cavity is operated at field levels where emission occurs. In the case of the 360 MHz cavity, a slow and consistent change in P_r and P_t could be observed when the forward power P_f was kept constant. To minimize x-ray radiation, field levels slightly above the field emission onset were used for the initial processing. The first 8 hours of CW RF processing lead to small performance increases up to an event, where the cavity exhibited a substantial performance increase, as shown in Figure 6.12.

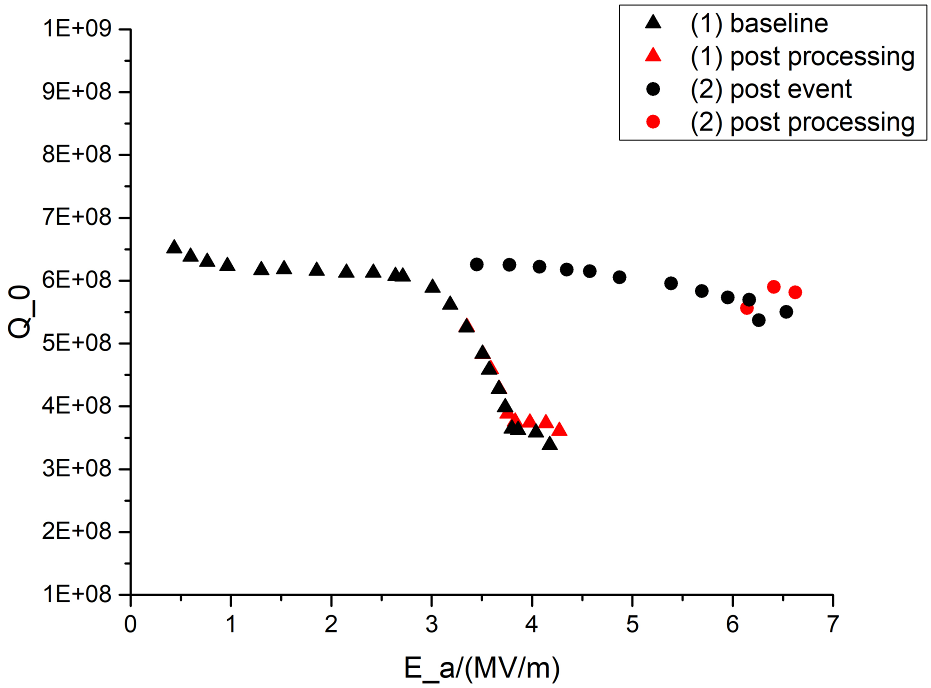

Figure 6.12: Emitter processing effectively started at $E_a = 3.8\,\mathrm{MV/m}$. After an event at $4.3\,\mathrm{MV/m}$, no more x-ray radiation was measured up to $6\,\mathrm{MV/m}$ and the quality factor Q_0 increased at higher field levels.

During emission processing, the emission current decreases, and the quality factor Q_0 rises. During the RF conditioning phase, this is observed via the power meters. The transmitted power slowly increases, and the reflected power increases in case of strong coupling. At 4.3 MV/m, a processing event took place, after which the RF control system was suddenly unable to hold the cavity in resonance. The cavity pressure reached a peak value of 3×10^{-6} mbar and fell back to a baseline of 7×10^{-10} mbar within 10 minutes. Radiation levels were monitored at the cavity and workstation, exclusively measured at the workstation for values above 3 µSv/h at the cavity. The processing event led to a steep decline in x-ray dosage at a given field strength and pushed the onset of field emission to 6 MV/m. Further CW RF conditioning followed the continuous pattern from before the event, as seen in Figure 6.12 (2) post-processing. Post-event, the cavity was RF conditioned for 10 more hours, leading to a further decrease in field emission and an increase in maximum gradient, as shown in Figure 6.13.

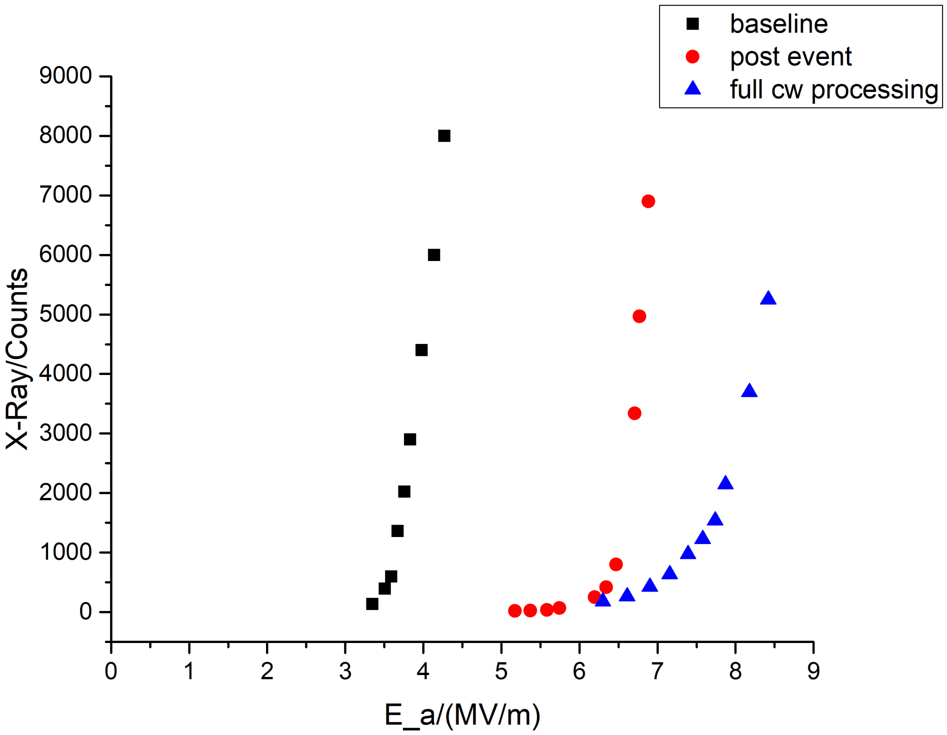

Figure 6.13: Emitter processing effectively started at $E_a = 3.8$ MV/m. After an event at 4.3 MV/m, no more x-ray radiation was measured up to 6 MV/m and the quality factor Q_0 increased at higher field levels.

This process took place after HPR cleaning of the cavity at HIM and a decrease in initial field emission compared to prior tests was found. During the first leak test of the cavity inside the ISO class 4 clean room, the air was sucked in and most likely contaminated the cavity with abrasions that were created during the assembly. With these contaminants, the cavity could be processed in contrast to the prior tests before HPR. With CW RF processing the gradient was more than doubled, resulting in the highest gradient achieved by this cavity.

6.3 Plasma Cleaning

Plasma cleaning of SC niobium cavities has the goal of increasing cavity performance by improving surface material properties. In Chapter 5.6.2, the modified Fowler-Nordheim equation was introduced:

$$j(E) = \frac{A_{FN}E^2}{\Phi}\exp\left(-\frac{\beta_{FN}\phi^{\frac{3}{2}}}{E}\right)$$

SC cavities experience increased losses from field emission at high gradients, which lower the breakdown threshold of superconductivity. Two distinct plasma cleaning procedures are performed and further investigated by laboratories all over the world. In both cases, the RF power required for plasma ignition is provided by the electromagnetic field of the cavity mode used. Room temperature plasma cleaning improves the work function ϕ of the surface material. Helium processing is performed at 4 K and can be understood as a form of amplified RF conditioning, that aims for the destruction of field emitters and reduction of β_{FN}.

Room Temperature Plasma Cleaning

Oak Ridge National Laboratory demonstrated that a plasma composed of neon and a small percentage of oxygen reduces hydrocarbon-related field emission. Studies of niobium samples from the Institute of Modern Physics showed that carbon contamination lowers the work function ϕ from 4.4 eV to 3.75 eV [55]. The lowered work function increases the emission current at a given electric field.

The experimental setup is cavity-structure specific, but the general concept remains the same. The cavity is constantly flushed with either an Ar/O_2 or Ne/O_2 mixture and pressure kept in the range of 50 to 100 mbar for an elliptical structure [56] and 5 to 8×10^{-3} mbar for a HWR structure [55]. The different pressures required originate from the glow discharge condition set by Paschen's-law,

$$V_B = \frac{Bpd}{\ln(Apd) - \ln\left(\ln\left(1 + \frac{1}{\gamma_{se}}\right)\right)} \tag{6.1}$$

where V_B is the breakdown voltage, p is the pressure, d is the gap distance, γ_{se} is the secondary-electron-emission coefficient of the gas atom, A is the saturation ionization in the gas at a particular E/p, and B is related to excitation and ionization energies.

Removal of hydrocarbons occurs due to two plasma-surface interaction mechanisms. First, physical sputtering occurs when ions bombard the inner cavity surface, causing desorption of the residual gas. The kinetic energy of the ions is provided by the bias voltage between the plasma region and the inner cavity surface and depends on electron energy. When ions cross the plasma sheet, they gain the respective voltage. Second, a chemical sputtering effect occurs, when ions with sufficient energy break chemical bonds within the surface layer and fragments react with the present flux of oxygen atoms, which produces volatile substances that desorb from the surface [57]. Experimental sequences with niobium samples and resonators at Oak Ridge National Laboratory showed a rebounding effect of hydrocarbons under high vacuum storage for 15 to 24 h, which depends on the total plasma processing time, as seen in Figure 6.14.

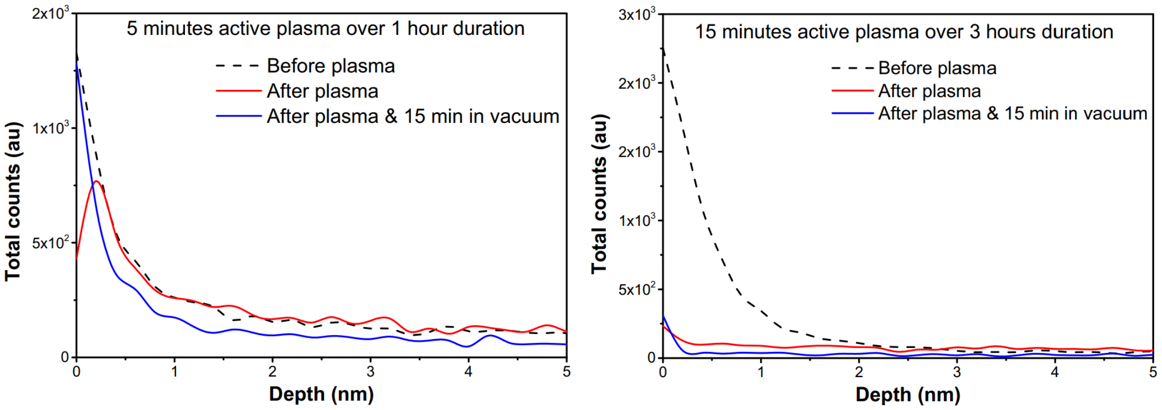

Figure 6.14: Hydrocarbons are present within the first couple of nm of the surface. For short total plasma cleaning times, a rebound within the top layer is observed [58].

Near-surface hydrocarbons within the bulk migrate towards the surface and resaturate the top layer. Plasma processing interacts only with the direct surface layer, and therefore requires multiple rounds with sufficient waiting times, resulting in a decrease of work function from $-0.7\,\mathrm{eV}$ to $-0.2\,\mathrm{eV}$. The migration process has an exponential temperature dependence, so preparation should be performed close to cooldown.

Even though room temperature plasma cleaning research was initially motivated by field emission, the increase in work function also has a positive impact on multipacting. Four elliptical 1.3 GHz 9-cell (Tesla) cavities that were prepared in a collaboration between Fermi National Accelerator Laboratory, SLAC National Accelerator Laboratory and Oak Ridge National Laboratory had experienced multipacting-related quenches. However, they did not experience any multipacting-related quenches post-plasma-cleaning [59].

Cold test of the HELIAC cavity CH1 showed multipacting that could not be conditioned within 2 weeks of processing time and had to be sent back to the manufacturer. A 325 MHz CH prototype also showed the onset of field emission at high field levels but did not quench due to MP. The source for multipacting onset at high field levels in some CH structures is not yet identified. Plasma cleaning could be considered a treatment option for cavities suffering from multipacting and further reduce field emission losses.

The possible advantages of plasma cleaning also come with inherent risks of the procedure itself. The main (copper) power coupler can sputter into the cavity, damaging the inner surface of the cavity. Excess plasma avalanches can also damage the niobium surface, resulting in early degradation. Multicell elliptical cavities are plasma cleaned with the use of the higher-order-mode (HOM) couplers. Sequential cleaning of each cell, with the respective mode of the cell, is performed to avoid ignition in the entire cavity. CH structures would need a dedicated power coupler for operation at room temperature, since the main power coupler for operation at 4 K is coupled weak with $\beta_e = \frac{Q_0}{Q_\mathrm{e}} \approx \frac{10^4}{10^8} = 10^{-4}$ to the point, where effectively almost no power is transmitted into the cavity. The complicated geometry of CH structures compared to elliptical cavities requires extensive research and experiments to safely handle this procedure, which is a promising and challenging field for further exploration of CH cavity treatment.

Helium Processing

Emitter processing has been introduced in Section 6.2, showing that a critical emission current is necessary to melt emitters. For both continuous wave (CW) and pulsed operations, there exists a maximum field level at which the cavity quenches and no further increase is possible. Since the electron current depends on the electric field present at the emitter, processing of the remaining emitter is not possible. However, the use of helium gas has been shown to enable further processing at similar field levels. The pressure increase with helium gas from 10^{-10} to 10^{-5} mbar increases plasma density, thereby increasing the ion current that destroys the macro emitter. Another theory suggests that helium ions saturate the surface and modify the electronic structure, affecting the field emission properties [53]. Helium processing inherits similar risks to the room temperature plasma cleaning case, where glow discharge can lead to damage to the power coupler and inner cavity surface.

Helium processing procedure of the 360 MHz CH cavity was taken from the CERN protocol [60] and consisted of a pressure increase to 5×10^{-5} mbar at 4 K and RF pulse length of 10 ms at a 50 % duty cycle. With increasing field levels, negligible X-ray radiation was observed and the cavity was considered unresponsive. Pulse length was then increased to 20 ms with a duty cycle of 67 %, resulting in a rapid onset of x-ray radiation. The cavity was processed for 3 h at a forward power of 50 W. Spatial x-ray doses varied abruptly during this process, showing emitter processing and activation of the previously inactive emitter. The experimental setup and measurement results are shown in Chapter 8.7.

6.4 Low Temperature Baking

A well-established cavity treatment to improve the high-field Q-slope involves a 120° C 48 h bake. EP-treated cavities tend to profit more from the baking than BCP-treated cavities do. The baking effects are preserved even after HPR, hydrofluoric acid treatments, and anodizing to less than 30 V [61]. Throughout this work, a 120°C 48 h bake was performed before HPR treatment and showed substantially lower high-field Q-slope post-HPR compared to results from 2007. The HPR treatment did not affect the cavity Q-slope to a measurable degree, which is in agreement with the literature. The 325 MHz was heat treated at 120°C under UHV for 48 h post-BCP and HPR and the results are shown in Figure 6.15.

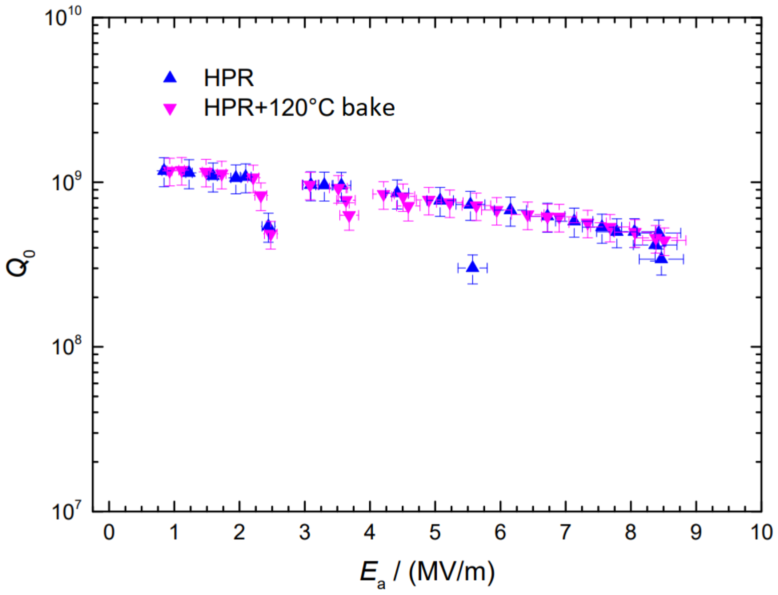

Figure 6.15: Intrinsic quality factor Q_0 of the 325 MHz CH cavity after BCP/HPR and low temperature baking [36].

No change in performance was observed in the case of the 325 MHz CH cavity. Low-temperature baking is also associated with a reduction of multipacting RF conditioning time required. Since this cavity is plagued with "harder" multipacting barriers, the effect of heat treatment can be inspected for this case. The barriers at 2.5 MV/m and 3.5 MV/m did not see improvement, but a prior high-field barrier at 8.5 MV/m did not show activation. Since low-temperature baking under UHV is overwhelmingly associated with positive performance effects, longer low-temperature bakes could be applied to future CH cavities plagued by multipacting. The effects of low-temperature baking for CH cavities were further studied for the 360 MHz CH cavity and results discussed in Chapter 8.4.

In the case of a ventilated HWR cavity, the field inside the cavity could not be established

within 8 h of RF pulsed conditioning. Subsequently, a 120°C bake for 1 h was applied, which allowed field establishment after 6 h of pulsed RF conditioning. However, it was limited by multipacting effects [55].
Elliptical cavities with high-field Q-slope can experience tremendous benefits from low-temperature baking, where quality factor and maximum field increase, as illustrated in Figure 6.16.

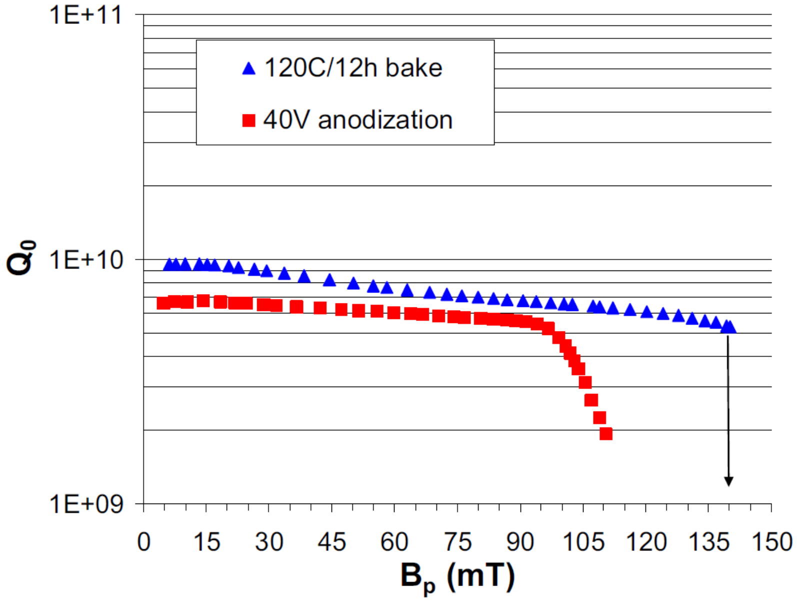

Figure 6.16: Q_0 vs. E_a of a 1.47 GHz single cell elliptical cavity etched by BCP and baked at 120°C for 12 h. The benefit of the bake was reversed back to baseline before baking by anodization of the cavity with 40 V at JLab [44].

6.5 Nitrogen Infusion

Ongoing research is focused on developing advanced baking procedures to further enhance the performance of superconducting cavities. The results from the same baking procedure vary significantly between different laboratories. Various baking recipes with different temperatures, baking times, and the use of a vacuum or the introduction of nitrogen or clean air at various pressures have been explored. Notably, low-temperature baking under a nitrogen flow has shown promising performance improvements, resulting in an increased Q-value across the entire electric field range and an increase in the maximum gradient [62]. However, it's crucial to acknowledge that the outcomes of these procedures are not always reliable and can sometimes lead to severe performance degradation.
One such infusion recipe consists of two baking phases. The first phase involves a 3 h bake at 800° C, which serves to break down the oxide layer and remove hydrogen and

oxygen. Subsequently, the temperature is lowered to 120–200° C, and the cavity is baked for 48 h with a constant injection of nitrogen at a maintained cavity pressure of 33 mbar.

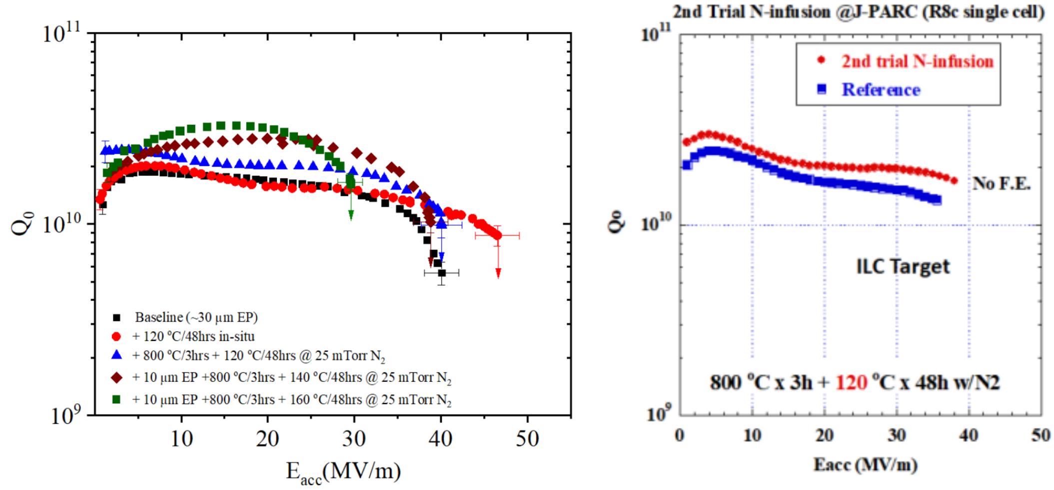

Figure 6.17: Q-E performance change of nitrogen infusion with different baking temperatures (left). A mid-to high-field Q-value increase with a diminished maximum electric field is observed with increasing baking temperature [63]. On the right, the top results of a nitrogen infusion series is shown, where quality factor and maximum electric field could be increased [62].

The precise mechanism behind the cavity performance changes is not clear, but it is suspected that the cleanliness of the furnace plays a critical role in the process. Cases of Q-degradation may be linked to contaminants originating from the furnace.
At Jefferson Lab, an increase in the quality factor was achieved with varying baking temperatures during nitrogen infusion [63]. However, it's important to note that the maximum gradient for any nitrogen infusion recipe fell short compared to the standard 120° C 48 h bake. Similar to cavities treated at J-PARC, the origin of field limitations is believed to be related to impurities introduced during nitrogen infusion.

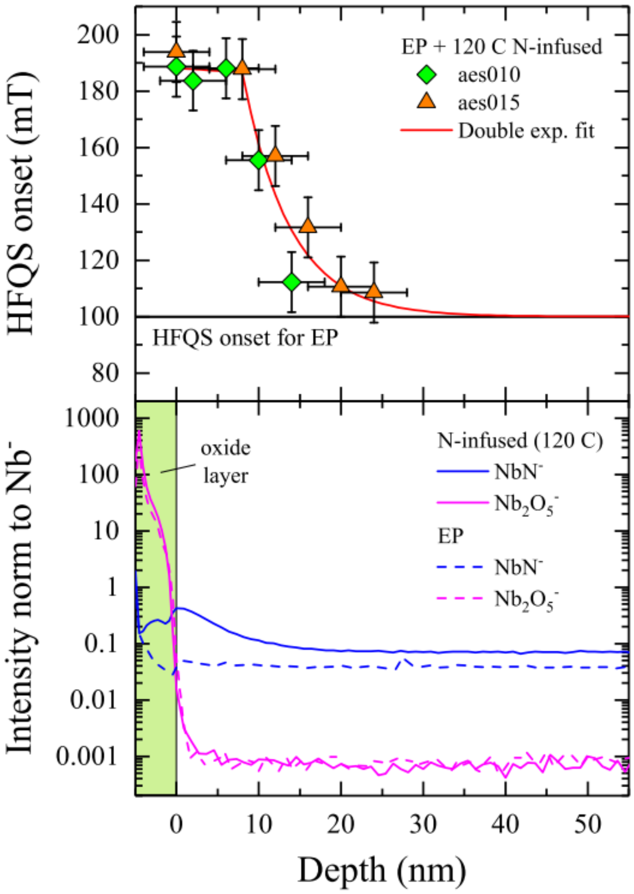

Figure 6.18: The effect of nitrogen infusion is correlated to the elevated NbN^- concentration within the first 20 nm of the surface layer. Subsequent removal of the surface shows earlier onset of high-field Q-slope [64].

While the exact cause of performance changes remains unclear, it has been established that they originate within the first nanometer of the oxide layer. Gradual removal through electro-polishing has shown a correlation between the onset of the high-field Q-slope and the depth of material removed, approaching typical values observed in electro-polished cavity high-field Q-slope onset at 100 mT.

7 Experimental Setup and Measurements

The cold test of a SC cavity aims to determine changes in its Q_0–E_a performance curve with each preparation step. In Chapter 5.5, the temperature dependence of the BCS surface has been introduced. All CH cavity tests have been conducted at 4 K, which is the chosen operation temperature for IAP SC CH cavities built and that are currently in development. The measurement process of the cavity performance is nearly identical for each test. Additional preparations might be necessary, as in the case of helium processing at 4 K. Cooldown and cavity conditioning are shown exemplary since cavity parameters such as frequency shift with temperature, and multipacting barriers are of concern during the cavity design phase and have to be separately validated for each cavity. This chapter chronologically guides through an entire cold test performed in the cryo-laboratory of IAP. Unique experimental setups and challenges of each cold test will be discussed together with the measurement results in Chapter 8.

7.1 Vacuum Preparation

Superconducting cavities require a high level of cleanliness on their inner surfaces. Hydrocarbons can reduce the work function of niobium and may be introduced when the vacuum pumps are not oil-free. A designated pump station for SC cavity operation is permanently installed to the mobile lid of the cryostat, as shown in Figure 7.1. The pump station consists of a membrane pre-pump, a turbomolecular pump, a high-vacuum pressure gauge, and a manometer that measures pressures down to a few mbar. All primary vacuum system components are DN CF parts, which use copper gaskets for the connection of all components. This minimizes leaking rates along the vacuum system and withstands operation in ultra-low temperature environments. Vacuum sections that are immersed into the cryo-bath use annealed copper gaskets, which are the most reliable sealing choice in this scenario. Chapter 7.3 will showcase the issue of cold leaks, which represent a major complication during the cooldown phase of a cold test and was a persistent issue post-HPR re-assembly.

Figure 7.1: Experimental setup with the 360 MHz CH cavity before insertion into the cryotank.

The cavity is connected to the lid using an aluminum mounting circle ring, where the cavity is held in place by four threaded rods and screw nuts. The mounting system, including adaptations for HPR treatment, was discussed in Chapter 6.1.2. The vacuum string is connected to an angle valve at the bottom part of the cavity. In the event particles accidentally enter the resonator through the vacuum line, they have a higher chance of falling onto the cavity floor, where electric fields are weak, reducing the chance of emitter activation.
The section from the pump station up to the angle valve of the cryo lid is under slight

overpressure with nitrogen, as a result of cavity ventilation in the prior cold test. The section from the lid angle valve to the cavity is exposed to air. After assembling the vacuum line to the cavity, the corrugated hoses are rinsed with clean nitrogen multiple times. The flow rate for pumping and ventilating needs to be low to minimize particle movement. For superconducting applications, the standard flow rate for ventilation is roughly 1 mbar/s, which was used for the vacuum system excluding the cavity. For pumping and ventilating the cavity, the same volume flow rate was used, resulting in a far lower rate than 1 mbar l/s to err on the side of safety.

Before the cavity is opened to the vacuum string, the entire string must undergo a leak test. The leak tester can be connected to a KF valve at the pump station. Since low leak rates of 10^{-12} to 10^{-10} mbar l/s are required, the line must be pumped to ultra-high vacuum with the turbomolecular pump. Within a suitable pressure range from 10^{-8} up to 10^{-6} mbar, the leak tester can adequately detect leak signal spikes. The leak tester is equipped with a mass spectrometer calibrated for ^{4}He. All connections are subjected to a weak helium gas jet from all sides. If a leak is detected, the flange can be further tightened and retested. Typically, a persistent leak stems from a damaged gasket or foreign bodies on the sealing surface and can often be resolved by replacing the gasket. During the cold test, the cavity is not pumped by the pumping station since the cryopump effect dominates and leads to cavity ventilation. To address this, an ion-getter pump is used while the lid's angle valve is closed, creating an enclosed system. The ion getter pump must be degassed under UHV using an installed heating unit until the pressure reaches a steady minimum, a process typically taking 8 to 10 h.

After degassing the ion-getter pump, the string is rinsed with nitrogen multiple times. The cavity is usually stored with a slight overpressure of nitrogen gas compared to the atmosphere. Consequently, the vacuum string requires a slight under pressure compared to the atmosphere to enable a gentle laminar flow from the cavity into the vacuum string when the angle valve is opened. The cavity is then slowly pumped to UHV and leak-tested. Finally, the angle valve at the cryostat lid is shut, and the ion-getter pump is used for the remaining preparation and cold test.

7.2 RF Workstation

High-quality factors of SC cavities result in very small frequency bands of a few Hertz. Strong coupling can broaden the acceptance band to a few hundred Hertz, which is still relatively narrow. Fluctuations within the helium bath can cause temperature and pressure shifts along the cavity, leading to changes in the resonance frequency within similar ranges. Operation of an SC cavity, therefore, necessitates an electronic system capable of fast adjustment of the RF signal to maintain cavity resonance. The core component for CW operation is the control system which was built at IAP. The control system operates within a fixed frequency range (300 – 400 MHz) and is designed for the operation of the 325 and 360 MHz cavities. A schematic overview of the entire RF system is presented in Figure 7.2.

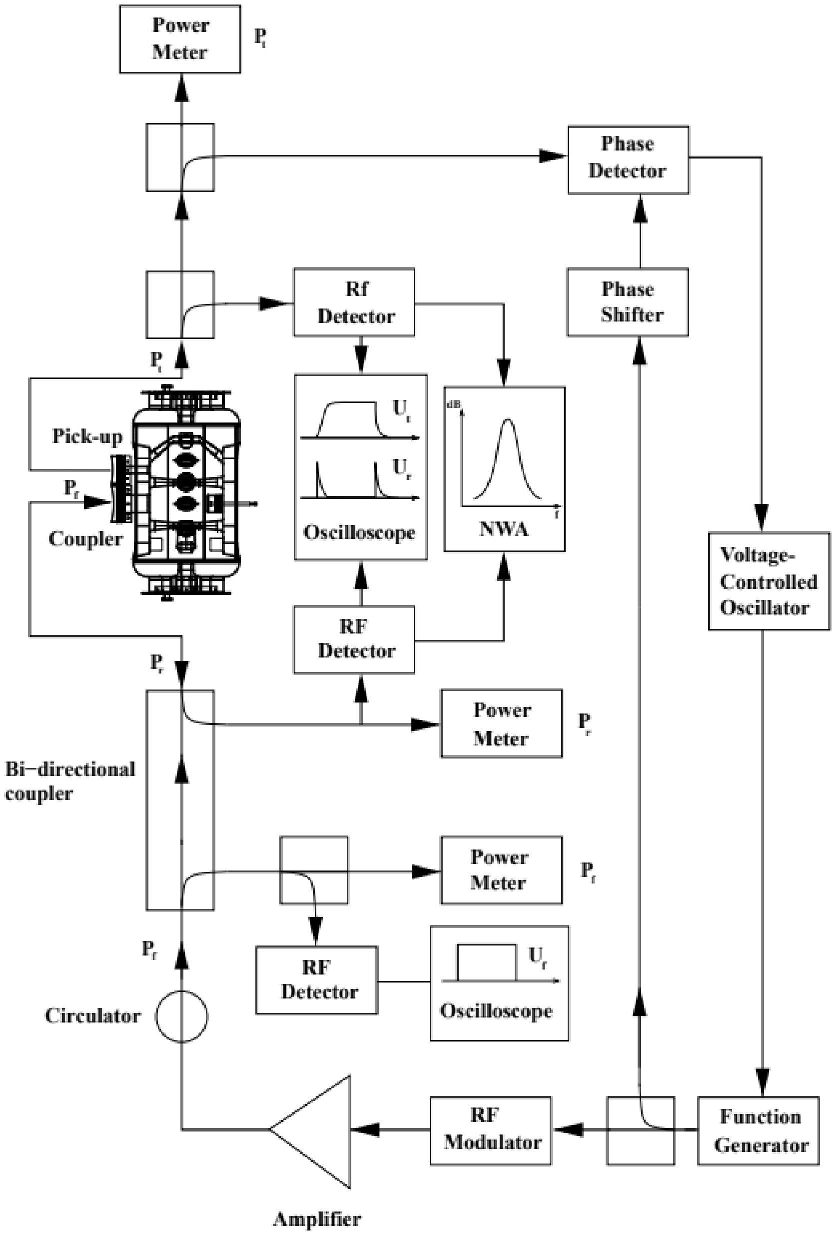

Figure 7.2: A schematic overview of the electronic system for low-level RF and performance measurements [36].

A function generator provides an RF wave at the desired frequency with a forward power of up to 10 mW. The control system features a phase and amplitude control unit that allows modification of the incoming RF signal from the function generator. The **F**requency **M**odulation (FM) of the function generator shifts the frequency proportionally to a DC voltage provided by a phase detector in the control system. This voltage is proportional to the phase shift between the function generator and the cavity signal. The function generator translates this voltage into a frequency shift of the function generator output signal using the **V**oltage **C**ontrolled **O**scillator method. Finally, the control system adjusts the output signal's amplitude relative to the amplitude of the cavity signal. Optionally, the control system offers a pulsed operation mode, providing rectangular pulse modulation with variable pulse and pause times, which is essential for low-level RF measurements. The signal is then amplified by an RF amplifier. For low-level measurements and RF conditioning of multipacting barriers, a 50 W amplifier suited for CW and pulsed operation with a broad frequency acceptance range is used. A circulator protects the amplifier from reflected power originating from the cavity coupler. A bi-directional coupler decouples a small fraction (-46 dB) of the forward and reflected power for analysis using an oscilloscope, network analyzer, and power meters. The transmitted cavity signal is split for analysis similar to the reflected power, with the addition of the control system's phase detector. Both Q_0 and E_a are calculated from the measured power meter values of P_f, P_r and P_t. The system is based on the principle that power meter sensors receive a well-defined fraction of the respective signal without distorting the original power levels P_f and P_r. The measured signal is then adjusted with each total damping value to obtain the real value present at the cavity. This necessitates careful and precise calibration of the entire RF system.

Part of the calibration process involves first verifying the functionality of all core RF components, namely the circulator, bi-directional coupler, splitters, cables, connections, and, of course, the cavity itself. Functionality is checked using a network analyzer at the operational frequency, where the components or circuit section's S-parameters S_{11} and S_{21} are of interest. S_{21} measures the corresponding dampening, while S_{11} represents the reflected signal. In healthy RF components, reflected signals should have values between -(26–35)dB. Significant reflection combined with higher-than-expected damping would indicate a broken part where the RF wave is partly reflected and dissipated.

Calibration of the three power meters is then performed via the final RF circuit used during the cold test. The circuit section's dampening is directly measured by the power meters themselves. A frequency generator provides a 0 dBm signal at the respective origin of the signal during the cold test. The power meters have the option to attenuate the measured signal. Calibration is considered complete when the power meter displays 0 dBm. An exception is given for the calibration of the forward power meter. The bi-directional coupler decouples a fraction of the signal, and the same procedure of P_r and P_t would yield the power level at the bi-directional coupler itself. Since the power level at the cavity is of interest, the circuit's dampening has to be separately measured and subtracted from the attenuation.

Before inserting the cavity into the cryo tank for cooldown preparation, the cavity's operability must be checked. The cavity coupler is designed to be strongly coupled for intrinsic quality factors of 10^9. For the 360 MHz cavity, the intrinsic quality factor at room temperature is 4300. This results in a reflection coefficient $r = \left(\frac{\beta-1}{\beta+1}\right) \approx 1$. The S_{21} cavity signal cannot be distinguished from the electric noise that occurs in the range of -(70 – 100)dB. A 4 W amplifier is typically sufficient to boost the signal above the electric noise.

7.3 Cryo System and Cooldown

The Physics Department of Goethe University possesses a cryoplant providing 4 K ^{4}He for SC applications of all faculties present on the Riedberg campus, including the cryolaboratory at IAP. The 3 m tall cryo tank has a capacity of 2200 l liquid helium. Given the physical limit of cryoplant efficiency, it's imperative to minimize all helium losses. In the context of SC cavities, a thermally, and mechanically excited helium bath will excite the microphonics spectrum of the cavity and make it inoperable. A schematic overview of the cryogenic circuit is shown in Figure 7.3.

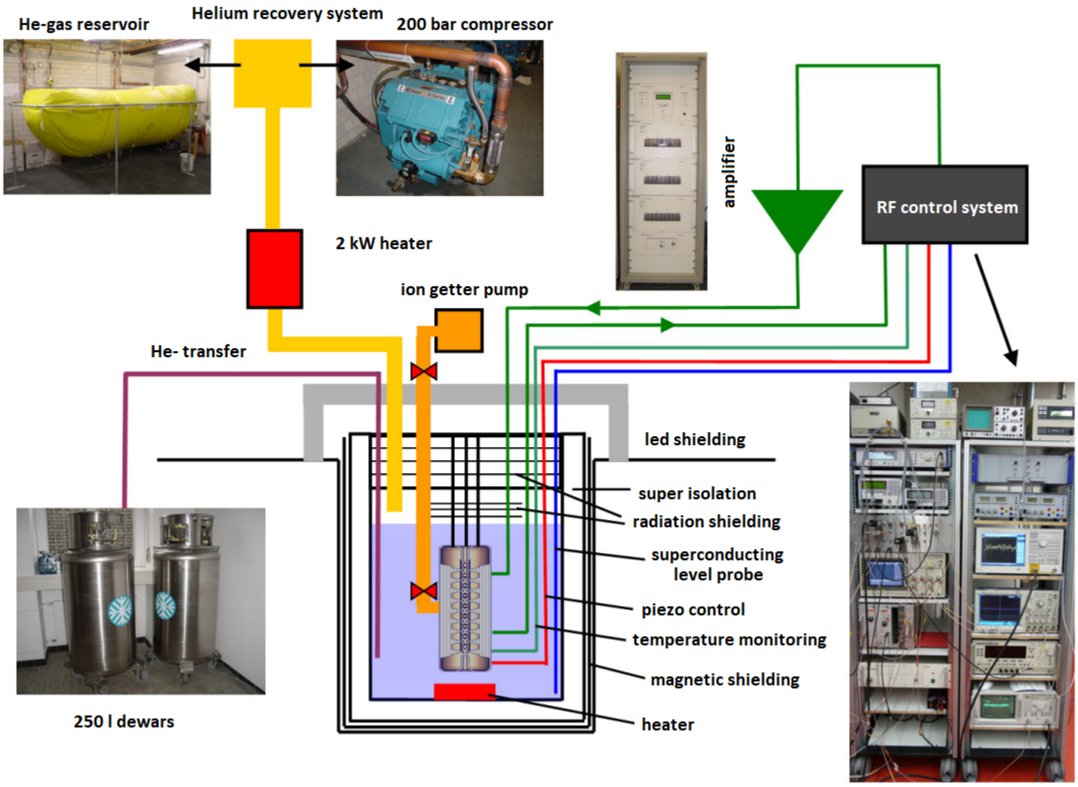

Figure 7.3: Circuit between cryo plant and laboratory at IAP, modified [24].

The cryobank and its supply components are thermally isolated by a vacuum and are pumped to UHV before every cooldown to 4 K. Liquid helium is transported from the plant to the laboratory in a 250 l dewar and is then connected to the tank via a cryo pipe and lifter. The lifter can be equipped with two different extensions. The long extension ends close to the tank floor and is used for cooldowns and filling during low helium levels.

As the helium level rises, the hydrostatic pressure increases and impedes further filling. Above 70 cm helium level, the extension is swapped for a shorter version, allowing for more efficient filling. Losses due to imperfect cryotank isolation and RF operation result in helium evaporation. This cold gas is directed through a warm water bath before entering the helium recovery pipeline, which leads back to the helium storage balloon. The warm helium gas is then cooled down and liquefied by the cryoplant.

The recovered helium must have a purity of at least 99% to reduce stress on the active filters before the cooling unit. During the cold test, the high purity of the recovered helium gas is automatically ensured. However, there are three sources from which impurities can be introduced into the system if not addressed. After insertion of the cavity, the cryo tank is filled with air. Subsequently, the tank is rinsed with high-purity helium gas, similar to the vacuum system using nitrogen. The tank is pumped to a few millibars and then filled up to atmospheric pressure. The vacuum sealing of the tank lid can be qualitatively checked by leaving the tank in the completely pumped state for 30 min up to one hour before filling the helium. If the pressure remains stable, the tank is cleared for cold operation.

The line leading from the water bath up to the angle valve of the helium recovery pipeline must be rinsed with helium if it was exposed to air during the cavity's removal after the cryo tank warm-up.

Before filling the tank, the connection pipe from the dewar to the lifter has to be rinsed. This is directly achieved by using the cold helium from the dewar until cold gas exits the pipe. Once the pipe is connected to the lifter, the filling procedure can be started. Besides the expelling of air in the tube, the pipe's cooldown allows for a short acceptance time for the tank and reduced heat influx, as seen in Figure 7.4.

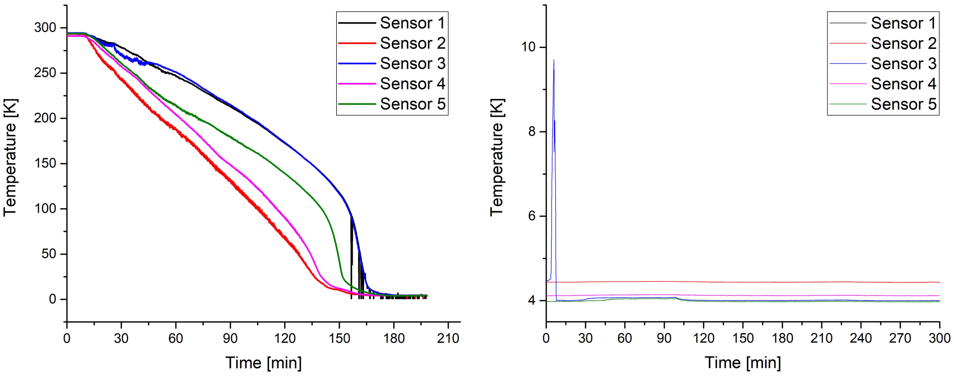

Figure 7.4: Exemplary cooldown and filling temperature curves. The cooldown is performed within 2 – 3 hours of total time, while requiring 1 h within the critical temperature range of (70 – 150)° C. Filling of the cold tank typically requires a waiting period of (10 – 20)min before the temperature inside the connection pipe and lifter reaches 4 K and liquid helium is transferred.

As the temperature decreases, both the cavity pressure and ion-getter pump current decrease. Unfortunately, a complication can arise during the cooldown process, where thermal deformation can lead to leakage. This is referred to as a "cold leak," and in most cases, it necessitates the termination of the test. Typically, the ion-getter pump current slowly and continuously increases, followed by a delayed increase in cavity pressure. Small leakages are sometimes observed to close up within 1 to 2 minutes, most likely due to temporary temperature gradients at a flange. A persistent cold leak will close up during warm-up to room temperature and, in most cases, exhibit similar leak rates at room temperature as before the cooldown. This effect was observed multiple times during the experimental series in this work, and a persistent case will be discussed in the HPR Section 8.5 of the measurement results.

7.4 RF Conditioning

When the cavity is successfully cooled down and fully immersed in liquid helium, the processing of multipacting barriers begins and is referred to as RF conditioning. Adsorbents on the cavity surface increase the SEC coefficient, leading to increased multipacting currents that limit the cavity at the associated field level. An increase beyond this field level results in the complete absorption of excess RF power by the electron current, leading to the characteristic multipacting plateau in the transmitted signal, shown in Figure 7.5.

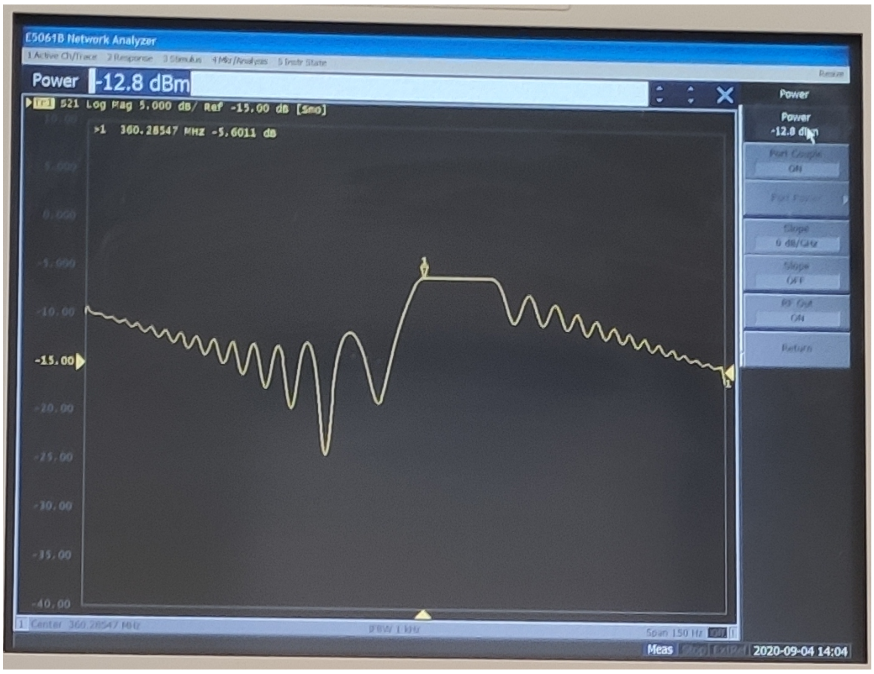

Figure 7.5: S_{21}-signal on the network analyzer shows multipacting barriers during the conditioning process.

RF conditioning processes degas surface adsorbents due to the impact of the electron current. The local SEC decreases until the current is no longer self-sustaining. The exponential nature of this resonant current can lead to damage to the cavity surface when not handled correctly. The protocol differs for normal and superconducting cavities. While normal conducting copper surfaces are often CW RF conditioned at a given barrier field level, niobium surfaces require a more delicate approach. Protocols consist of pulsed power processing to limit the evolution time of the electron current. Since SC cavities have a high transient response time compared to normal conducting cavities, field levels will naturally keep trying to increase while multipacting has already set in. This is analogous to a further increase of CW RF power beyond the barrier level in the normal conducting case. The solution to this problem is to keep the pulse duration shorter than the time constant $\tau_L = Q_\mathrm{L}/\omega$. This can be done using a frequency generator and signal modulation, which is often employed by other international laboratories.
A different approach is to utilize a network analyzer as the signal source. Here, the signal is generated by sweeping over a defined frequency band (span) at a set repetition frequency (IF bandwidth). The operator can adjust three parameters of the cavity input signal, namely forward power, frequency bandwidth, and frequency sweep speed. The conditioning starts at a low power level with a high span and high sweep speed. Typical values for this are a few milliwatts with a span of 1 kHz and an IF bandwidth of 3 kHz. This results in three sweeps per second over the defined frequency band. Considering the 3dB range of the 360 MHz cavity at $Q_\mathrm{L} = 1.5 \times 10^8$, which is $\Delta f_{3dB} = 2.4\,\mathrm{Hz}$, this is roughly estimated by a duty factor 0.0024 with and a pulse length of 0.8 ms. In the case of strong coupling, the cavity requires multiple $\tau_L = 60\,\mathrm{ms}$ to reach its steady-state field level, as shown in Figure 2.5. From this, we see that the cavity is excited by such short bursts that the field ramping behavior of the cavity is largely suppressed.
Over the course of RF conditioning RF power, span, and IF bandwidth are adjusted to process the MP barrier spectrum. A barrier is processed when a given plateau in S_{21} signal vanishes and the field level exceeds the prior limitation.

7.5 Low Level and Q-E Measurement

Once the cavity is fully RF conditioned, it is safe to apply pulse lengths that reach steady-state low field levels. Up to this point, essential cavity parameters could not be measured. The pulsed RF signal response can now be used to verify RF parameters at low field levels, as shown in Chapter 2.6. The goal is to quantify the intrinsic quality factor at its highest value. For extremely low field levels ($P_\mathrm{c} < 1\,\mathrm{mW}$) the initial upward Q-slope could be observed during the first cold test. This was due to the very strong overcoupling of $\beta \approx 44$, where such low power was transmitted into the cavity at a forward power of $P_f = 150\,\mathrm{mW}$.
With a reasonable coupling strength of 3 to 8, low-level measurements are performed at pulse powers within 50 to 150 mW. The cavity response is recorded with an oscilloscope and shows the characteristic 'fish-shaped' signal of strongly coupled cavities.

The oscilloscope measures a signal's voltage and allows direct calculation of β from the peak heights using Equation 2.116. Measurement of Q_L is performed by determining τ_L of the transmitted power oscilloscope signal. The exponential decline is proportional to $\exp\left(-\frac{t}{2\tau_L}\right)$, and the corresponding time period Δt where the signal drops to $\frac{1}{e}$ is obtained as $\Delta t = 2\tau_L$.

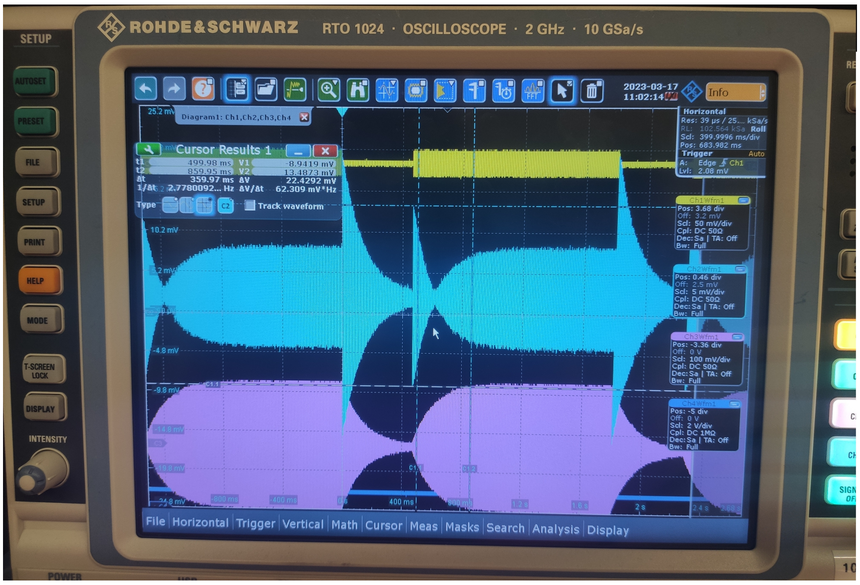

```
Cursor Results 1
t1     499.98 ms   V1          -8.9419 mV
t2     859.95 ms   V2          13.4873 mV
Δt     359.97 ms   ΔV          22.4292 mV
1/Δt   2.7780092... Hz   ΔV/Δt   62.309 mV*Hz
```

```
Horizontal
Res: 39 µs / 25.... kSa/s
RL:  102.564 kSa  Roll
Scl: 399.9996 ms/div
Pos: 683.982 ms
Trigger          Auto
A:   Edge  Ch1
Lvl: 2.08 mV
```

```
Ch1Wfm1
Pos: 3.68 div
Off: 3.2 mV
Scl: 50 mV/div
Cpl: DC 50Ω
Dec:Sa | TA: Off
Bw: Full
```

```
Ch2Wfm1
Pos: 0.46 div
Off: 2.5 mV
Scl: 5 mV/div
Cpl: DC 50Ω
Dec:Sa | TA: Off
Bw: Full
```

```
Ch3Wfm1
Pos: -3.36 div
Off: 0 V
Scl: 100 mV/div
Cpl: DC 50Ω
Dec:Sa | TA: Off
Bw: Full
```

```
Ch4Wfm1
Pos: -5 div
Off: 0 V
Scl: 2 V/div
Cpl: DC 1MΩ
Dec:Sa | TA: Off
Bw: Full
```

Figure 7.6: The characteristic "fish"-shaped reflection signal (blue) during pulsed operation of a strongly coupled cavity is used to calculate the coupling strength β from the switch-on to switch-off peak ratio. The exponential decline of the transmitted power (purple) is used to determine the loaded quality factor.

The loaded quality factor is then calculated as $Q_\mathrm{L} = \pi f \Delta t$. The intrinsic quality factor is then calculated with $Q_0 = Q_\mathrm{L}(1+\beta)$ for the applied forward power used. Since the calculation of β is based on a voltage ratio and Q_L is determined by the $1/e$-method, the low-level measurement results are independent of RF component's signal dampening and cannot be distorted.

The parameters Q_0 and E_a in the performance plot are calculated for every RF power triplet (P_f,P_r,P_t) and result in the 2-tuple (E_a, Q_0). First, we derive the function for $E_a = E_a(P_f, P_r, P_\mathrm{t})$. For low field levels, the cavity losses are caused by the BCS and residual resistance, and the cavity voltage U_a is given by:

$$U_a = B\sqrt{P_\mathrm{t}} \tag{7.1}$$

B is a constant that depends on cable calibration and the coupling strength β_t of the pickup. The acceleration voltage is also given by the shunt impedance and cavity losses:

$$U_a = \sqrt{R_a P_\mathrm{c}} = B\sqrt{P_\mathrm{t}} \tag{7.2}$$

Now, B can be calculated from low field power and shunt impedance values:

$$B = \sqrt{\frac{R_a^{low} P_c^{low}}{P_t^{low}}} = \sqrt{\left(\frac{R_a}{Q_0}\right) Q_0^{low} \frac{(P_f^{low} - P_r^{low} - P_t^{low})}{P_t^{low}}} \tag{7.3}$$

We recall that the (R/Q) value is a geometric property of the cavity and is independent of field level, and is known from CST RF simulation, which allows calculating Q_0^{low} from $(R_a^{sim}/Q_0^{sim}) = (R_a^{low}/Q_0^{low})$. With $P_c = P_f - P_r - P_t$ as part of B, precise calibration is necessary. Since the relation $U_a = B\sqrt{P_t}$ is field independent, B can be used to calculate E_a and Q_0 at high field levels:

$$E_a^{high} = B\frac{\sqrt{P_t^{high}}}{l} \tag{7.4}$$

For calculation of Q_0^{high} we start from:

$$R_a^{high} = \frac{U_a^{2,high}}{P_c^{high}} = \left(\frac{R_a^{sim}}{Q_0^{sim}}\right) Q_0^{high} \Rightarrow Q_0^{high} = \frac{U_a^{2,high}}{\left(\frac{R_a^{sim}}{Q_0^{sim}}\right) P_c^{high}} = \frac{B^2 P_t^{high}}{\left(\frac{R_a^{sim}}{Q_0^{sim}}\right) P_c^{high}}$$

Inserting B yields the relation between Q_0^{high} and Q_0^{low}:

$$Q_0^{high} = Q_0^{low} \left(\frac{P_f^{low} - P_r^{low} - P_t^{low}}{P_f^{high} - P_r^{high} - P_t^{high}}\right)\left(\frac{P_t^{high}}{P_t^{low}}\right) \tag{7.5}$$

With increasing cavity losses, the coupling strength β of SC cavities does not remain constant. During the measurement of the power triplets, the control system requires phase shift adjustments as the power increases. The change in phase shift increases with increasing Q-slope. Suppose the control system does not maintain the cavity at the maximum field level. In that case, the results of E_a and Q_0 remain accurate, but the coupling strength β increases and becomes unrelated to the cavity's ideal performance.

8 Measurement and Results

This chapter outlines the cavity performance measurements at each stage of this work. The main effort was put into the 360 MHz CH cavity. First, a recap of past performance and RF parameters will be shown and then compared to the state after tuning tests, 11 years of storage, and a suspected ventilation accident during the storage period. The cavity was then made operational by coupler redesign and baseline performance was recorded. A series of preparation methods were then applied to the cavity with a performance test in between each treatment.

8.1 2007 Performance

The measurement results of 2007 are used as a reference for past cavity performance. Low-level measurement resulted in the RF parameters displayed in Table 8.1.

τ_L	Q_L	β	Q_0	R_s	R_0
54.5 ms	1.23×10^8	4.54	6.8×10^8	82 nΩ	29 nΩ

Table 8.1: RF parameter results from 2007 [24].

The surface resistance from external magnetic field is $R_{s,ext} = 4\,\mathrm{n\Omega}$, and the BCS resistance is $R_{s,BCS} = 49\,\mathrm{n\Omega}$, used to determine the residual resistance, are constant values across all tests. The Q-E plot in Figure 8.1 shows the past performance development of the 360 MHz.

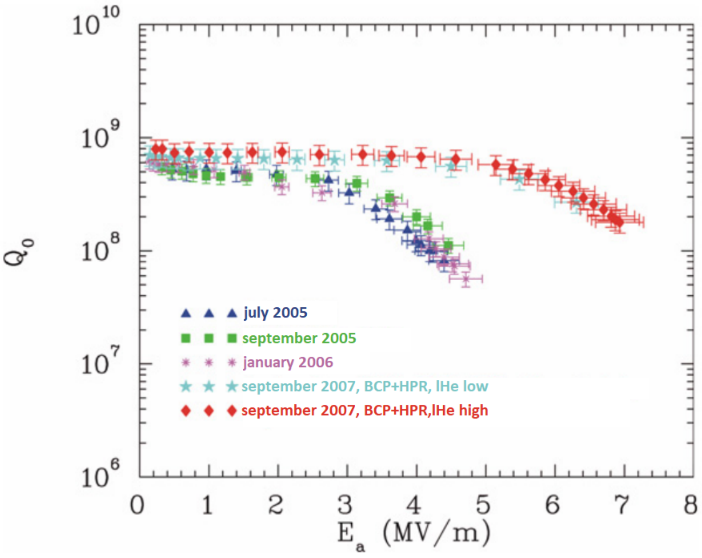

Figure 8.1: Q-E results from past performance measurements, modified [24].

The decrease in Q_0 with E_a stems from an increase in total losses. At low field levels, the ohmic losses mainly stem from residual and BCS resistance. Within low field levels the BCS resistance is assumed to be constant and the ohmic losses can be extrapolated with the quadratic relation:

$$P_{\mathrm{c}}^{ohmic} = \frac{U_a^2}{R_a^{low}} = \frac{(E_a \cdot l)^2}{\left(\left(\frac{R}{Q}\right) Q_0^{low}\right)} \tag{8.1}$$

The difference between the total losses measured and the interpolated losses at high fields are given from additional mechanisms like BCS resistance increase, magnetic losses, field emission, etc. Figure 8.2 shows the total cavity losses and the extrapolated ohmic losses.

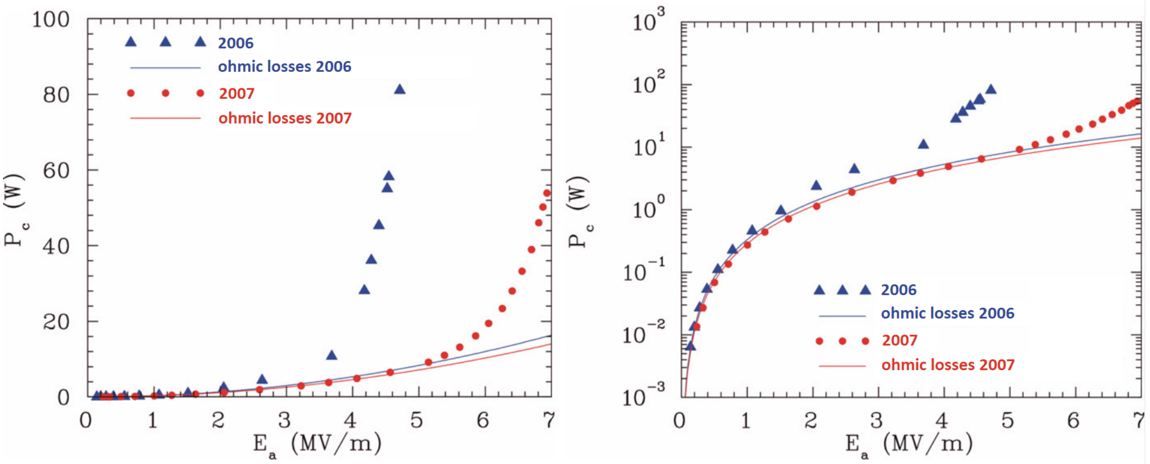

Figure 8.2: Losses from 2006 and 2007 measurements, in linear and logarithmic scale, modified [24].

In Chapter 5.6.2 the Fowler-Nordheim equation and the enhancement factor β_{FN} are discussed. The results can be formed into the tuple $(1/E_p, \ln\left(\frac{I}{E_p^{2.5}}\right))$, where a linear relation will be seen for measurement points with active field emission. The slope m is directly linked to the enhancement factor via,

$$\beta_{FN} = \frac{B_{FN\phi^{3/2}}}{m}$$

where $B_{FN} = 6.83 \cdot 10^3$ and $\phi = 4.4\,\mathrm{eV}$.

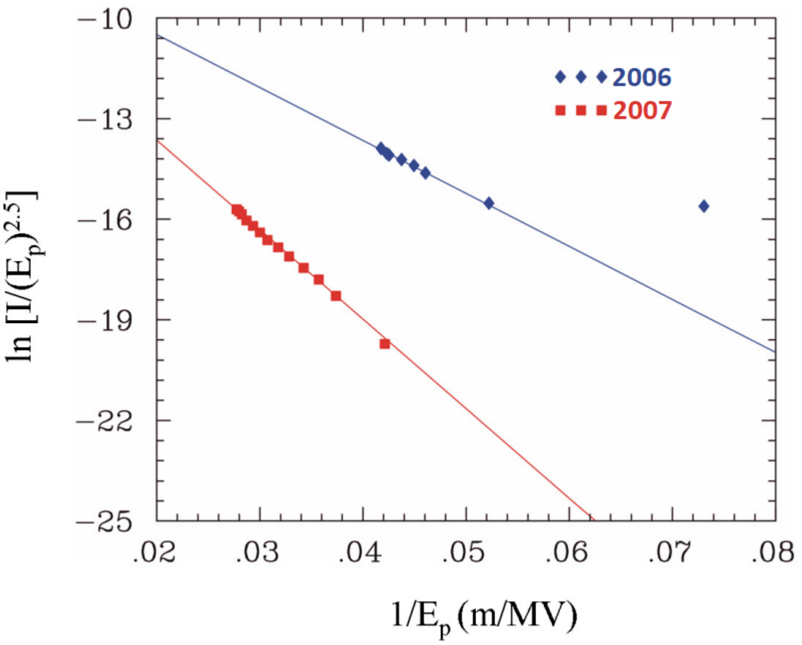

Figure 8.3: Fowler-Nordheim plot from 2007 showed an enhancement factor of $\beta_{FN} = 240$, modified [24].

8.2 State after Storage

The 360 MHz cavity was stored for 11 years before the start of this work. A cold test was performed to determine the cavity performance state. Vacuum preparation showed no problems with leaks and the cavity was cooled down to 4 K without the onset of cold leaks. RF conditioning of the cavity required a total amount of 2.5 weeks until multipacting barriers were processed. Low-level measurement results are shown in table 8.2.

τ_L	Q_L	β	Q_0	R_s	R_0
6.05 ms	$1.37 \cdot 10^7$	40 ± 10	$(5.61 \pm 1.37) \cdot 10^8$	$(106 \pm 26)\mathrm{n}\Omega$	$(53 \pm 26)\mathrm{n}\Omega$

Table 8.2: RF parameter results from the first cold test after 11 years of cavity storage time.

The exponential decay time $\tau_L = 6.05\,\mathrm{ms}$ would require very strong coupling of $\beta = 44$ with regards to the prior intrinsic quality factor of 2007 with $Q_0^{2007} = 6.8 \cdot 10^8$. Calculation of β via the reflected peak signal ratio ranged within 30 − 50. The error of the β measurement increases for increases with its value. The problem is shown by plotting the underlying formulas, shown in Figure 8.4.

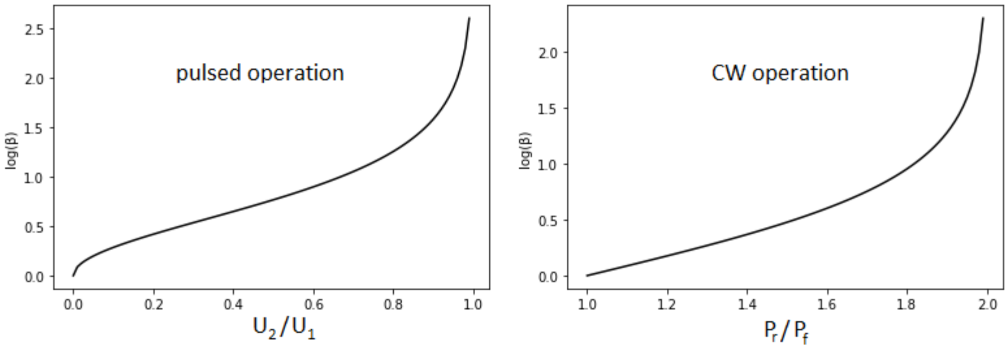

Figure 8.4: On the left: Log-Plot of $\beta^{osci} = \frac{1}{2\frac{U_1}{U_2}-1}$ for the peak voltage ratio U_2/U_1 during pulsed operation. On the right: Log-Plot of $\beta^{power} = \frac{1\pm\sqrt{P_r/P_f}}{1\mp\sqrt{P_r/P_f}}$ for the power ratio P_r/P_f, during CW operation.

Small relative errors in both peak voltages lead to a high absolute error for coupling strengths $\beta > 25$ where the function slope strongly increases. A measurement series within the low field field of voltage peak ratios resulted in $\langle\beta^{osci}\rangle = 41 \pm 8$. Performance curve measurement also allows to calculate β from power meter data. The beta value also varies strongly for small power value deviations for $\beta > 50$, see figure 8.4. The low level Q-E data resulted in $\langle\beta^{power}\rangle = 37.56 \pm 3.80$ and therefore $\langle Q_0^{power}\rangle = (5.28 \pm 0.52) \cdot 10^8$. The cavity performance is shown in Figure 8.5.

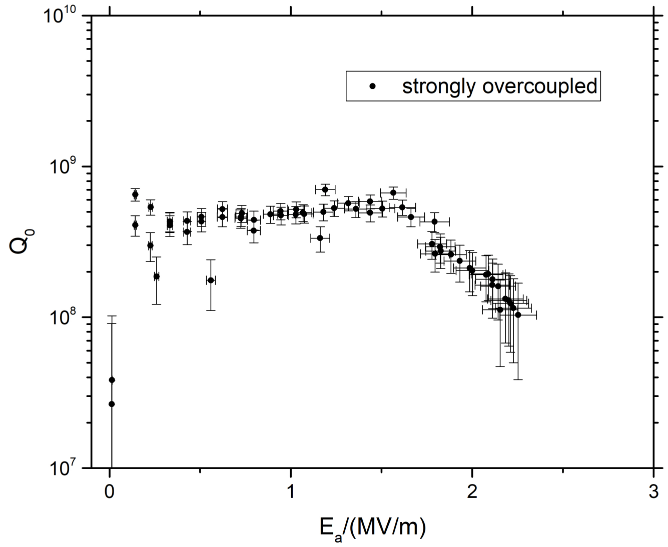

Figure 8.5: Performance curve after 11 years of storage time. The strong overcoupling led to noise within the Q-E plot.

Maximum gradient was found to be $E_{a,max} = 2.3\,\mathrm{MV/m}$, the cavity showed strong onset of field emission at a low field level of $E_a = 1.8\,\mathrm{MV/m}$ and was limited by field emission induced quenches.

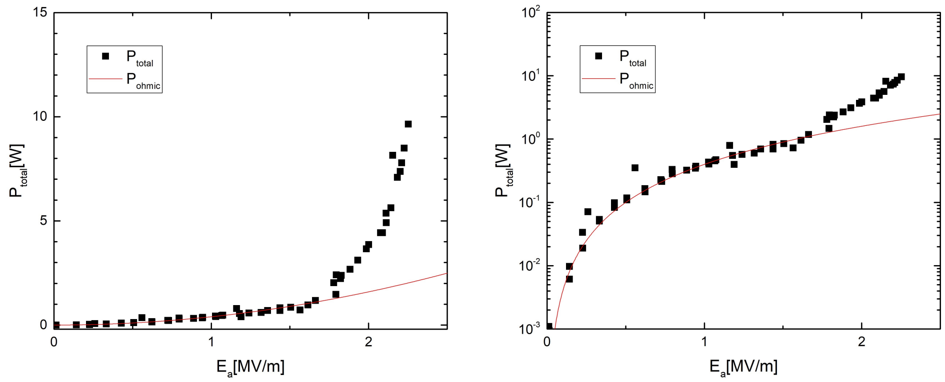

Figure 8.6: Additional losses are observed at $E_a = 1.8\,\mathrm{MV/m}$ and coincide with an observed onset of X-ray radiation.

The effect is also apparent in the loss plots, see Figure 8.6, and quadratic fits for low-field level values. The logarithmic plot shows the influence of outlier points, resulting in a slightly stronger upward slope of the fit than one could expect. This has led to an underestimation of the electron current I_{FN} and the amplifying coefficient β_{FN} shown in Figure 8.7.

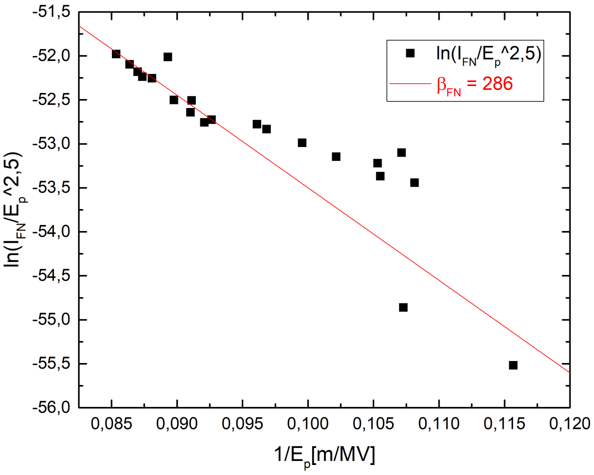

Figure 8.7: Fowler-Nordheim plot of the first cold test after storage.

The Fowler Nordheim-coefficient $\beta_{FN} = 286$ appears elevated compared to the measurement of 2007 with $\beta_{FN} = 240$.
Overall, the measurement contains substantial noise and is visibly distorted due to the overly strong coupling. The cavity was examined in the clean room at IAP after warm-up and the installed coupler was dismounted and further analyzed in the RF laboratory and a redesign of the coupler was performed, as described in Chapter 2.5.

8.3 Baseline New Coupler

After coupler assembly in the clean room at IAP, the cavity was successfully leak tested, and cooldown was performed. A persistent cold leak formed and required a warm-up to room temperature. An increased leak rate was found at the connection between the vacuum pipe and the angle valve at the cavity. The connection was tightened and the leak rate decreased below 10^{-10} mBar/s. Cooldown to 4 K was successful and RF conditioning performed. Low-level measurements showed the RF parameter shown in table 8.3.

τ_L	Q_L	β	Q_0	R_s	R_0
63 ms	$1.43 \cdot 10^8$	2.49	$4.98 \cdot 10^8$	112 nΩ	59 nΩ

Table 8.3: RF parameter results from with new coupler.

The quality factor of the new coupler was measured at room temperature inside the clean room and resulted in $Q_{\mathrm{e}}^{RT} = 2.02 \cdot 10^8$. Calculating the couplers quality factor from RF parameter at 4 K results in $Q_{\mathrm{e}}^{4K} = 2.01 \cdot 10^8$ and is in agreement with prior room temperature measurement. The intrinsic quality factor was identified as $Q_0 = 4.98 \cdot 10^8$ at low field level and is well within the measured range of the prior "strongly overcoupled" cold test.

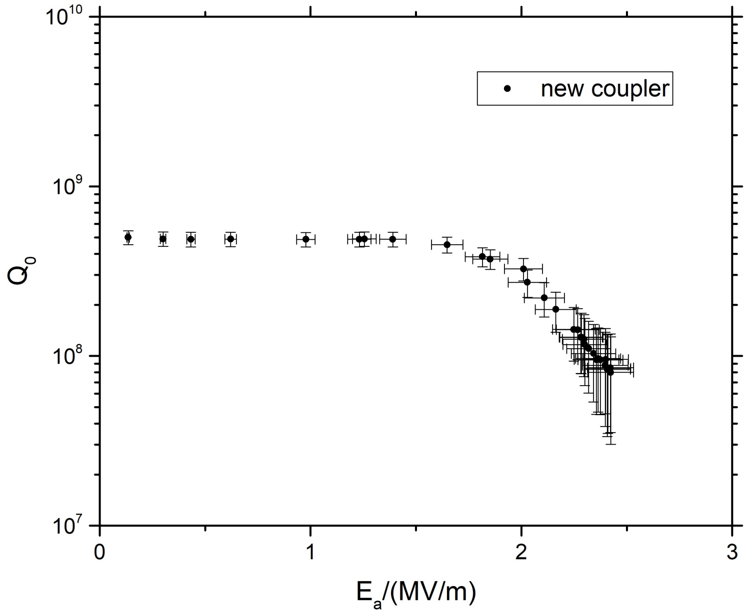

Figure 8.8: Performance curve after the installment of the new coupler.

Noise reduction due to the decreased coupling strength is visible in the performance curve in Figure 8.8 in comparison to Figure 8.5. The maximum electric field resulted in $E_a = 2.45\,\mathrm{MV/m}$. With this clear baseline performance, the effect of subsequent treatments is now quantifiable. The field emission Q-slope, with an assigned onset at $E_a = 1.8\,\mathrm{MV/m}$, is now well defined.

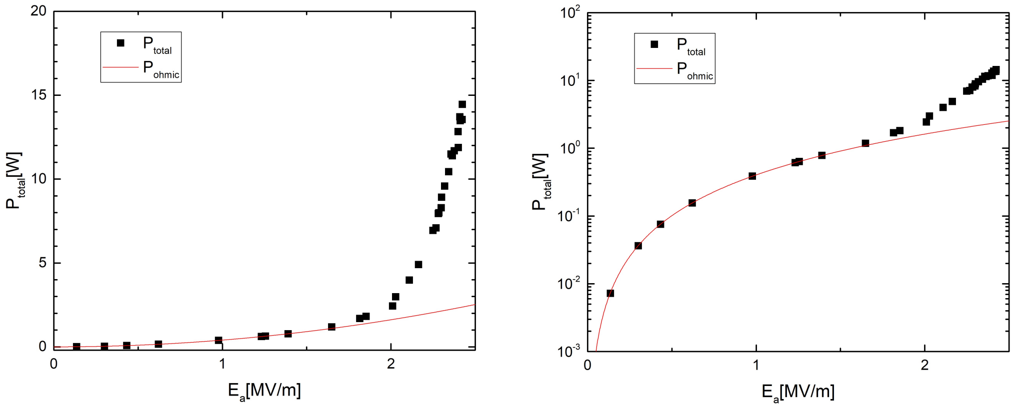

Figure 8.9: Total losses vs interpolated ohmic losses, at $E_a = 1.8\,\mathrm{MV/m}$ additional loss mechanisms set in.

The total cavity losses in Figure 8.9 differ from the interpolated ohmic losses slightly before bremsstrahlung could be detected via scintillator. Since the X-ray radiation is measured on top of the cryo tank lid, a threshold must be met before bremsstrahlung can be detected through the infrastructure. The ohmic losses are slightly lower than previously determined, which was expected.

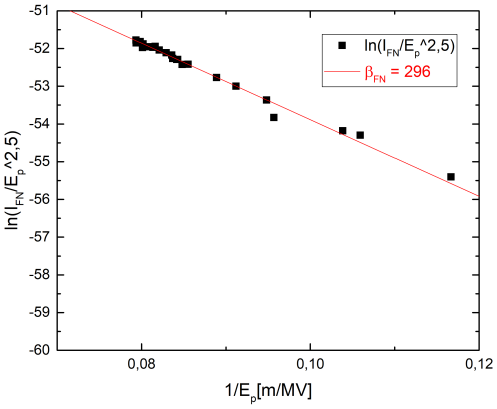

Figure 8.10: Fowler-Nordheim plot with replaced coupler.

The non-ohmic losses $P_{nonohmic} = P_{total} - P_{ohmic}$ increased due to greater accuracy of the fit and results in an amplification factor of $\beta_{FN} = 296$, shown in Figure 8.10. The cavity has previously shown greater performance with higher β_{FN}, as shown in table 8.4.

test	Q_0	R_0	β_{FN}	$E_{a,max}$
2006	$5.7 \cdot 10^8$	$49\,\mathrm{n\Omega}$	400	$4.3\,\mathrm{MV/m}$
2007	$6.8 \cdot 10^8$	$29\,\mathrm{n\Omega}$	240	$7.0\,\mathrm{MV/m}$
baseline	$4.98 \cdot 10^8$	$59\,\mathrm{n\Omega}$	296	$2.45\,\mathrm{MV/m}$

Table 8.4: RF parameter comparison of 2006, 2007 and baseline measurement after storage.

The rise in residual resistance hints towards accidental ventilation with air outside of a clean room setting. Ventilation with air is used in the study of performance recovery protocols and observe similar drops in Q-value and maximum electric field. Recovery protocols with different preparation methods exist and are further researched. A standard procedure is given by a combination of low-temperature bake and HPR which can be repeated multiple times. As a last resort a chemical etch is used to 'reset' the inner surface. The reason behind the Q-drop could not be traced due to the prolonged time to the last activity with the cavity. The decision was made, to first bake and then to HPR the cavity. The base expectation was to recover prior cavity performance from 2007. In the case this could not be achieved, a BCP of the cavity would have been performed.

8.4 Low Temperature Bake

The cavity was brought back to the cryo laboratory after heat treatment, leak tested, and cooled down without any complications. During RF conditioning, the multipacting barrier density was reduced and each barrier processed faster compared to the prior tests. The total RF conditioning phase took only 3 days compared to the baseline measurement conditioning phase of $10-14$ days. The cavity UHV decreased by a magnitude from heat treatment under room temperature, from $10^{-8}\,\mathrm{mBar}$ to $10^{-9}\,\mathrm{mBar}$ with the more powerful pump station at the experimental hall, see Figure 8.11.

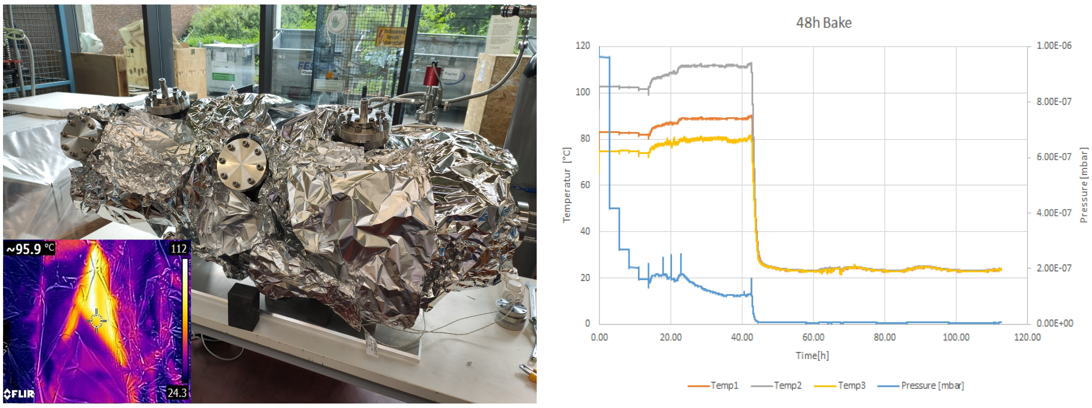

Figure 8.11: The cavity was baked at 110° C for 48 hours. The installed temperature probes did not accurately measure the total temperature present in the cavity and can only be used to show the qualitative change. The peak temperature was determined with a heat camera.

The clear decrease in multipacting suggests that the improvement of the UHV is at least partially due to the reduction of surface hydrocarbons. The mass spectrometer measurements also showed a reduction in hydrogen, which is a contributor to residual resistance. Low-level measurements showed changes in the RF parameters listed in Table 8.5.

τ_L	Q_L	β	Q_0	R_s	R_0
70.5 ms	$1.60 \cdot 10^8$	2.98	$6.35 \cdot 10^8$	88 nΩ	35 nΩ

Table 8.5: RF parameter results after 120°C bake.

The low level results showed an increase to $\tau_L^{baseline} = 70.5\,\mathrm{ms}$ from $\tau_L^{bake} = 63\,\mathrm{ms}$ and therefore a loaded quality factor increase from $Q_\mathrm{L}^{baseline} = 1.43 \cdot 10^8$ to $Q_\mathrm{L}^{bake} = 1.60 \cdot 10^8$. The intrinsic quality factor of the cavity increased by 27.5% to $Q_0^{bake} = 6.35 \cdot 10^8$.

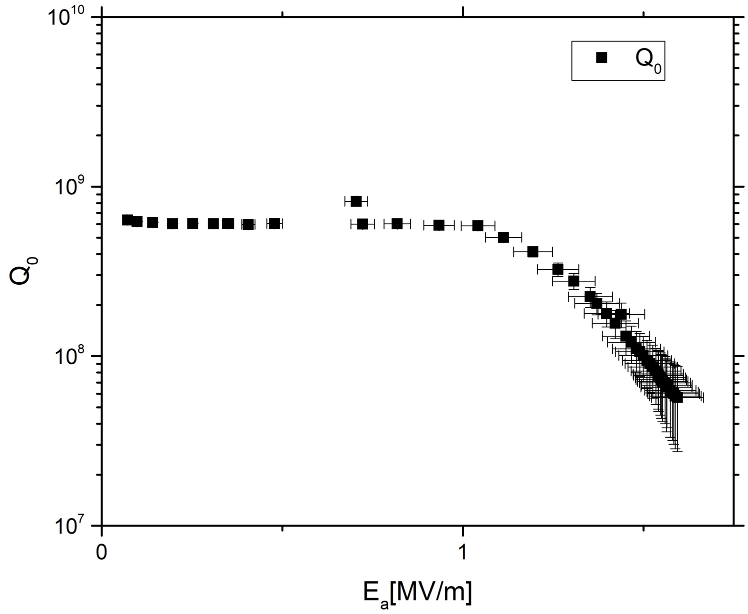

Figure 8.12: Performance curve after 120°C bake.

The maximum electric field did further reduce down to $E_a = 1.6\,\mathrm{MV/m}$ with a field emission onset at $E_a = 1.1\,\mathrm{MV/m}$. The worsening of field emission, seen by the Q-slope in Figure 8.12 and the displayed losses in Figure 8.13, can have multiple reasons. For once, emitters were already present in the cavity before heat treatment. Cavity transportation and rearrangement can displace the particles to new locations with higher relative electric surface fields, activating the emitters at lower E_a levels. Another possibility is given by the introduction of further particles during the heat treatment vacuum preparation. The pump station in the experimental hall is also exclusively reserved for SC cavities and should ideally not be contaminated. However, since the assembly of the vacuum string to the cavity of prior and this test was performed in the experimental hall, particles inside the corrugated hose and pump station can not be ruled out.

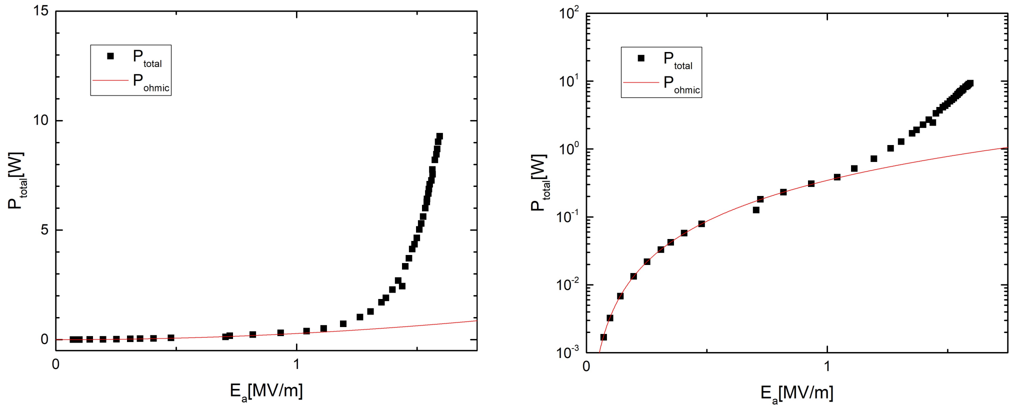

Figure 8.13: Total losses vs interpolated ohmic losses, at $E_a = 1.8\,\mathrm{MV/m}$ additional loss mechanisms set in.

While the drop in electric field is a concern, it is more likely that other sources than the bake are responsible for this effect. The cavity gas spectrum was analyzed via mass spectrometer before and after baking.

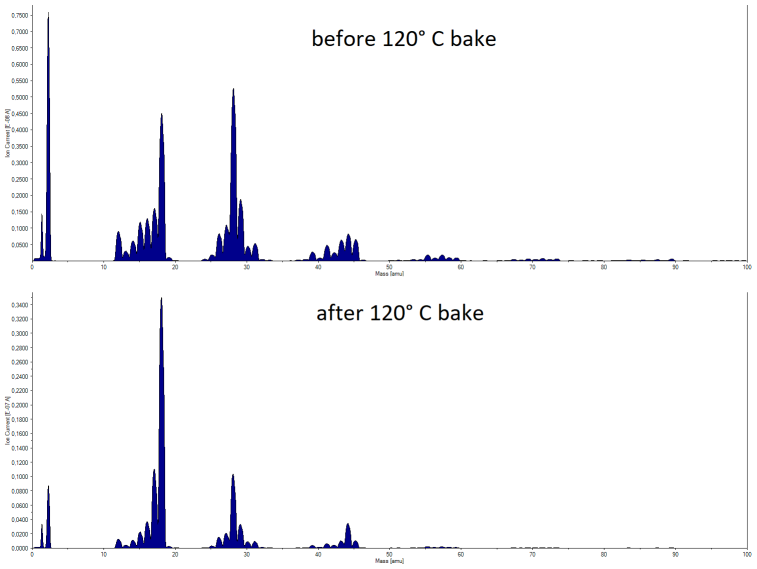

Figure 8.14: The hydrogen current dropped by 20% when the cavity was measured after the 120° bake. The $M = 18$ peak is due to H_2O and increased by a factor of 5 and $M = 28$ peak is most likely due to N_2 and increased by a factor of 2.

The spectrum comparison shows a decrease in H_2 and of compounds with $M > 50$

which include a variety of hydrocarbons, which are found to decrease the work function of niobium and increase residual resistance. This residual gas analysis data is consistent with the observed Q increase at low levels.

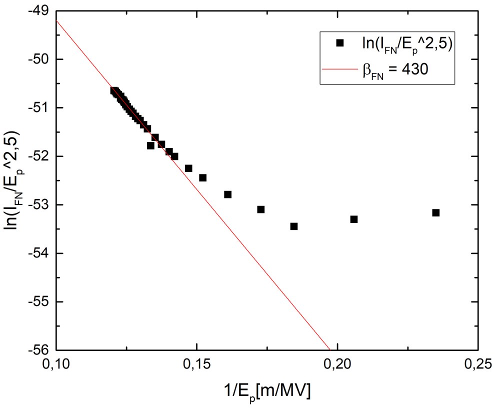

Figure 8.15: Fowler-Nordheim plot after 120°C bake.

The amplifying coefficient further increased from $\beta_{FN} = 296$ to $\beta_{FN} = 430$, see Figure 8.15, and hardens the assumption of emitter displacement from transportation and/or insertion of particles through the vacuum system inside the experimental hall. Under these estimated conditions, an HPR of the cavity is expected to greatly improve the maximum gradient of the cavity. The HPR preparation and application at HIM are discussed in Chapter 6.1.2 up to Chapter 6.1.4.

8.5 HPR

The cavity was transported from HIM to the cryo laboratory at IAP Frankfurt. The leak rate at HIM could not be reduced below 10^{-6} mBar/s but was sufficient for transportation. Extensive leak tests and flange adjustments could not improve the leak rate to levels where a cold test could be performed. The cavity was then cleaned and placed inside the clean room for replacement of all gaskets. This harbors the risk of cavity contamination, effectively nullifying the HPR treatment effect. To reduce the chance of the introduction of new particles inside the cavity, the execution of this process was carefully planned. As the first step, all critical surfaces like the table and flow box slats were cleaned with clean room wipes and isopropanol. Gaskets were sequentially replaced under the condition, that the flanges were positioned in a downward angle of roughly 45°. New gaskets and disassembled components were placed on opposite sites of the clean room table. Flanges, screws, nuts, and washers were cleaned with lint-free, microfiber cleanroom wipes and ethanol. Assembly of each flange was performed with fresh

gloves and repeatedly cleaned tools. After completion, the cavity was then successfully leak-tested in the cryo laboratory.
A cold leak formed at a relatively high temperature of 170 K and warm-up with subsequent leak test performed. All flanges were tightened back to the previous torque value. One of the 100 mm-"DESY" blank flange showed an increased leak rate but could be leak-proofed again. This flange formed a cold leak two more times, at 70 K and 5 K. The fourth cooldown was successful and RF conditioning was performed for a total of 8 days. Low-level measurements resulted in RF parameter changes illustrated in Figure 8.6.

τ_L	Q_L	β	Q_0	R_s	R_0
72 ms	$1.63 \cdot 10^8$	3.13	$6.73 \cdot 10^8$	84 nΩ	30 nΩ

Table 8.6: RF parameter results after HPR.

Special attention was given to the assembly of the coupler concerning its alignment with the cavity. From $Q_0 = 6.73 \cdot 10^8$ and $Q_\mathrm{L} = 1.63 \cdot 10^8$ the coupler's quality factor results in $Q_\mathrm{e} = 2.15 \cdot 10^8$ similar to the quality factor after heat treatment.
The intrinsic quality factor of the cavity increased slightly by 6% to $Q_0 = 6.73 \cdot 10^8$. The increase might stem from a further decrease in surface hydrocarbons. The Q-E performance is plotted in Figure 8.16.

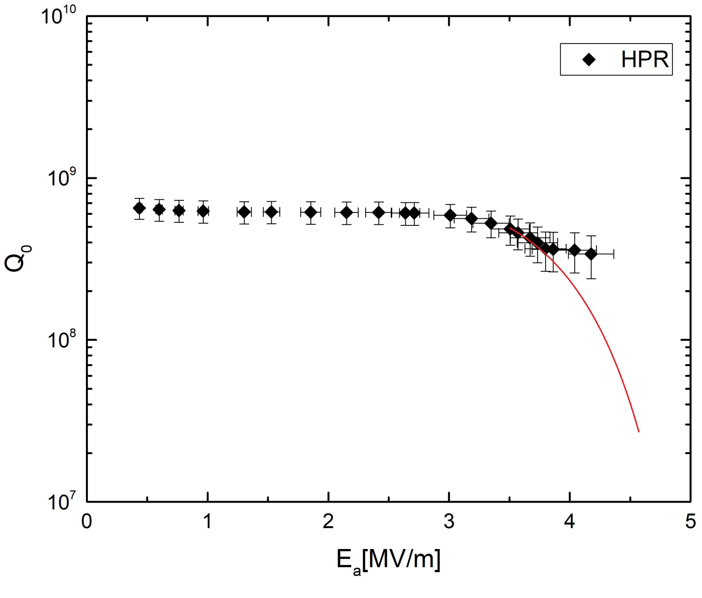

Figure 8.16: Performance curve after HPR. The estimated field emission drop without RF conditioning is plotted in red.

Field emission onset shifted to $E_a = 3.25\,\mathrm{MV/m}$ and during the measurement of the data points up to $E_a = 4.25\,\mathrm{MV/m}$, a conditioning effect could be observed where P_t slowly increased at constant forward power. To reduce the x-ray radiation towards the workstation, the conditioning was performed for 5–15 minutes per data point, resulting in the distorted Q-E field emission slope. The maximum gradient without conditioning is assumed to be in the range of 4–5 MV/m. The losses are shown in Figure 8.17.

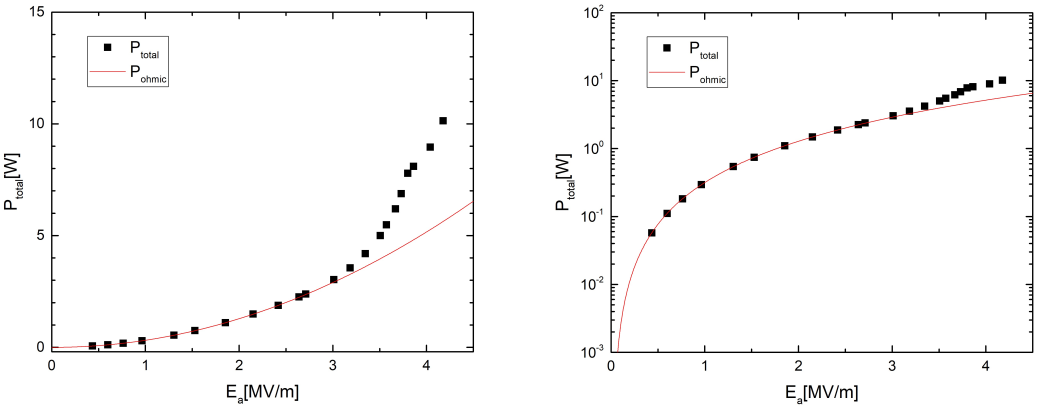

Figure 8.17: Total losses vs interpolated ohmic losses, at $E_a = 3.2\,\mathrm{MV/m}$ additional loss mechanisms set in.

The conditioning effect shows in the reduction of cavity loss slope above 3.9 MV/m.

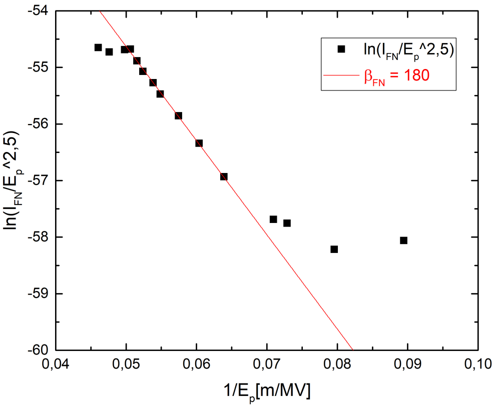

Figure 8.18: Fowler-Nordheim plot after HPR.

The decrease in β_{FN} from HPR treatment from 430 to 180, see Figure 8.18, is consistent with the increase in maximum electric field. The fast conditioning effect is also apparent in the Fowler-Nordheim plot, where the data point starts deviating from the slope.

8.6 CW RF Conditioning

CW RF conditioning was performed over a total of 3 days, where the field level was gradually chosen within the field emission Q-slope and concerning the maximum x-ray radiation, dictated by radiation protection, of 3.5 µSv/h at the work station. On day 2 of RF conditioning, an abrupt event took place, where the control system could not hold the cavity in resonance. The peak cavity pressure was observed at $3 \cdot 10^{-6}$ mbar and declined to $7 \cdot 10^{-10}$ mbar within 10 minutes. After the cavity reached equilibrium, the control system was able to hold the cavity in resonance and the Q-E change in Figure 6.12 was measured. The conditioning improvement within 5 to 15 minutes of each data point is highlighted by the difference between the curves in black and red.

τ_L	Q_L	β	Q_0	R_s	R_0
72.5 ms	$1.64 \cdot 10^8$	3.12	$6.76 \cdot 10^8$	83 nΩ	30 nΩ

Table 8.7: RF parameter results after RF conditioning.

Low-level measurements showed a negligible change in RF parameters, listed in Table 8.7, and the performance curve was taken right after the event and after the full conditioning.

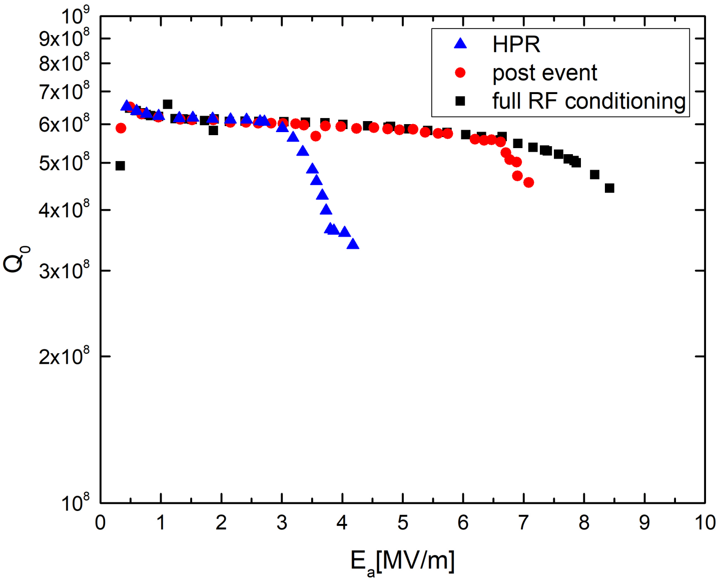

Figure 8.19: Performance curve after HPR, conditioning event, and full RF conditioning. The event occurred after 2 days of conditioning(blue to red) and the final conditioning took another 2 days (red to black).

Field emission onset level stayed consistent at roughly $E_a = 6.5\,\mathrm{MV/m}$ after the event and during the remaining conditioning. But the x-ray radiation doses at a given field level gradually decreased with RF conditioning time, see Figure 6.13. The maximum electric field increased from $E_a = 7.5\,\mathrm{MV/m}$ to $E_a = 8.4\,\mathrm{MV/m}$, as shown in Figure 8.19. In the first case, the cavity did not quench, but the radiation limit was reached during the conditioning phase. For the fully conditioned case, the cavity quenched slightly above 8.4 MV/m.

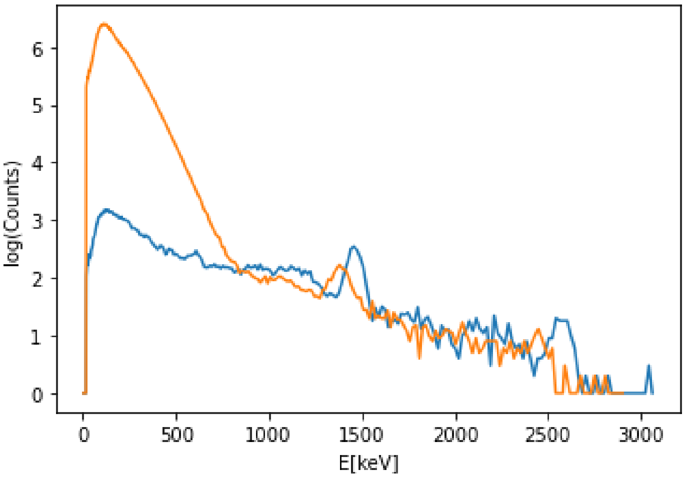

Figure 8.20: X-ray spectrum in blue is the baseline measurement without RF power, and in orange is the spectrum for $E_a = 8\,\mathrm{MV/m}$.

The X-ray spectrum in Figure 8.20 shows that the highest electron energy emitted is 700 keV and the maximum electron intensity is observed for 112 keV. For a gradient of $E_a = 8\,\mathrm{MV/m}$ the gap voltage is approximately 420 keV. It has to be noticed, that the distributions were measured from the outside of the cryotank and the device was not aligned with the beam axis, where the highest photon energies are typically emitted. From the measured distribution we can see, that the maximum energy gain from the electric field was the previously mentioned 700 keV. This suggests, that some emitted electrons can be accelerated through multiple gaps. The highest luminosity is given by the most probable case, which is acceleration inside one gap before a cavity wall is hit. The electrons do not experience the maximum voltage present in a gap, since the electrons are emitted off the beam axis and additionally have their transit time coefficient, depending on the RF phase at the time of emission.

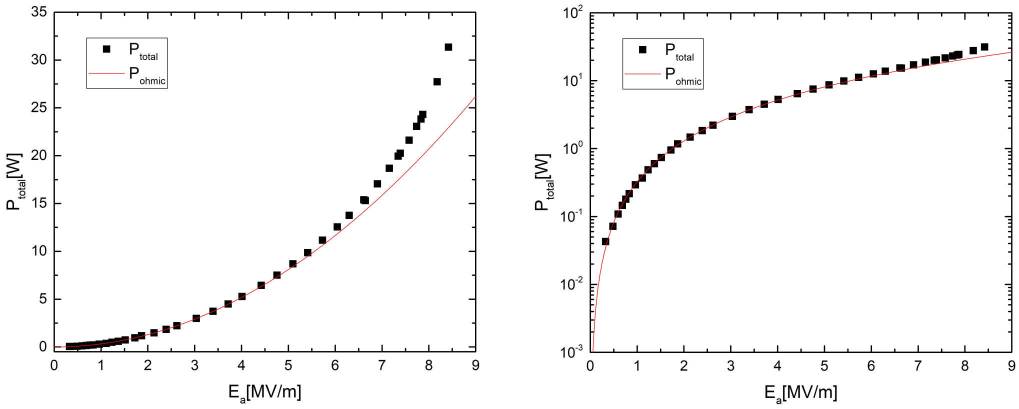

Figure 8.21: Total losses vs interpolated ohmic losses, at $E_a = 6\,\mathrm{MV/m}$ additional losses set in.

The total losses in Figure 8.21 are predominantly given by the ohmic losses of the cavity. This is in good agreement with the observed drop in X-ray radiation doses. The observed additional losses beyond 6 MV/m are given by field emission.

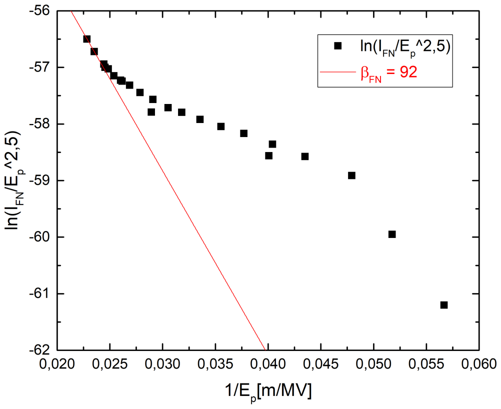

Figure 8.22: Fowler-Nordheim plot after RF conditioning.

The RF conditioning also shows in the Fowler-Nordheim amplification coefficient, seen in Figure 8.22, with a change from 180 to 92. This is additional confirmation of the fact, that emitters have been processed via CW conditioning.

8.7 Helium Processing

The helium processing procedure consisted of ion getter pump shutdown, cavity ventilation with clean helium to $\approx 5 \cdot 10^{-5}$ mbar, pulsed plasma ignition, cavity warm up to ≈ 50 K while pumping with the pumping station. This has to be performed to degas the helium condensate on the inner cavity surface. When the temperature is reached and the cavity pressure is below 10^{-5} mbar, the ion getter pump is used to pump down to 10^{-8} mBar and then the cooldown to 4 K is performed to measure the performance change.

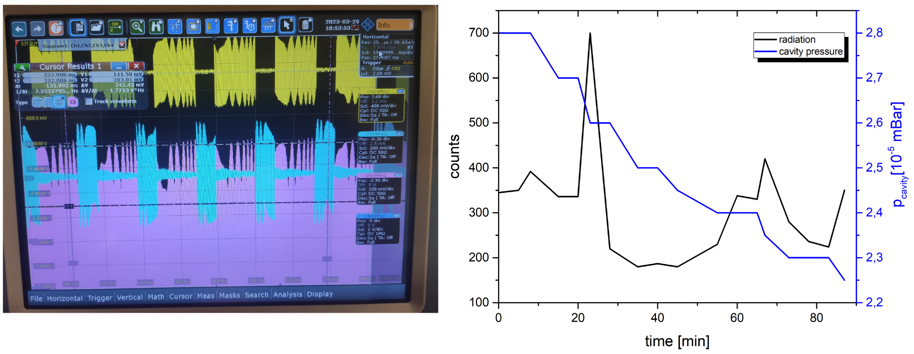

Figure 8.23: RF signal during active helium processing and radiation at the work station at constant forward power $P_f = 50$ W for 1.5 h.

The cavity was operated at a duty cycle of 67 % with 20 ms puls and 10 ms pause length. The x-ray radiation due to the plasma ignition from field emission is spatially highly inhomogeneous, depending on the active emitter. When an emitter is processed, a different one can get activated. This was observed during the helium processing, where the radiation towards the workstation fluctuated significantly over time, see Figure 8.23. The cavity pressure declined over time, which is mostly due to declining helium bath level with associated cavity volume expansion. The ion-getter pump was deactivated for the entire processing procedure.

τ_L	Q_L	β	Q_0	R_s	$R_{s,BCS}$	$R_{s,ext}$	R_0
71 ms	$1.64 \cdot 10^8$	3.23	$6.80 \cdot 10^8$	82 nΩ	49 nΩ	4 nΩ	29 nΩ

Table 8.8: RF parameter results after 2 h helium processing.

The helium showed a small reduction of Q_L while the β increased results in an overall small increase of Q_0 at low field levels as shown in Table 8.8. Since the changes are negligible, it is safe to assume that the coupler and cavity were not damaged by the plasma ignition.

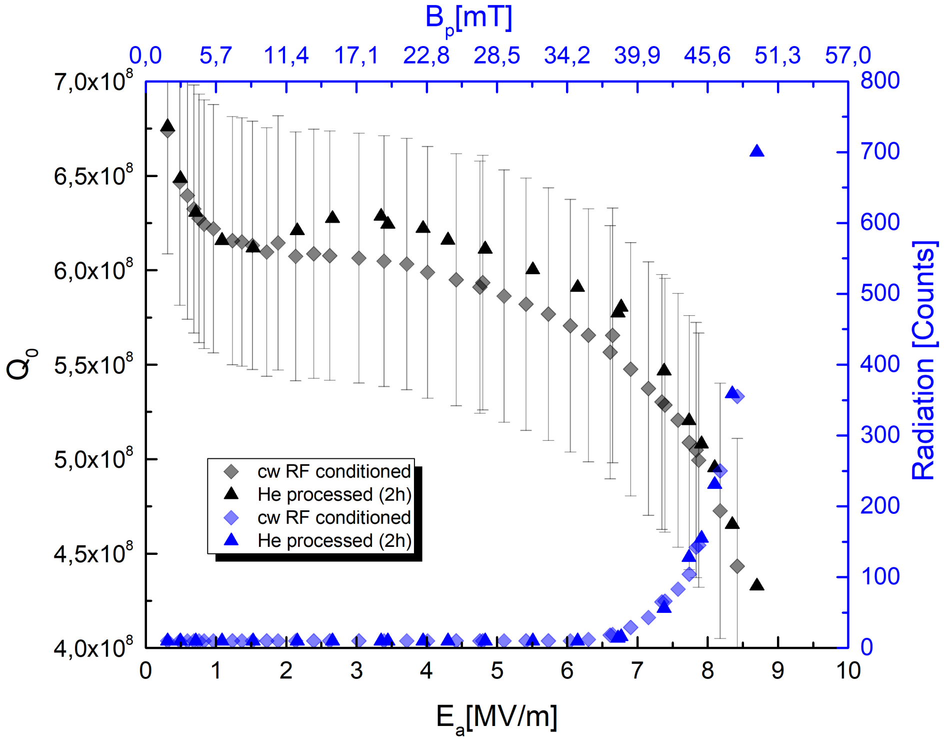

Figure 8.24: With similar radiation response to the cw RF conditioned state, decreased losses from residual resistance are observed in the medium-field region. The peak magnetic field B_p remains well below the critical magnetic field level during the measurement.

Radiation towards the working station after helium processing was equal to the cw RF conditioned case, as shown in Figure 8.24, while the maximum electric field increased from $E_a = 8.4\,\mathrm{MV/m}$ to $E_a = 8.7\,\mathrm{MV/m}$.
A surprising effect is given by the 5% increase in Q_0 for E_a in the range of (2–6.75)MV/m. All Q-values lie within the measurement uncertainty band of the prior measurement and the argument for disregarding these findings could be made. This curve characteristic can not be found in any prior cold test and is exclusive to the performance plot after helium treatment. With the observed onset of radiation, the relative increase shrinks, because the additional losses due to field emission become an increasingly relevant contribution to the total losses. The Q-slope is not affected by emission losses up to $E_a = 7\,\mathrm{MV/m}$. The Q-E behavior shows similarities to an effect in N-doped cavities, where an increase of Q-value can occur up to higher levels than previously recorded, see figure 6.17. The infusion effect on the surface layer depends on temperature, baking duration, and nitrogen pressure.
It is safe to say that surface bombardment with helium ions during the processing event

led to plasma-oxide layer interactions. Further investigation into helium processing and the effect of different parameters such as E_p, processing time, pulse length, duty cycle, and helium pressure on cavity performance could lead to an optimized protocol for SC CH structures.

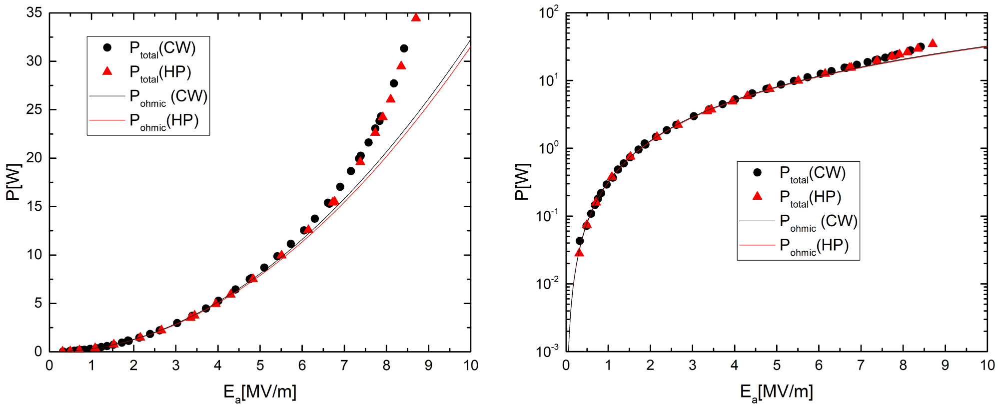

Figure 8.25: Total losses vs interpolated ohmic losses, at $E_a = 6\,\mathrm{MV/m}$ additional loss mechanisms set in. A slight change in ohmic losses can be observed after the helium processing, which is in agreement with the observed increase in intrinsic quality factor above $2\,\mathrm{MV/m}$.

The decrease in ohmic losses after helium processing, shown in Figure 8.25, reflects the observed increase in intrinsic quality factor and maximum gradient.

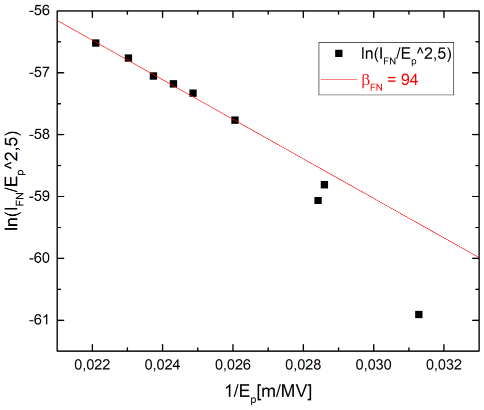

Figure 8.26: Fowler-Nordheim plot after helium processing.

The helium processing shows a slight increase in the Fowler-Nordheim amplification coefficient, shown in Figure 8.26, from 92 to 94.

9 Summary and Outlook

This dissertation outlines the experiences gained from employing various preparation methods for CH cavities and offers an optimized preparation protocol to further increase cavity performance post-manufacturing. The performance is assessed using two key RF parameters: the electric field E_a and the intrinsic quality factor Q_0. Unlike NC cavities, the intrinsic quality factor of SC cavities can vary significantly with increasing electric field. The optimum outcome for cavity preparation is to increase the maximum electric field while maintaining higher Q_0 over the entire field span. Since Q_0 is inversely proportional to cavity losses, an increase in quality factor reduces cryo-losses for operation at a given field level. The performance development throughout this work is displayed in Figure 9.1.

The majority of SC cavities are high-beta elliptical cavities, and preparation methods have primarily been tailored to optimize these structures. This study focuses on implementing the most reliable and promising surface treatments on the first SC CH cavity prototype developed by IAP. This cavity exhibited decreased performance after 11 years of storage, with a notable onset of strong radiation at low electric fields. This was most probably caused by accidental ventilation with normal air, introducing particles acting as emitters. Additionally, a redesign of the power coupler was required due to overcoupling of existing ones.

A 120°,C bake for 48 h was applied, resulting in an improved quality factor at low levels and in a reduced time required to process multipacting barriers. However, this treatment further decreased the maximum electric field. The quality factor improvement is attributed to the degassing of hydrocarbons during the bake. The negative effect on the electric field is less likely due to the bake itself and more likely related to cavity transportation and infrastructure at the experimental hall.

The performance limitation of the cavity was expected to be caused by enclosed particles inside the resonator. High-pressure rinsing with ultra-pure water is the standard procedure to achieve high cleanliness of the inner surfaces after treatments that have the risk of surface contamination. HPR has been planned and performed in collaboration with Helmholtz-Institute-Mainz and "Gesellschaft für Schwerionenforschung". The cavity improved in performance during the measurement of the Q-E curve, which did not occur before the HPR. With CW RF conditioning, the cavity showed the highest gradient achieved with a far weaker Q-drop at high-field levels. In both the 2008 measurement and the described measurement, the cavity was finished by HPR treatment, but for the HPR treatment at HIM some adjustments have been prepared. The 360 MHz cavity does not possess any additional off-axis flushing ports and was therefore rinsed by two different nozzles with different spray angles to maximize the covered inner resonator surfaces. The use of multiple spray angles could also benefit CH cavities equipped with flushing ports and should be investigated for future HPR applications.

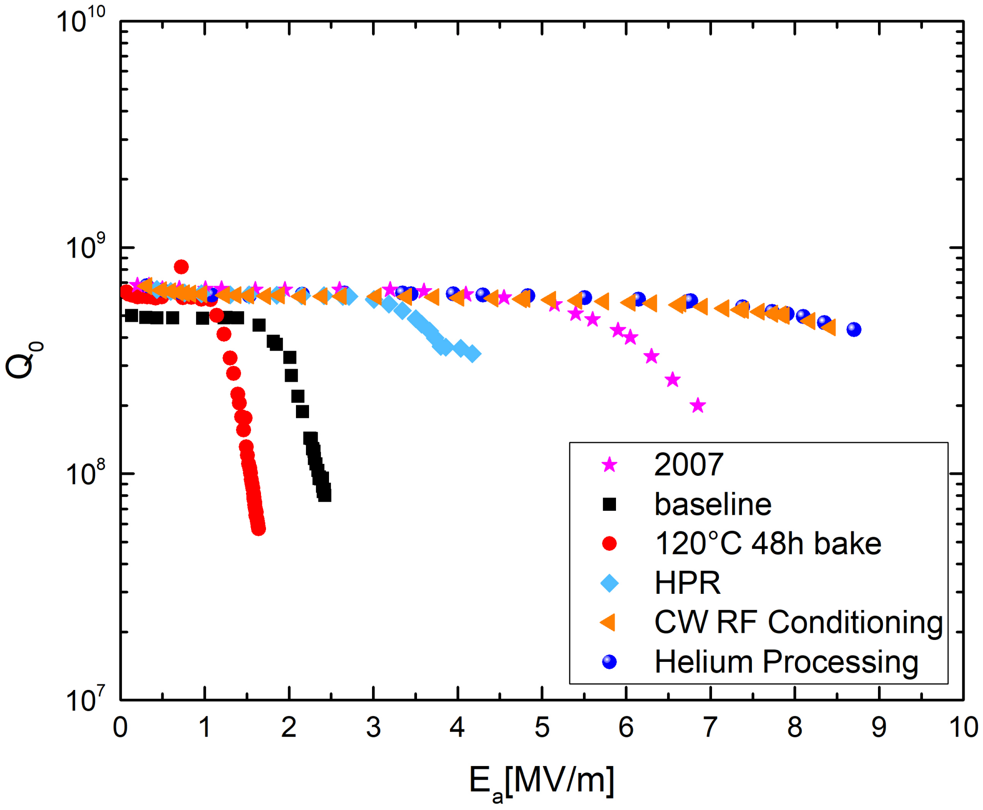

Figure 9.1: Shows the performance development of the 360 MHz CH cavity with the prior highest performance achieved in 2007.

Helium processing has been performed on the CH prototype for a total time of 2.5 hours and produced promising results in terms of Q-value and gradient optimization. During the helium processing, the radiation was measured at a fixed angle and showed strong time-dependent fluctuations. This indicated the processing of emitters and was subsequently confirmed with an 3.5 % increase in the electric field from 8.4 MV/m to 8.7 MV/m. An unexpected effect was found in the medium- to high-field Q-slope, where the quality factor exhibited a 5 % elevation above 2 MV/m compared to the HPR-RF-conditioned case. This systematic increase has never been observed for this cavity before the treatment. Nitrogen-doped cavities show similar behavior, where interactions within the oxide layer are correlated to changes in quality factors. Since helium is a non-reactive element, possible explanations for this effect are the sputtering process and helium deployment inside the surface. A new series of helium-processing is planned to find an optimized and safe recipe for CH cavities. The Q-E measurement after the cooldown and before the treatment will also show if the performance gain is affected by a warm-up to room temperature.

The treatment sequence outlined in this work is strongly recommended for CH cavities and is illustrated in Figure 9.2. The bake-out has proven effective in reducing the high-field Q-slope and multipacting which remains unaffected by subsequent HPR. In the case of the 360 MHz cavity, rinsing with different spray angles during HPR has shown favorable results. This positive effect may extend to CH cavities with flushing ports, warranting further investigation into the use of multiple spray angles. Notably, no negative effects on multipacting from HPR have been observed in this study. CW RF conditioning is then performed until the maximum cavity performance is reached. When the cavity is still limited by field emission, a repeat of HPR treatment should be considered since no CH cavity showed to be limited by this effect when HPR was carefully executed. It also has to be noted, that the helium processing has only been performed on the 360 MHz CH cavity when it showed low radiation and field emission. The risk of helium processing on CH cavities with high levels of field emission is unknown. The electron currents and therefore ion bombardment avalanches are expected to increase and pose a greater risk for the damage of cavity components. With the current knowledge, helium processing should only be considered for well-prepared cavities with minimal field emission.

This work presents an optimized plan for CH cavity preparation, maximizing performance post-standard BCP treatment. New insights into the optimization of each treatment lay the foundation for further research into CH cavity preparation.

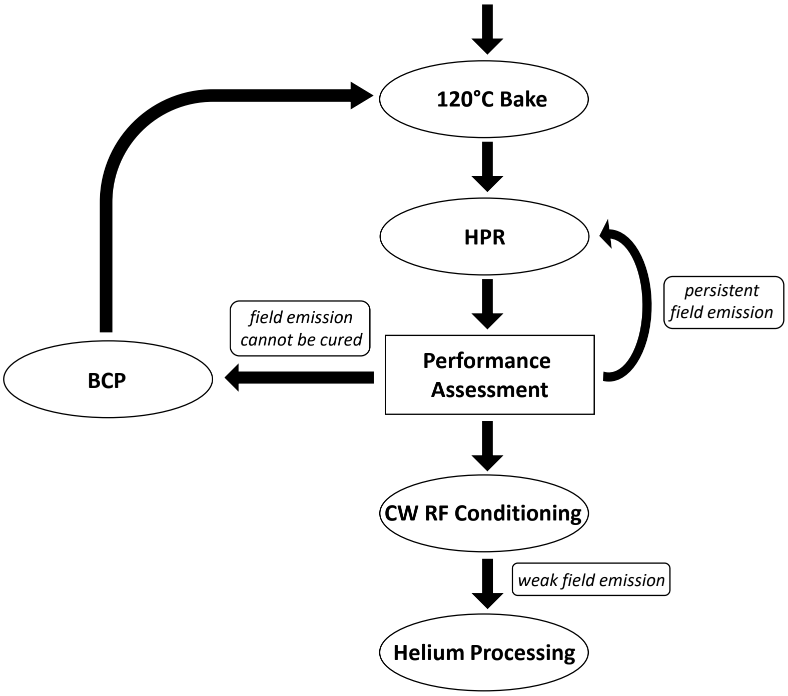

Figure 9.2: Schematic recommended preparation protocol for CH cavities.

Acknowledgement

I would like to take the opportunity to thank all the people and organizations who made it possible for me to conduct the research summarized in this thesis and who have been very supportive over the years.

First and foremost, I want to express my sincere gratitude to my supervisor Prof. Dr. H. Podlech for the opportunity to do my doctorate in his group, for the support in all phases of this thesis.

Many thanks also to my second reviewer Prof. Dr. U. Ratzinger, who has always had an open ear and provided helpful advice with his expertise.

I would like to express my gratitude to all my colleagues at the Institute of Applied Physics who supported me and my work during these studies. In particular, I would like to mention Dr. D. Koser, Dr. M. Basten, N. Petry, Dr. K. Kümpel, S. Lamprecht, Dr. T. Conrad, Dr. H. Hähnel, Dr. M. Busch, J. Storch, P. Braun, D. Bänsch, T. Metz, C. Wagner and S. Rapphahn.

Always prompt help in administrative matters I received from L. Quist, A. Hergt and M. Scholz. Thank you.

I would also like to thank my colleagues at GSI Darmstadt, HI Mainz and JGU Mainz for the good cooperation and time during the HPR preparation. I like to name in particular Prof. Dr. W. Barth, Dr. M. Miski-Oglu, Dr. F. Dziuba, Dr. C. Burandt, Dr. T. Kürzeder, V. Gettmann, S. Lauber and J. List.

I received fundamental support from the German Federal Ministry of Education and Research (BMBF, contr. nos. 05P15RFRBA and 05P18RFRBA), the Helmholtz Research Academy Hesse for FAIR (HFHF), and the Helmholtz Graduate School for Hadron and Ion Research (main doctus scholarship) with special consideration of family Giersch.

Last but not least, I would like to thank my family, and all other friends not mentioned here by name for their loving support, both inside and outside the university.

List of Figures

List of Tables

References

[1] W. Demtröder. *Experimentalphysik 4 (2005).* Springer-Verlag Berlin Heidelberg, DOI: `https://doi.org/10.1007/b138029`.

[2] O. Hahn and F. Strassmann. Über den Nachweis und das Verhalten der bei der Bestrahlung des Urans mittels Neutronen entstehenden Erdalkalimetalle. *Naturwissenschaften Vol. 27 (1939)*, pages 11–15, DOI: `https://doi.org/10.1007/bf01488241`.

[3] Flerov and Petrjak. Spontaneous Fission of Uranium. *Phys. Rev. Vol. 58 (1940)*, DOI: `https://doi.org/10.1103/physrev.58.89.2`.

[4] C. Simenel, P. McGlynn, A. S. Umar, and K. Godbey. Comparison of fission and quasi-fission modes. *Physics Letters B Vol. 882 (2021)*, DOI: `https://doi.org/10.1016/j.physletb.2021.136648`.

[5] S. Hofmann, V. Ninov, F. P. Heßberger, and P. Armbruster et al. Production and decay of $^{269}110$. *Zeitschrift für Physik A Hadrons and Nuclei Vol. 350 (1995)*, DOI: `https://doi.org/10.1007/BF01291181`.

[6] Yu. Ts. Oganessian, F. Sh. Abdullin, C. Alexander, and J. Binder et al. Production and decay of the heaviest nuclei $^{293,294}117$ and $^{294}118$. *Phys. Rev. Lett. Vol.109 (2012)*, DOI: `https://doi.org/10.1103/physrevlett.109.162501`.

[7] J. H. Hamilton, S. Hofmann, and Y. T. Oganessian. Search for Superheavy Nuclei. *Annual Review of Nuclear and Particle Science Vol. 63 (2013)*, pages 383–405, DOI: `https://doi.org/10.1146/annurev-nucl-102912-144535`.

[8] GSI. Gesellschaft für Schwerionenforschung. URL: `https://www.gsi.de/forschungbeschleuniger/fair`.

[9] M. Schwarz. *Beam dynamics design of an energy-variable superconducting heavy ion accelerator (2021).* doctoralthesis, Universitätsbibliothek Johann Christian Senckenberg, DOI: `https://doi.org/10.21248/gups.64448`.

[10] G. Bisoffi, L. Bellan, M. Bellato, and D. Borille et al. Hardware Commissioning of the Refurbished ALPI Linac at INFN-LNL to Serve as SPES Exotic Beam Accelerator. *Journal of Physics: Conference Series Vol. 1350 (2019)*, DOI: `https://dx.doi.org/10.1088/1742-6596/1350/1/012091`.

[11] E. Fagotti et al. Operational Experience in PIAVE-ALPI Complex. In *Proc. HIAT'09 (2009), Venice, Italy*, pages 208–212, URL: `https://jacow.org/HIAT2009/papers/FR-04.pdf`.

[12] S. M. Gerbick, M. P. Kelly, R. C. Murphy, and T. Reid. A New Electropolishing System For Low-Beta SC Cavities. In *Proc. SRF'11 (2011), Chicago, USA*, pages 576–578, URL: `https://jacow.org/SRF2011/papers/WEIOA03.pdf`.

[13] S. C. Jeong. Progress of the RAON Heavy Ion Accelerator Project in Korea. In *Proc. IPAC'16 (2016), Busan, Korea*, pages 4261–4265, DOI: `https://doi.org/10.18429/JACOW-IPAC2016-FRYAA01`.

[14] C. Marchand et al. Performances of Spiral2 Low and High Beta Cryomodules. In *Proc. SRF'15 (2015), Whistler, Canada*, pages 967–972, URL: `https://jacow.org/SRF2015/papers/WEBA04.pdf`.

[15] N. Sakamoto et al. Development of Superconducting Quarter-Wave Resonator and Cryomodule for Low-Beta Ion Accelerators at RIKEN Radioactive Isotope Beam Factory. In *Proc. SRF'19 (2019), Dresden, Germany*, pages 750–757, DOI: `https://doi.org/10.18429/JACOW-SRF2019-WETEB1`.

[16] A. Sublet et al. Status of HIE-ISOLDE SC Linac Upgrade. In *Proc. IPAC'15 (2015), Richmond, USA*, pages 3151–3154, DOI: `https://doi.org/10.18429/JACOW-IPAC2015-WEPHA021`.

[17] Z. Y. Yao et al. Operating Experience on Cavity Performance of ISAC-II Superconducting Heavy Ion Linac. In *Proc. SRF'17 (2017), Lanzhou, China*, pages 527–530, DOI: `https://doi.org/10.18429/JACOW-SRF2017-TUPB064`.

[18] M. Busch et al. Overview on SC CH-Cavity Development. In *Proc. IPAC'19 (2019), Melbourne, Australia*, pages 2822–2825, DOI: `https://doi.org/10.18429/JACOW--IPAC2019--WEPRB012`.

[19] S. Y. Lee. *Accelerator Physics (2004).* World Scientific Publishing Co. Pte. Ltd, Singapore, second edition, DOI: `https://doi.org/10.1142/5761`.

[20] F. Hinterberger. *Physik der Teilchenbeschleuniger und Ionenoptik (2008).* Springer-Verlag Berlin Heidelberg, DOI: `https://doi.org/10.1007/978-3-540-75282-0`.

[21] K. Wille. *Physik der Teilchenbeschleuniger und Synchrotronstrahlungsquellen (1992).* Vieweg+Teubner Verlag Wiesbaden, DOI: `https://doi.org/10.1007/978-3-663-11850-3`.

[22] H. Wiedemann. *Circular Accelerators (2015)*, pages 59–80. Springer International Publishing, Cham, DOI: `https://doi.org/10.1007/978-3-319-18317-6_3`.

[23] CST. *Computer Simulation Technology.* URL: `http://www.cst.com`.

[24] H. Podlech. *Entwicklung von normal- und supraleitenden CH-Strukturen zur effizienten Beschleunigung von Protonen und Ionen (2008)*. Habilitation, URL: `http://linac.physik.uni-frankfurt.de/publikationen/habil-podlech.pdf`.

[25] H. Padamsee, J. Knobloch, and T. Hays. *RF Superconductivity for Accelerators (1998)*. Wiley-VCH, ISBN: `https://www.isbns.net/isbn/9780471154327/`.

[26] U Ratzinger. H-type linac structures (2005). `https://doi.org/10.5170/CERN-2005-003.351`.

[27] Huifang Wang. *Operation of Copper Cavities at Cryogenic Temperatures (2023)*. doctoralthesis, Universitätsbibliothek Johann Christian Senckenberg, DOI: `https://doi.org/10.21248/gups.79228`.

[28] H. Hähnel, A. Ateş, B. Dedić, and U. Ratzinger. Additive manufacturing of an ih-type linac structure from stainless steel and pure copper. *Instruments Vol.7 (2023)*, `https://doi.org/10.3390/instruments7030022`.

[29] F. S. He et al. Manufacturing of the Main Accelerator with TESLA-like 9-cell SRF Cavities at Peking University. In *Proc. IPAC'10 (2010), Kyoto, Japan*, pages 2977–2979, URL: `http://accelconf.web.cern.ch/IPAC10/papers/WEPEC041.pdf`.

[30] H. Padamsee, J. Knobloch, and T. Hays. *RF superconductivity for accelerators (2009)*. Wiley-VCH, ISBN: `https://www.isbn.de/buch/9783527405725/rf-superconductivity`.

[31] J. Graber, P. Barnes, J. Kirchgessner, and D. Moffat et al. A world record accelerating gradient in a niobium superconducting accelerator cavity. In *Proceedings of International Conference on Particle Accelerators Vol. 2 (1993)*, pages 892–894, DOI: `https://doi.org/10.1109/pac.1993.308739`.

[32] V. Shemelin and H. Padamsee. The optimal shape of cells of a superconducting accelerating section (2002). URL: `https://www.classe.cornell.edu/public/SRF/2002/SRF020128-01/OPTSHAPE.pdf`.

[33] J. Sekutowicz, G. Ciovati, P. Kneisel, and G. Wu et al. Cavities for JLab's 12 GeV upgrade. In *Proceedings of the 2003 Particle Accelerator Conference (2003), Portland, OR, USA*, pages 1395–1397, DOI: `https://doi.org/10.1109/pac.2003.1289717`.

[34] J. Sekutowicz, K. Ko, L. Ge, and L. Lee et al. Design of a Low Loss SRF Cavity for the ILC. In *Proceedings of the 2005 Particle Accelerator Conference (2005)*, pages 3342–3344, DOI: `https://doi.org/10.1109/pac.2005.1591465`.

[35] T. Saeki, F. Furuta, K. Saito, and Y. Higashi et al. Initial Studies of 9-cell High-Gradient Superconducting Cavities at KEK (2006). URL `https://api.semanticscholar.org/CorpusID:56265972`.

[36] M. Busch. *Auslegung und Messungen einer supraleitenden 325 MHz CH-Struktur für Strahlbetrieb.* doctoralthesis, Universitätsbibliothek Johann Christian Senckenberg, 2015, URL: `https://publikationen.ub.uni-frankfurt.de/frontdoor/index/index/year/2015/docId/38625`.

[37] F. Dziuba. *Entwicklung und Test einer supraleitenden 217 MHz CH-Kavität für das Demonstrator-Projekt an der GSI.* doctoralthesis, Universitätsbibliothek Johann Christian Senckenberg, 2016, URL: `https://publikationen.ub.uni-frankfurt.de/frontdoor/index/index/docId/41485`.

[38] M. Basten. *Entwicklung und Inbetriebnahme zweier supraleitender 217 MHz CH-Strukturen für das HELIAC-Projekt.* doctoralthesis, Universitätsbibliothek Johann Christian Senckenberg, 2019, URL: `https://publikationen.ub.uni-frankfurt.de/frontdoor/index/index/docId/51767`.

[39] C. Munz and T. Westermann. *Numerische Behandlung gewöhnlicher und partieller Differenzialgleichungen (2019).* Springer Vieweg, DOI: `https://doi.org/10.1007/978-3-662-55886-7`.

[40] W. Buckel and K. Reinhold. *Superconductivity.* Wiley-VCH (2004) DOI: `10.1002/9783527618507`.

[41] Wikipedia. URL: `https://commons.wikimedia.org/wiki/File:EXPULSION.png`.

[42] P. Bauer, N. Solyak, G. L. Ciovati, and G. Eremeev et al. Evidence for non-linear BCS resistance in SRF cavities. *Physica C: Superconductivity Vol. 441 (2006)*, pages 51–56. DOI: `https://doi.org/10.1016/j.physc.2006.03.056`.

[43] G. Ciovati. *Investigation of the Superconducting Properties of Niobium Radio-Frequency Cavities.* doctoralthesis, Old Dominion University, 2005, DOI: `https://doi.org/10.25777/SASG-CE57`.

[44] G. Ciovati. Review of High Field Q-Slope, Cavity Measurements. In *Proc. SRF'07 (2007), Beijing, China*, pages 70–74, URL: `https://jacow.org/srf2007/papers/TU102.pdf`.

[45] G. Ciovati and A. Gurevich. Evidence of high-field radio-frequency hot spots due to trapped vortices in niobium cavities. *Phys. Rev. ST Accel. Beams Vol. 11 (2008)*, DOI: `https://doi.org/10.1103/physrevstab.11.122001`.

[46] A. Gurevich and G. Ciovati. Dynamics of vortex penetration, jumpwise instabilities, and nonlinear surface resistance of type-II superconductors in strong rf fields. *Phys. Rev. B Vol. 77 (2008)*, DOI: `https://doi.org/10.1103/physrevb.77.104501`.

[47] R. Ricker. Thermodynamic Evaluation of the Propensity of Niobium to Absorb Hydrogen During Fabrication of Superconducting Radio Frequency Accelerator Cavities (2009), URL: `https://tsapps.nist.gov/publication/get_pdf.cfm?pub_id=903830`.

[48] G. Ciovati. Effect of low-temperature baking on the radio-frequency properties of niobium superconducting cavities for particle accelerators. *Journal of Applied Physics Vol. 96 (2004)*, pages 1591–1600, DOI: `https://doi.org/10.1063/1.1767295`.

[49] G. Ciovati, G. Myneni, F. Stevie, P. Maheshwari, and D. Griffis. High field Q slope and the baking effect: Review of recent experimental results and new data on Nb heat treatments. *Phys. Rev. ST Accel. Beams Vol. 13 (2010)*, DOI: `https://doi.org/10.1103/physrevstab.13.022002`.

[50] T Kürzerder, K Aulenbacher, W Barth, and C Burandt et al. Commissioning of a Cleanroom for SRF Activities at the Helmholtz Institute Mainz. *SRF 2019 (2019), Dresden, Germany*, pages 1162–1167, DOI:`https://doi.org/10.18429/JACOW-SRF2019-THP101`.

[51] T. Kürzeder, K. Aulenbacher, W. Barth, and C. Burandt et al. Cleanroom installations for SRF cavities at the Helmholtz Institute Mainz. *Journal of Physics: Conference Series Vol. 1350 (2019)*, pages 1–4, DOI: `https://doi.org/10.1088/1742-6596/1350/1/012186`.

[52] Inventor. *Autodesk*. URL: `https://www.autodesk.de`.

[53] J. Knobloch and H. Padamsee. Microscopic investigation of field emitters located by thermometry in 1.5 GHz superconducting niobium cavities. *Proceedings of the 1995 Workshop on RF Superconductivity (1995), Gif-sur-Yvette, France*, pages 95–103, URL: `https://accelconf.web.cern.ch/SRF95/papers/srf95b03.pdf`.

[54] O. C. Brunner, A. Butterworth, G. Cavallari, and N. Hilleret et al. First Experience with in situ Helium Processing of the LEP Superconducting Modules. *8th Workshop on RF Superconductivity (1998), Abano-Terme, Italy*, pages 133–137, URL: `https://cds.cern.ch/record/352578`.

[55] S. C. Huang, Q. W. Chu, Y. He, and C. L. Li et al. The Effect of Helium Processing and Plasma Cleaning for Low Beta HWR Cavity. In *Proc. SRF'19 (2019), Dresden, Germany*, pages 1228–1230, DOI: `https://doi.org/10.18429/JACoW-SRF2019-FRCAB6`.

[56] B. Giaccone, M. Martinello, P. Berrutti, and O. Melnychuk et al. Field emission mitigation studies in the SLAC Linac Coherent Light Source II superconducting rf cavities via in situ plasma processing. *Phys. Rev. Accel. Beams Vol. 24 (2021)*, DOI: `https://doi.org/10.1103/physrevaccelbeams.24.022002`.

[57] A. Wu, L. Yang, C. Hu, and C. Li et al. In-situ plasma cleaning to decrease the field emission effect of half-wave superconducting radio-frequency cavities (2018). *Nuclear Instruments and Methods in Physics Research Section A: Accelerators, Spectrometers, Detectors and Associated Equipment Vol. 905*, pages 61–70, DOI: `https://doi.org/10.1016/j.nima.2018.07.039`.

[58] P. V. Tyagi, M. Doleans, B. Hannah, and R. Afanador et al. Improving the work function of the niobium surface of SRF cavities by plasma processing. *Applied Surface Science Vol. 369 (2016)*, pages 29–35, DOI: `https://doi.org/10.1016/j.apsusc.2016.02.030`.

[59] B. Giaccone et al. Plasma Cleaning of LCLS-II-HE verification cryomodule cavities. *Phys. Rev. Accel. Beams Vol. 25 (2022)*, DOI: `https://doi.org/10.1103/physrevaccelbeams.25.102001`.

[60] K. Turaj, O. Brunner, A. Butterworth, and F. Gerigk et al. Degradation and Recovery of the LHC RF Cryomodule Performance Using the Helium Processing Technique. *Proceedings of the 20th International Conference on RF Superconductivity (2022)*, pages 746–750, DOI: `https://doi.org/10.18429/JACOW-SRF2021-THPFAV006`.

[61] A. Romanenko. Review of High Field Q-slope, Surface Measurements. In *Proc. SRF'07 (2007), Beijing, China*, pages 75–81, https://jacow.org/srf2007/papers/TU103.pdf.

[62] K. Umemori et al. Study on Nitrogen Infusion for 1.3 GHz SRF Cavities Using J-PARC Furnace. In *Proc. LINAC'18 (2018), Beijing, China*, Linear Accelerator Conference, pages 499–502, DOI: `https://doi.org/10.18429/JACOW-LINAC2018-TUPO071`.

[63] P. Dhakal. Recent Development on Nitrogen Infusion Work Towards High Q and High Gradient. In *Proc. SRF'19 (2019), Dresden, Germany*, pages 355–359, DOI: `https://doi.org/10.18429/JACOW--SRF2019--TUFUA5`.

[64] M. Checchin et al. New Insight on Nitrogen Infusion Revealed by Successive Nanometric Material Removal. In *Proc. IPAC'18 (2018), Vancouver, Canada*, pages 2665–2667, DOI: `https://doi.org/10.18429/JACOW--IPAC2018--WEPMK016`.